Dear reader,

In the last decades we have witnessed the presence of a characteristic phenomenon: a gradual increase in technical parameters of machinery and equipment at the simultaneous decrease in their mass related to the unit of output.

This tendency can be expected also in the future as it is progressive not only from technical and economic points of view but also from the point of view of ecology. Constructional materials will occupy a dominant position in this area. Development activities in the area of constructional materials are oriented towards a further increase in strength characteristics, resistance against fragility impairment, towards improvement of surface and technological characteristics.

The above mentioned trends leading to the improvement of materials quality together with modern constructional calculations are the basis for optimal use of constructional materials.

In this issue of the COMMUNICATIONS you will have an opportunity to read articles and get acquainted with results representing mutual relationships among „structure – properties – use" of constructional materials.

Otakar Bokůvka

Jaroslav Pokluda *

THEORETICAL STRENGTH OF SOLIDS

The significance of theoretical strength (TS) investigations is explained and a brief overview of the current state of TS calculations is presented on the background of a historical evolution. Influence of crystal defects on TS is outlined by taking into account published theoretical models. The study is completed by a discussion concerning differences between theoretical and experimental results.

1. Introduction

The strength of engineering materials is usually controlled by nucleation and motion of dislocations or microcracks. If such defects were not present, the material would only fail if the *theoretical (ideal) strength* were reached. As a rule, this value is related to the infinite perfect monocrystal (as a generally most stable state of a solid) of particular chemical composition under defined loading mode. Starting from the beginning of the last century, there is a more or less continuous effort expended in order to obtain theoretical and experimental data concerning TS of various solids [1]. The TS values set an upper limit to the envelope of attainable strength and its knowledge enables us to assess the gap remaining to upper strength values of advanced engineering materials in each period of time. However, this is by far not the only reason for the TS investigation.

From the theoretical point of view, the TS plays a decisive role in the fundamental theory of fracture. For example, the stress necessary for nucleation of dislocation loop can be identified with the shear TS value and the local stress for nucleation of a cleavage crack should overcome the tensile TS value [2, 3]. The ratio of these values expresses the tendency of the crystal matrix to become brittle or ductile [4, 5]. From the practical point of view, the shear TS appears to control both the onset of fracture and dislocation nucleation in defect-free thin films and, in particular, in nanostructured materials that are currently being developed. It has been confirmed most eloquently by nanoindentation experiments (see e. g. [6, 7]). Moreover, the perfect monocrystalline wires (whiskers) are used as reinforcements in advanced composite materials and large metallic and ceramic monocrystals start to be important in special engineering components, e.g. in turbine blades [8].

When considering a perfect crystal deforming homogeneously in a nonlinear elastic way [9], the total internal energy of the crystal can be expanded as

$$E = E_0 + V\sum_i \sigma_i \eta_i + \frac{1}{2} V \sum_i \sum_j C_{ij}\, \eta_i\, \eta_j + O(\eta^3)$$

$$i, j = 1, 2, ..., 6, \qquad (1)$$

where σ_i are components of the stress tensor, η_i are components of the Lagrangian strain tensor, C_{ij} are the second order elastic coefficients and V is the crystal volume. Here, the simple Voigt notation can be used since the tensors σ_{ij}, η_{ij} and C_{ijkl} ($i, j, k, l = 1, 2, 3$) are symmetric with respect (ij) $\leftrightarrow$ (ji) to interchange. By setting $E_0 = 0$ and using the internal energy per volume unit $E_u = E/V$, one can simply write

$$C_{ij} = \frac{\partial^2 E_u}{\partial \eta_i\, \partial \eta_j} \qquad (2)$$

$$\sigma_i = \frac{\partial E_u}{\partial \eta_i}. \qquad (3)$$

The *energy-strain curve* can be determined using empirical interatomic potentials or calculating the electronic structure of the crystal. For each particular loading case, the TS is characterized by a set of 6 values of the associated stress tensor components. Consequently, an infinite number of "theoretical strengths" exists for a given crystal. For practical reasons, only special loading cases, determined by a single value of the stress tensor component, used to be connected with the TS value. It concerns the uniaxial and the three-axial (hydrostatic) tension and compression loading modes as well as the simple shear case. The respective TS values denoted as σ_{iut}, σ_{iuc}, σ_{iht}, σ_{ihc} and τ_{is} cover the most important stress state range occurring in engineering practice. In these cases, TS corresponds to a maximum reachable gradient on the energy-strain curve and its attainment is accompanied by a mechanical instability of the crystal lattice.

2. The History of Theoretical Strength Investigation

The well known classical estimations of TS values τ_{is} and σ_{iut} are those of Frenkel [10] and Orowan-Polanyi [11]:

$$\tau_{is} = \frac{Gb}{2\pi h}, \qquad (4)$$

$$\sigma_{iut} = \left(\frac{E\gamma}{a_0}\right)^{1/2}, \qquad (5)$$

* **Jaroslav Pokluda**
Institute of Engineering Physics, Brno University of Technology, Technická 2, CZ-616 69 Brno, Czech Republic

where E and G are elastic moduli in tension and shear, b is the size of the Burgers vector, h is the distance between shear planes, γ is the surface energy and a_0 is the lattice constant in the tensile direction. Both expressions can be easily derived assuming the *sinusoidal stress-strain curve*. In spite of a simple pair atomic interaction approach, both relations give a plausible orientation results $\tau_{is} \approx G/10$ and $\sigma_{iut} \approx E/10$ for TS values.

The Mackenzie theory [12] represents a further milestone in the development of TS calculations. The first three terms of the Fourier expansion are used as the *energy-strain curve*. On the other hand, however, it allowed some physically irrelevant assumptions leading to very small values of $\tau_{is} = G/30$ for fcc. crystals [13]. Since that value seemed to be rather close to some experimental results, an optimistic conclusion was accepted simultaneously with a term change from *theoretical* to ideal strength [1, 12, 14]. However, more recent semiempirical and ab initio approaches [13, 15] confirmed a good validity of the classical result (4). Therefore, we keep use the term "theoretical strength" as a more relevant one.

During the last 30 years, many types of *empirical interatomic potentials* were proposed as Johnson, Morse, Born-Mayer, Lennard-Jones, Stillinger-Weber, ionic, polynomial, etc. Empirical parameters in these potentials are to be established by fitting to experimental data on equilibrium lattice parameter a_0, elasticity constants C_{ij} or cohesive energy U_0. For more extensive historical overview of empirical approaches to TS see, e.g. [1, 14, 16]. In the last 25 years, *semiempirical potentials* constructed according to either Finnis and Sinclair scheme (FS) [17] or embedded-atom method (EAM) [18] became very popular for modelling extended lattice defects like grain boundary structure in alloys. The FS potential was constructed for many types of binary alloys reproducing exactly the values a_0, c_{ij}, U_0, the vacancy formation energies U_v as well as the stacking fault energies U_{sf} [19]. The EAM potentials allow exact fits to elastic moduli of the third order C_{ijk} and yield also reasonable phonon frequency spectra [20].

The values of a_0, C_{ij} and C_{ijk} characterise the closest vicinity of the unstressed equilibrium state and the quantities U_0, U_v and U_{sf} are of integral character. The TS value, however, corresponds typically to the 10 - 20 per cent atomic stretch from their equilibrium (unstressed) lattice. Therefore, approaches based on electronic structure calculations – so called *ab initio* (or first principles) methods – started to appear since 1980 [21]. They deal with approximate solutions of many-particle Schrödinger equation for solid crystal and enable the calculation of the energy-strain curve *without any experimental calibration at all*. Assumptions like the adiabatic approximation, density functional theory, variation principle and tight-binding approximation are commonly used in the models [22]. The last approximation enables to use various systems of basic functions for the description of one-electron atomic waves. It leads to a number of methods like, e.g., Augmented Plane Wave (APW), Discrete Variational cluster Method (DVM) or Muffin-Tin Orbitals (MTO). Methods based on Green functions, as Koringa-Kohn-Rostocker, or on various pseudopotentials are also frequently used. Generally, such approaches request advanced computers and a lot of computation time. On the other hand, computational methods as the full potential linear augmented plane waves (FLAPW) or, the less general linear muffin thin orbitals (LMTO), can be successfully applied without extraordinary demands on computer level or time. The FLAPW method is among the most accurate methods for electronic structure calculations. It is a procedure solving the Kohn-Sham equations for the ground-state density, total energy and eigenvalues of many-electron system by introducing the basic functions especially adapted to the problem. The lattice unit cell is divided into the non-overlapping atomic spheres (centred at the atomic sites) and the interstitial region. The potential is expanded in the following form

$$V(r) = \sum_{lm} V_{lm}(r) Y_{lm}(r) \quad \text{inside sphere}$$

$$V(r) = \sum_{K} V_K e^{iKr} \quad \text{outside sphere}$$

where l, m are quantum numbers. Inside the atomic sphere a linear combination of radial functions $V_{lm}(r)$ times spherical harmonics Y_{lm} is used unlike a plane wave expansion in the interstitial region outside spheres. The LMTO approximation of LAPW retains only the $l = m = 0$ component inside the sphere (spherical average) and the $K = 0$ outside (volume average). This method is particularly useful in solving the high-symmetry problems as, e.g., the hydrostatic loading of cubic.

3. The State of the Art

For the present, the ab initio approaches are able to yield a sufficiently precise prediction of the mechanical behaviour far enough from the unstressed equilibrium states. However, they have to be supplemented by an assessment of the mechanical stability of the loaded system.

A general stability condition for a quasi-stationary stressed system leads to the requirement that the free energy (and at $T = 0$ also the total internal energy) be minimum in subsequent constant stress ensembles in accordance with the second law of thermodynamics [23–25]. If the solid is infinitesimally strained by ε_{ij} from a reference state associated with the stress σ_{ij} (in the standard notation), the related Cauchy (true) stress t_{ij} can be expressed as

$$t_{ij} = \sigma_{ij} + B_{ijkl}\, \varepsilon_{kl}, \tag{6}$$

where

$$B_{ijkl} = C_{ijkl} + \frac{1}{2}(\delta_{ik}\sigma_{jl} + \delta_{jk}\sigma_{il} + \delta_{il}\sigma_{jk} + \\ + \delta_{jl}\sigma_{ik} + 2\delta_{kl}\sigma_{ij}) \tag{7}$$

is the elastic stiffness matrix ($i, j, k.l = 1, 2, 3$), generally asymmetric towards $(ij) \leftrightarrow (ji)$ interchange. Construction of this matrix is crucial for stability assessment. Namely, the system can be considered to be unstable when it holds

$$det\,|\boldsymbol{B}| = 0 \tag{8}$$

for the first time during the loading. It should be emphasized that the elastic moduli in eq. (7) are the local ones, corresponding to each point on the deformation path. Their values should be determined by introducing a sufficient number of independent small deviations (strain increments) from the original deformation path in each of its points. The solution of eq. (8) yields a different number of possible stability conditions for different crystal lattice symmetries as well as different loading modes. The lowest possible number of necessary stability conditions (only two) corresponds to the isotropic solid.

For example, in case of hydrostatic loading of a cubic crystal one can write $C_{11} \neq 0$, $C_{12} \neq 0$, $C_{44} \neq 0$, and $C_{ij} = 0$, others and the simple relation $\sigma_{ij} = \sigma\, \delta_{ij}$ holds for the stress tensor. By introducing these relations to eq. (8), one obtains the following stability conditions [23]:

$$C_{11} + 2C_{12} - \sigma > 0,$$

$$C_{11} - C_{12} + 2\sigma > 0,$$

$$C_{44} + \sigma > 0.$$

The first condition prevents the bulk modulus from vanishing (or getting negative) during the loading. Obviously, the left-hand side differs from the bulk modulus for the stress-free state $\sigma = 0$ only by a multiplication constant. The violation of this criterion is directly related to the inflexion point on the energy-strain curve and, therefore, no special tests along the deformation path are needed for its analysis. Conditions (9b) and (9c) are related to the vanishing of shear moduli and need special tests.

In general, two basic cases of instability behaviour related to the TS can be distinguished when analysing the crystal deformation:

i) the instability occurs along the original deformation path,
ii) the instability changes the loading mode or the type of the deformation path.

The first kind of instability means that the process of unstable crystal collapse starts at the point of inflexion on the same (original) deformation path. Assuming the constant stress ensembles (i.e. the stress-controlled loading), the crystal starts to spontaneously disintegrate after reaching this point. During the process, however, strain induced phase transformations (so-called displacive transformations) may appear along the deformation path [26–28]. They are of the first order and, therefore, accompanied by a symmetry-dictated extrema on the stress-strain curve. Consequently, more "TS values" can be found related to different points of inflexion on the energy-strain curve. *The TS is determined by the stress associated with the first point of inflexion on the original strain-energy curve.* All other inflexion points are preceded by a break down of at least one stability condition.

The second-kind instability occurs before reaching the first point of inflexion on the original energy-strain curve. It changes the type of the deformation path (e.g. the bifurcation from the tetragonal to the trigonal tensile path in the uniaxial tensile test of fcc crystals) or it may simply cause a change in the loading mode (e.g. from the tensile to the shear or vice versa). In that case, *the TS corresponds to the stress related to the point of the first break down of a stability condition preceding the point of inflection.*

Beside the violation of mechanical stability conditions, some phonon instabilities may be expected along the deformation path [28]. Unfortunately, a too limited number of relevant papers has appeared until now in order to be able to present a more general statement concerning the role of the phonon resonance in the TS analysis. Thus, the currently used methodology for calculating the TS of the particular crystal can be summarised into the following points:

1. Construction of a suitable empirical interatomic potential or calculation of the electronic structure.
2. Calculation of the strain-energy curve and the related stress-strain curve for the specific deformation path.
3. Formulation of stability conditions and calculation of their left-hand side values as functions of strain.
4. Establishment of elastic and phonon instability ranges on the strain-energy and/or stress-strain curve.
5. Determination of TS value as a stress related to the first point of inflexion or to the first instability point on the stress strain-energy curve.

4. Influence of lattice defects and temperature

In real perfect crystals (whiskers), a presence of some imperfections is to be expected, at least, the equilibrium concentration of vacancies and a certain level of surface roughness. Thus, it seems to be correct to mention the effects of lattice defects, surface roughness and temperature on TS. From the principal reasons, the strength of imperfect crystals can not be called as TS any more. In this paragraph, therefore, only the term „strength" will be used instead of TS.

a) Point defects

Vacancies are inevitable in real crystals just near the zero Kelvin temperature. However, the effect of monovacancies on strength is negligible. It can be clearly seen from the fact that the simple formula (5) for σ_{iut} is equal to the Griffith criterion for a nanocrack of the atomic size – a vacancy. The effect of impurities and alloying atoms on strength was studied in several works based on *ab initio* methods [29–31]. In summary, the influence of a low concentration of point defects on strength seems to be very small.

b) Dislocations

Dislocation slip is possible under shear stresses above the Peierls-Nabbarro stress. The strength might be reduced by 4 orders (or even more) when the P-N stress is as low as in metals,. On the other hand, the P-N stress is extremely high in ceramic covalent crystals (C, Si, SiC, ZnS, Si_3N_4) and complex ionic crystals ($MgAl_2O_4$, Al_2O_3, Al_2O_3.MgO) so that the dislocations are practically sessile at the near zero temperature

[32]. Therefore, only the tensile strength can be reduced by about tens of percents due to microcracks initiating by the stress relaxation around dislocations with long Burgers vectors.

c) Stacking faults

As far as we know, no special studies on the stacking fault (SF) influence on strength were performed. Atoms on the stable SF plane lie in the local energy minimum and no stress is induced in surrounding volume. The energy of the SF per atom is of about two orders lower than that of the free surface. We may, therefore, deduce that the influence of SFs on the strength value can be neglected.

d) Free surface and notches

The effect of perfectly flat surface on strength can be also considered to be negligible. However, just small imperfections like scratches or dimples act as stress concentrators (notches). Their maximum effect on strength value can be roughly estimated by a factor $1+2(l/\rho)^{1/2}$, where l is the notch depth and ρ is the curvature of the notch root ($\rho > 0$) [33].

e) Cracks

According to the Griffith law for perfectly brittle materials, an atomically sharp crack of length a causes the drop in tensile or shear strength values by a factor of $(a/a_0)^{1/2}$ (a_0 is the lattice parameter). However, only ceramics, semiconductors and, most probably, Mo and W can be considered to be intrinsically brittle crystals at zero absolute temperature [4, 5]. In all other metals, the dislocation emission appears before the unstable crack growth. This process increases the effective surface energy and blunts the crack tip. Consequently, the drop in strength must be much less steep than that predicted by Griffith law.

f) Phonons (temperature)

The strength variation with temperature corresponds, basically, to the problem of the role of phonons in deformation and fracture processes. Although the Frenkel expression (4) suggests simply that the variation should be the same as that of the shear modulus, the eq. (5) brings the complication with the temperature dependence of surface energy. The first approaches predicted the drop in the uniaxial strength within the range of several to tens of percents when changing the temperature from 0 K to 1000 K, depending on the type of the empirical interatomic potential used (short- or long range). Very recent ab initio studies [34] suggest that some phonon instabilities can be coupled with a violation of some shear stability conditions. In general, one can assume that the temperature change in the relevant elastic modulus might be considered to be an acceptable lower-band first approximation to the strength temperature dependence.

5. Theoretical and experimental results

Owing to the long history of TS calculations, a number of theoretical results concerning crystals of pure elements and compounds is available in literature. On the other hand, the experimental data are still rather limited owing to problems associated with both the specimen preparation and the experimental arrangement. It holds especially for experiments focused on the shear τ_{is} and the three-axial σ_{iht} – in the latter case, there is even a lack of any value. Selected theoretical and experimental TS values for various crystals are presented in Tab. 1.

There is a three-order difference between the strongest and the weakest crystal. As expected, the highest TS values exhibit a diamond crystal with pure covalent bonds and the lowest ones belong to Van der Waals crystals of inert gases stable only in a low temperature range. It should be emphasized, however, that a great majority of σ_{iut} values corresponds to the inflexion point on the energy-strain curve and the stability analysis was omitted. Those values are most probably overestimated. On the other hand, the stability analysis applied to cubic crystals under hydrostatic tension has revealed that, in most cases, no shear instability appeared before reaching the inflexion point [36]. Therefore, values σ_{iht} obtained by *ab initio* (LMTO-ASA) method can be considered to be very reasonable estimations of TS. A comparison between σ_{iht} values obtained by *ab initio* LMTO-ASA/LDA calculation and those obtained by empirical approaches is displayed in Fig. 1 for selected crystals. It is clear that, in most cases, the sinusoidal potential overestimates the TS, whereas the Morse approximation underestimates the TS. Results well comparable with the ab initio calculations can be obtained by means of the polynomial potential. The computed τ_{is} values are lowest for fcc crystals. Most experimental data obtained on perfect large monocrystals or even on thin whiskers in uniaxial tension are of an order lower than calculated TS values. It might be dedicated to the dislocation assisted shear instability controlling the final fracture process. The very high Peierls-Nabarro stress in covalent and complex ionic ceramic crystals resists to nucleation and motion of dislocations. For such crystals, indeed, the difference between theory and experiment is relatively low. The probably highest ever reported experimental value $\sigma_{iut} = 40$ GPa $\approx E/20$ corresponds to the ZnO whisker

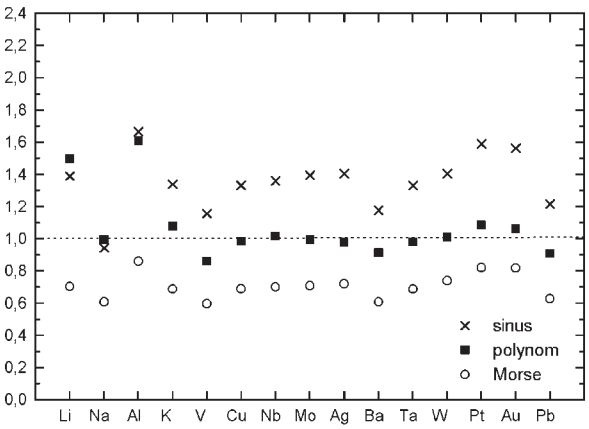

Fig. 1 Comparison of ab initio calculation of threeaxial theoretical strength using LMTO ASA (reference dotted line) with calculations based on selected empirical potentials.

[14]. The gap between the theory and the experiment for metallic crystals becomes much lower by taking the stability conditions into account (e.g. for Cu crystal [53]), but still remains to be high. This can be understood particularly in terms of various imperfections of experimental procedure, including the crystal defects discussed above. Additionally, there is resonance of short- wavelength phonons and its possible coupling with reaching the shear TS in a significant crystallographic shear system. All such effects are clearly beyond the description supplied by the mechanical stability conditions based on the theoretical continuum mechanics. Let us note, finally, that the currently used ultra-high strength steels exhibit only $\sigma_{iut}/10$ value of ultimate strength. From the the-

Calculated and measured values of theoretical strength Tab. 1.

Crystal	Latt.	Threeaxial TS [GPa]	Uniaxial TS [GPa]		Shear TS [GPa]	
		theory	theory	experiment	theory	experiment
Na	bcc	2.0 A [37] 1.5 A [40] 1.2 E [16]	0.04<100>E [14] 0.2 <110>E [14] 0.9 <111>E [14]		0.21<111>E [13] 0.20<111>A [41]	
Si	dia	20.5 A [37] 25.0 E [16]	22.4<100>E [14] 47.3<111>E [14] 24.8<111>A [51]	4.14 [14] 7.60 [14]	13.7<100>E [1] 14.7<110>E [13]	
C	dia	54.0 A [39] 138 E [16]	168<100>E [14] 205<111>E [14] 90<111>A [42] 95<111>A [43] 130<100>A [42]	20.7(graph.) [14] 19.6(graph.) [1]	131<110>E [13]	
Cu	fcc	29.0 A [37] 19.9 E [16]	41 <100>E [21] 39 <111>E [14] 31 <110>A [44] 29 <111>A [44] 9.3<100>A [35]	1.25 <111> [1] 2.94 <111> [14] 1.50 <100> [14] 1.74 <100> [14] 1.59 <110> [14]	1.2 <112> E [1] 2.9 <112> E [13] 4.0 <112> A [41] 2.7 <112> A [41]	0.80<011> [1]
Fe	bcc	42.5 A [36] 24.1 E [16] 21.5 E [16]	48.0<111>E [16] 30.0<100>E [16] 13 <001>A [47]	13.1 <111> [1]	7.3 <111> E [14] 6.6 <111> E [1] 11.5 <111> E [13]	3.56<111> [1]
Ti	bcc		9.5 <100>E [44]			
W	bcc	53.1 A [46] 56.8 A [37] 42.2 E [16]	61<100>E [16] 29.5<100>A [49] 54.3<110>A [48] 40.1<111>A [48]	24.7<100> [14]	18.2 <111> E [14] 18.1 <111> A [41]	
Pb	fcc	8.47 A [39] 5.47 E [16]			0.47 <112> E [13]	
Ar	fcc	0.25 E [14] 0.15 E [16]	0.35<100>E [16] 0.35<111>E [16]		0.14 <110> E [13] 0.08 <112> E [13]	
TiC	B1		44<001>A [50]			
NaCl	B1	4.3 E [14] 3.4 E [16]	4.6<111>E [16] 12.4<110>E [14] 4.3<100>E [14]	1.08 <100> [14]	3.2 <110>E [18] 2.3 <112> E [14]	
MgO	B1	8.5 E [16]	37<100>E [16]	23.7 bend. [14]	32.0 <110> E [13]	
Ni_3Al		28.1 A [35]	17.5<100>A [52] 28<111>A [52]			
$\beta-Si_3N_4$	P63m		57 E <100> [17]	13.5<100> [14] 14<100> [1]		
Polyeth.			26 E [1]	3.04 [14]		
Kevlar				2.8-3.6 [1]		

A – ab initio, E – Empirical

oretical point of view, however, materials of an extreme dislocation density could, in principal, achieve the strength level of $\sigma_{iut}/2$ [54].

6. Conclusion

In the recent time, a significant advance in the solution of theoretical strength problem has been achieved by application of *ab initio* methods based on electronic structure calculations. A significant success was achieved also by description of extended crystal defects, as grain boundary structures and metastable phases, by means of *ab initio* supported semi-empirical potentials. From the theoretical point of view, the following items remain to be the main challenges in the near future: *i) ab initio* supported semiempirical potentials, *ii)* extended application and improvement of stability conditions including phonon resonance, *iii)* the first principle TS studies. In the experimental field, the nanoindentation technique seems to be very promising at least for testing the shear TS. It is also to hope that the technological progress would enable tensile experiments on large perfect crystals by means of (nearly) perfect loading devices. This seems to be even the most crucial point in the future evolution of TS investigations.

7. Acknowledgement

This work was done in the framework of the research intention "Advanced functionally graded and nanostructural materials" MSM 262100002 of the Brno University of Technology supported by the Ministry of Education, Youth and Sport of the Czech Republic.

References

[1] KELLY, A., MACMILLAN, N. H.: *Strong Solids*. Clarendon Press, Oxford 1986.
[2] JOKL, M. L., VITEK V., MCMAHON JR., C. J.: *Acta Metall.* 28 (1980), 147.
[3] THOMSON, R.: *Sol. State Physics 39* (1986), 1.
[4] POKLUDA, J., ŠANDERA, P.: *Phys. Stat. Solidi* 167b (1991), 543.
[5] POKLUDA, J., ŠANDERA, P.: *Key Engng. Mater.* 97-98 (1994), 467.
[6] BAHR, D. F., KRAMER, D. E., GERBERICH, W. W.: *Acta Mater.* 46, 3605 (1998).
[7] GOULDSTONE, A., KOH, H. J., ZENG, K. Y., GIANNAKOPOULOS, A. E., SURESH, S.: *Acta Mater.* 48, 2277 (2000).
[8] GOLDSCHMIDT, D.: In: *Materials for Edvanced Power Engineering* 1994, Eds. D. Coutsouradis et al. Part I. Dodrecht, Kluwer Academic Publishers 1994, p. 661.
[9] WALLACE, D. C., ED.: T*hermodynamics of Crystals.* Lohn Willey & Sons, New York-London-Sydney-Toronto 1972.
[10] FRENKEL, J.: Z. *Phys.*, 37 (1926), 572.
[11] OROWAN, E.: *Rep. Progr. Phys.*, 12 (1949), 185.
[12] KELLY, A.: *Strong Solids.* Clarendon Press, Oxford 1973.
[13] ŠANDERA, P., POKLUDA, J.: *Scr. Met. Mater.* 29 (1993), 1445.
[14] MACMILLAN N. H.: In "*Atomistics of Fracture.*" Eds. R.M.Latanision and J.R.Pickens, Plenum Press, New York 1983, p. 95.
[15] PAXTON, A. T., GUMBSCH, P., METHFESSEL, M.: *Phil. Mag. Lett.* 63 (1991), 267.
[16] ŠANDERA, P., POKLUDA, J.: Kov. Mater. 32 (1994), 180.
[17] FINNIS, M. W., SINCLAIR, J. E.: *Phil. Mag.* A, 50 (1984), 45.
[18] ADAMS, J. B.. FOILES, S. M.: *Phys. Rev.* B 41, 3316 (1990).
[19] LUZZI, D. E., YAN, M., ŠOB, M., VITEK, V.: *Phys. Rev. Lett.* 67, 1894 (1991).
[20] CHANTASIRIWAN, S., MILSTEIN, F.: *Phys. Rev.* B 67, 14081 (1996).
[21] ESPOSITO, E., CARLSON, A. E., LING, B. D., EHRENREICH, H., GELATT, JR., C. D.: *Phil Mag.* A41 (1980), 251.
[22] TUREK, I., DRCHAL, V., KUDRNOVSKÝ, J., ŠOB, M., WEINBERGER, P.: *Electronic Structure of Disordered Alloys,* Surfaces and Interfaces. Kluwer, Boston 1997.
[23] ZHOU, Z., JOÓS, B.: *Phys. Rev.* B 54, 3841 (1996).
[24] MORRIS, J. W., KRENN, C. R.: *Phil. Mag.* A 80, 2827 (2000).
[25] YIP, S., LI, J., TANG, M., WANG, J.: *Mater. Sci.* Eng. A317, 236 (2001).
[26] CRAIEVICH, P. J., WEINERT, M., SANCHEZ, J. M., WATSON, R. E.: *Phys. Rev.* Lett. 72, 3076 (1994).
[27] ŠOB, M., WANG, L. G., VITEK, V.: *Comp. Mat.* Sci. 8, 100 (1997).
[28] SHIBUTANI, Y., KRASKO, G. L., ŠOB, M., YIP, S.: *Mater. Sci.* Res. Int. 5, 225 (1999).
[29] GOODWIN, L., NEEDS, R., HEINE, V.: *Phys. Rev.* Lett., 60 (1988), 2050.
[30] HUANG, Y. M., SPENCE, J. C. H., SANKEY, O. F.: *Phil. Mag.*, 70 (1994), 53.
[31] SONG, Y., XU, D. S., YANG, R., LI, D., WU, W. T., GUO Z. X.: *Mater. Sci.* Eng. A260 (1999), 269.
[32] POKLUDA, J., KROUPA, F., OBDRŽÁLEK, L.: *Mechanical Properties and Structure of Solids.* PC Dir, Brno 1994 (in Czech).
[33] NEUBER, H.: *Kerbspannungslehre.* Springer Verlag, Berlin 1958.
[34] MA, Y., TSE, J. S., KLUG, D. D.: *Phys. Rev.* B 67, 140301(R) (2003).
[35] ČERNÝ, M., ŠOB, M., POKLUDA, J., ŠANDERA, P.: In: *Proc. ICSMA* 13 (submitted).

[36] ČERNÝ, M., POKLUDA, J., ŠANDERA, P., ŠOB, M.: *Phys. Rev.* B 67, 035116 (2003).
[37] ŠANDERA, P., POKLUDA, J., WANG, L. G., ŠOB, M.: *Mater. Sci.* Eng. A234-236 (1997), 370.
[38] CLATTERBUCK, D. M., CHRZAN, D. C., MORRIS, JR., J. W.: *Phil. Mag.* Lett. 82, 141 (2002).
[39] ČERNÝ, M., ŠANDERA, P., POKLUDA, J.: *Czech. J. Phys.* B49 (1999), 1495.
[40] MILSTEIN, F., RASKY, D. J.: *Phys. Rev.* B 54, 7016 (1996).
[41] MORRIS JR., J. W., KRENN, D., ROUNDY, D., COHEN, M. L.: In: *2000 Hume-Rothery Symp.* in honor of A. G. Khatchaturyan Eds.: Turchi, P. E. and Gonis, A., TMS, Warrendale, PA, 2000 pp. 187-207.
[42] TELLING, R. H., PICKARD, C. J., PAINE, M. C., FIELD, J. E.: *Phys. Rev.* Lett. 84, 5160 (2000).
[43] ROUNDY, D., COHEN, M. L.: *Phys. Rev.* B 64, 212103 (2001).
[44] ŠOB, M., WANG, L. G., VITEK, V.: *Kov. Mater.* 36 (1998), 145.
[45] ČERNÝ, M., ŠANDERA, P., POKLUDA, J.: In: *Proc. ICSPMA 2003* (to be published).
[46] SON, Y., YANG, R.: *Phys. Rev.* B59 (1999), 14220.
[47] FRIJÁK, M., ŠOB, M., VITEK, V.: In: *Juniormat '01, Institute of Materials Engineering,* Brno University of Technology, Brno 2001, pp. 117-120.
[48] ŠOB, M., WANG, L. G., VITEK, V.: *Mater. Sci.* Eng. A 234-236, 1075 (1997).
[49] ROUNDY, D., KRENN, D., COHEN, M. L., MORRIS JR., J. W.: *Phil. Mag.* A 81, 1725 (2001).
[50] PRICE, D. L., COOPER, B. R., WILLS, J. M.: *Phys. Rev.* B 46, 11368 (1992).
[51] VERMA, M. V., VERMA, A., RATHERE, R. P. S.: *Acta Phys. Polon.* A93 (1998), 479.
[52] ŠOB, M.: In: *Proc. ICSMA 13* (to be published).
[53] ČERNÝ, M., ŠOB, M., POKLUDA, J., ŠANDERA, P.: *J. Phys. Cond. Matter* 16 (2004), 1045.
[54] KROUPA, F.: In: *Prediction of Mechanical Properties of Metallic Materials by means of Structural Characteristics.* Eds. J. Pokluda and P. Staněk. VÚ070 Brno, 1981, p. 32 (in Czech).

Stanislav Věchet – Jan Kohout – Klára Hanzlíková *

FATIGUE PROPERTIES OF ADI IN DEPENDENCE ON ISOTHERMAL TRANSFORMATION DWELL

As a result of excellent both mechanical and technological properties, austempered ductile iron (ADI) is ranked with very perspective structural materials. Recently it has been applied even to castings for dynamically loaded components and a considerable part of ADI production is applied also in military industry. The structure of ADI matrix, mostly created by the mixture of bainite and stabilized austenite, strongly depends on transformation conditions, i.e. temperature and the length of isothermal transformation dwell. An ADI transformed at 380 °C during a temporal range from 2 minutes to 9 hours was studied in details, with emphasis on structural composition and fatigue properties. The highest level of fatigue properties was obtained for the transformation dwell of 60 minutes when the maximum portion of austenite was found in ADI structure.

1. Introduction

Austempered ductile iron (ADI) is usually made using isothermal heat treatment. Owing to its excellent mechanical as well as technological properties, ADI belongs among prospective structural materials. Recently it has also been applied to castings for strongly dynamically loaded machine details, e.g. gear and traversing wheels, crankshafts of motor-cars, vans and trucks, swivel pins, rail brakes, pressure pipes in oil industry [1, 2]. A considerable part of ADI production is applied in military industry, e.g. in 1995 about 3 % of total ADI production in U.S.A. were used for military reasons [2]. ADI castings are preferably applied in the following cases [3]:

1. The most usual case is the substitution of a detail made of steel (forged piece, workpiece or weldment) when the design remains the same as the design of original detail or only slight changes of the design have been done.
2. Occasionally nodular cast iron with lower level of strength properties (usually with pearlitic matrix) is substituted with ADI to increase loading capacity and/or service life of cast detail.
3. In the case when a new detail is designed specially for ADI application (above all when a complex of heat treated details is substituted with only one ADI casting, e.g. steering swivel pin in motor-cars), the highest effect with the largest savings is obtained.

Microstructure and mechanical properties of ADI can be substantially influenced by the condition of heat treatment. While the austenitization conditions (usual austenitization temperature is from the region of 880 to 920 °C and typical dwell is 1 to 3 hours) play only a marginal role, the conditions of isothermal transformation, i.e. transformation temperature and the dwell at this temperature, influence the resulting structure of ADI and consequently its mechanical properties very substantially [4 – 8]. The present paper is devoted to the study of how the dwell of isothermal transformation in the range of 2 minutes to 9 hours influences the structure as well as the static and fatigue properties of unalloyed ADI transformed at temperature of 380 °C.

2. Experimental material and techniques

Heat of unalloyed nodular cast iron with chemical composition 3.49 wt. % C, 2.46 % Si, 0.25 % Mn, 0.02 % P, 0.007 % S, and 0.042 % Mg was selected for the study. Austenitization at 900 °C during 1 hour was followed by isothermal transformation in AS 140 salt bath at 380 °C. The dwell at transformation temperature varied in the range from 2 minutes to 9 hours in order to study the dependence between the obtained structural mixture (upper bainite, retained austenite, and martensite if any) and its mechanical properties. Heat treatment was applied to test bars (with the diameter of 6 mm for static tests and of 7 mm for fatigue tests) with small grinding allowance.

The content of retained (stabilized) austenite was determined using quantitative X-ray phase analysis. Basic mechanical properties (yield stress $R_p0.2$, ultimate tensile stress R_m, and elongation to fracture A_5) were measured using universal loading device of the Zwick Company at room temperature.

For fatigue tests the high frequency pulsator of the Amsler Company was used. Ground test bars with surface roughness of 0.4 μm were loaded symmetrically in tension-compression at room temperature. The testing frequency of a resonant pulsator, which is significantly dependent on the sample stiffness, was about 202 Hz for all the tested materials. Each of S-N curves was determined by the tests of 12 to 15 test bars. For their regression by the least square method the three-parameter non-linear function proposed by Stromeyer [9] and recommended by Weibull [10]

* **Stanislav Věchet[1], Jan Kohout[2], Klára Hanzlíková[1]**
[1]Institute of Materials Engineering, Faculty of Mechanical Engineering, Brno University of Technology, Technická St 2, CZ-616 69 Brno, Czech Republic
[2]Department of Physics, Military Technology Faculty, Military Academy in Brno, Kounicova St 65, CZ-612 00 Brno, Czech Republic

$$\sigma = a\,N^{b} + K \qquad (1)$$

was used, where as σ stress amplitude or maximum stress of loading cycle can be considered, a, b, K are parameters of regression curve, and N is the number of cycles to failure or to test stoppage.

3. Results

Established structural composition, average values of static mechanical characteristics, and by using Eq. (1) calculated values of the fatigue limit for reference number to failure $N_C = 10^7$ are presented for all the studied materials in Table 1.

Content of retained austenite or martensite (if any), static mechanical properties, fatigue limit, and fatigue ratio of ADI transformed at 380 °C in dependence on the dwell of isothermal transformation. Table 1

sign	τ_t		A_R	M	R_p 0.2	R_m	A_5	σ_C	σ_C / R_m
	[min]	[h]	[vol. %]	[vol. %]	[MPa]	[MPa]	[%]	[MPa]	[-]
A	2		9.5	61.2	-	700	0.0	184	0.263
B	5		24.0	36.6	736	896	0.5	188	0.209
C	10		27.4	5.0	607	977	2.1	200	0.204
D	25		31.7	0.0	675	973	3.8	199	0.204
E	60	1	36.0	0.0	772	1022	8.1	231	0.225
F	120	2	22.6	0.0	811	1001	6.7	–	–
G	270	4.5	4.3	0.0	824	990	5.9	230	0.233
H	540	9	0.0	0.0	824	1055	5.0	179	0.170

As shown in Table 1 and Fig. 1, the composition of structural mixture in the matrix of ADI transformed at 380 °C is strongly influenced by the dwell of isothermal transformation. The structure mostly consists of upper bainite and retained austenite, only when short transformation dwells are applied then also martensite is present in the structure (in the case of the shortest dwell, i.e. 2 minutes, even as a dominating structural component). With increasing length of transformation dwell the martensite content decreases very quickly and for transformation dwell of 10 minutes only its debris were found. The content of retained austenite increases reaching for its maximum at transformation dwell of 1 hour. Then it decreases and at the longest dwell (9 hours) no retained austenite is present in ADI structure.

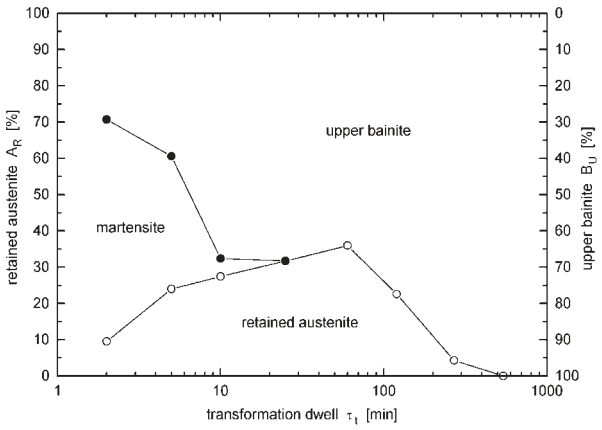

Fig. 1: Structural composition of ADI in dependence on the length of transformation dwell.

As the fatigue behaviour of ADI is the main object of this paper, the results of fatigue tests are presented at first and in more details. The latest results obtained by testing BH 27 G material, i.e. the ADI transformed during the dwell of 270 minutes, are presented together with fitted S-N curve in Fig. 2. This figure demonstrates a typical scatter of ADI fatigue tests and their fit using Eq. (1). Comparison of fitted S-N curves for nearly all transformation dwells is presented in next two figures: for the dwells of 60 minutes and a shorter one in Fig. 3, for the dwells of 60 minutes and a longer one in Fig. 4. The 60-minute dwell was chosen as a braking point because it leads to the highest fatigue limit. Unfortunately, the fatigue tests of the ADI transformed during the dwell of 120 minutes, which presage very promising results, are not finished yet.

Similarly as the composition of structural mixture of ADI matrix, also the length of isothermal dwell in salt bath substantially influences static and fatigue properties, see Table 1 and Fig. 5. Not considering small waviness, UTS and yield stress increase with an increasing length of transformation dwell and reach maxima for the longest dwells, with the only exception of yield stress value at transformation dwell of 5 minutes. Elongation to fracture, in contrast to both the stress characteristics, increases at first but after reaching for maximum of 8.1 % at dwell length of 60 minutes a slight decrease follows. Maximum of fatigue limit is reached at the same dwell but the value for 270-minute dwell is only negligibly lower, see also fully comparable high-cycle parts of S-N curves for both mentioned dwells in Fig. 4. Comparing with retained austenite content, the increases of elongation to fracture as well as of fatigue limit are very closely connected with the increase of

austenite content for increasing transformation dwell up to 60 minutes. On the other hand, for longer dwells the decrease of elongation to fracture and namely of fatigue limit is considerably delayed with respect to the decrease of austenite content.

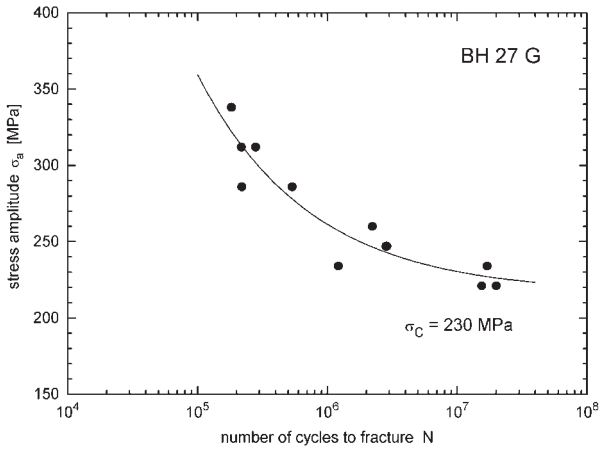

Fig. 2: S-N curve of ADI transformed at 380 °C for the dwell of 270 minutes.

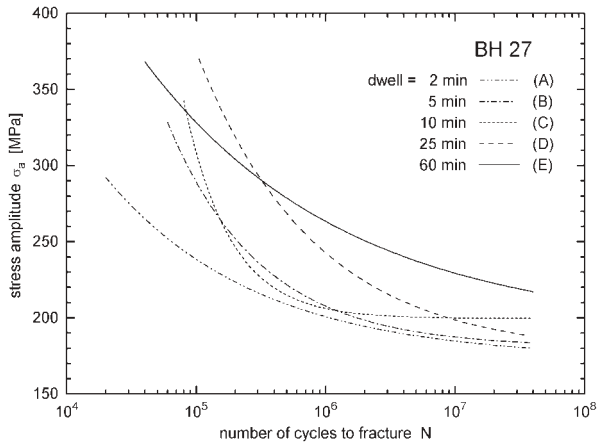

Fig. 3: Comparison of S-N curves of ADI for various lengths of transformation dwell (up to 60 minutes).

4. Discussion

Presented results show an already described fact [11, 12] that, in contrast to most structural steels and cast irons, increasing UTS is not followed by increasing fatigue limit in the case of ADI. The maxima of elongation to fracture, of fatigue limit, and of austenite content obtained at the same value of transformation dwell (60 minutes) are evidence of certain internal connection among these quantities. Retained austenite is an extremely deformable structural component of ADI and, therefore, the maximum content of austenite means maximum deformability expressed through the elongation to fracture. Then fatigue, which is considered to be an accumulation of plastic deformation, should be closely dependent on the content of retained austenite. High values of fatigue limit were also determined for ADI structures with a high content of retained austenite, which isothermally transformed at 400 °C [13].

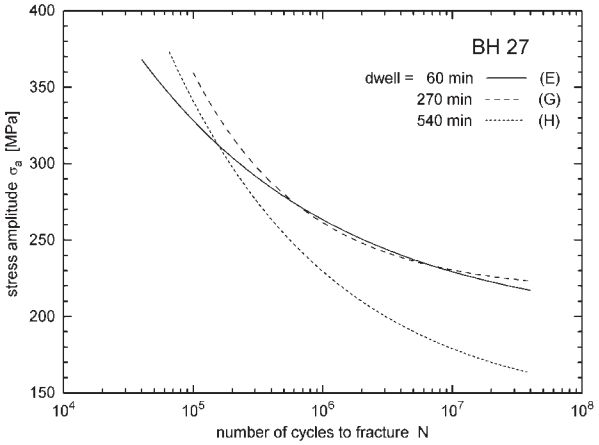

Fig. 4: Comparison of S-N curves of ADI for various lengths of transformation dwell (60 minutes and longer).

While strong decrease of austenite content with increasing transformation dwell above 60 minutes is followed by moderate decrease of elongation to fracture, the fatigue limit decreases in

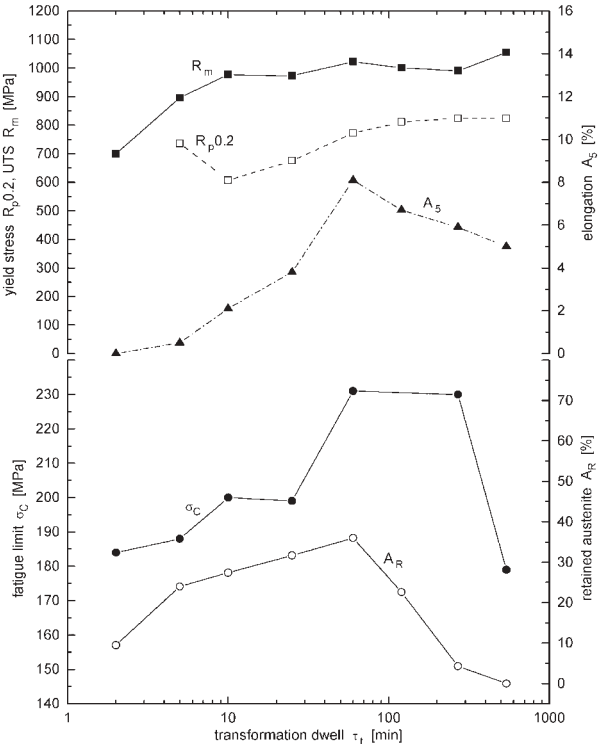

Fig. 5: Dependence of yield stress, UTS, elongation to fracture, retained austenite content and fatigue limit of ADI on the length of transformation dwell.

fact only for dwells longer than 4.5 hours, see Fig. 5. It means that not only the content of retained austenite contributes to relatively high values of fatigue limit. More information will be obtained after finishing the fatigue tests for the 120-minute dwell, now the other factors raising fatigue limit can be only suspected. In phenomenological considerations two following facts can be considered:

(i) The increase of elongation to fracture with increasing austenite content is higher than the following decrease of the elongation with decreasing austenite content.
(ii) Stress characteristics, i.e. UTS and yield stress, increase with increasing transformation dwells in fact in the whole studied range of transformation dwells.

Then slower decrease of deformability together with continued increase of stress characteristics could lead to nearly constant level of fatigue limit.

The root of slightly decreasing fatigue limit with substantially decreasing austenite content in dwell range from 60 to 270 minutes consists probably in increasing deformability of bainitic ferrite with increasing length of transformation dwell. The mechanisms of this increase should be the same or similar to those applied in martensite during its tempering at not very high temperatures. To support this idea, the tetragonality of bainite should be determined in dependence on the transformation dwell, which is planned for the future.

5. Conclusions

Summarizing the obtained results and their analysis, the following items can be asserted:

1. The length of isothermal transformation dwell very substantially influences the composition of structural mixture in the matrix of ADI transformed at 380 °C.
2. Maximum content of retained austenite was obtained in the ADI structure for transformation dwell of 60 minutes.
3. UTS and yield stress values increase with increasing transformation dwell practically in the whole studied range of transformation dwells.
4. Maximum elongation to fracture of about 8 % was measured for transformation dwell of 60 minutes corresponding with the maximum content of retained austenite.
5. The length of isothermal transformation dwell strongly influences also fatigue limit. Optimum fatigue properties were obtained for the transformation dwell, for which ADI structure contains the maximum amount of retained austenite, i.e. for 1 hour.
6. High level of fatigue limit appears also when austenite content starts to decrease. The reason of this effect is probably increasing deformability of bainitic ferrite with increasing transformation dwell.
7. Technological window in transformation dwells to obtain high fatigue limit was found in the range from 1 to 4.5 hours.
8. Low values of fatigue limit for short transformation dwells are the consequence of martensite presence as well as low content of retained austenite in ADI matrix.

Acknowledgement

Presented studies were partially supported by the grant projects 106/01/0376 and 106/03/1265 of the Grant Agency of the Czech Republic.

References

[1] HUGHES, I. C. H.: Brit. Foundryman vol. 74, 1981, p. 229
[2] KEOUGH, J. R.: Foundry Management and Technology vol. 123, 1995, Nr. 11, p. 27
[3] DORAZIL, E.: *High Strength Austempered Ductile Cast Iron.* Academia and Horwood, Praha and Chichester, 1991, 228 p. and 20 p. suppl.
[4] DORAZIL, E., PODRÁBSKÝ, T., ŠVEJCAR, J.: *Influence of chemical microhomogeneity on structure and properties of low-alloyed isothermally heat treated ductile iron.* Slévárenství vol. 40, 1990, Nr. 6, pp. 342-353 (in Czech)
[5] HORNUNG, K.: Heat Treatment of Metals 1986, Nr. 4, pp. 87-94
[6] JOHANSSON, M., VESANEN, A., RETTIG, H.: *Austenite-bainite iron with nodular graphite as structural material in gear box construction.* Antriebstechnik vol. 15, 1976, Nr. 11, pp. 593-600 (in German)
[7] NIETH, F., WIEGAND, H.: Giesserei-Forschung vol. 29, 1977, p. 131 (in German)
[8] PODRÁBSKÝ, T., DORAZIL, E.: *Behaviour of austenite in bainite of silicon steel and nodular cast iron under static loading.* Giesserei-Praxis 1991, Nr. 8, pp. 135-145 (in German)
[9] STROMEYER, C. E.: *The determination of fatigue limits under alternating stress conditions.* Proc. Roy. Soc. vol. A90, 1914, pp. 411-425
[10] WEIBULL, W.: *Fatigue testing and analysing of results.* Oxford, London, New York, Paris: Pergamon Press, 1961, 275 p. (also Russian translation exists)
[11] VĚCHET, S.: *Behaviour of ductile cast iron in the conditions of fatigue loading.* Ph.D. Thesis, Brno 1989, Brno University of Technology, Faculty of Mechanical Engineering, 80 p. and 55 p. suppl. (in Czech)
[12] VĚCHET, S., KOHOUT, J.: *High-cycle fatigue properties of nodular cast iron.* Part I, Slévárenství vol. 47, 1999, Nr. 11/12, pp. 638-641. Part II, Slévárenství vol. 48, 2000, Nr. 1, pp. 37-41 (in Czech)
[13] VĚCHET, S., KOHOUT, J.: F*atigue Properties of ADI in dependence on the time of isothermal transformation.* Mechanika 55, Nr. 235/97, Opole 1997, pp. 127-130 (ISSN 0209-0848).

kamUNikácie
COMMUNICATIONS

Milan Růžička *

LOCAL ELASTIC STRESS APPROACH FOR FATIGUE LIFE CALCULATION BY THE FINITE ELEMENT METHOD (FEM)

The paper discusses possibilities of a description of material fatigue and prediction of service life of machine parts on the basis of stress state calculations using the finite element method (FEM). It focuses on the local approach to the assessment of service life that is based on the determination of elastic stress peaks in stress raisers (notches) and on the derivation of the fatigue stress curves for assessed structural points. The method of taking into account the stress concentration and stress gradient during the determination of synthetic fatigue curves is described. Furthermore, methods of processing the loading history and correcting mean stress values of loading cycles are described.

1. Introduction

Material fatigue is one of the important limiting states of structures, during which a fatigue crack can be initiated in a local material volume as a consequence of repeated cyclic loading leading to an undesirable fracture of the entire load bearing cross section of a machine part. At present, the finite element method (FEM) is a standard method for assessing states of structural deformation and stress. There are several commercially available FEM software packages and modules for the subsequent assessment of the fatigue damage can also be purchased. The goal of this paper is to demonstrate certain relations between individual approaches to the assessment of the fatigue service life with the help of the FEM modules and to describe in detail an approach based on local values of elastic stress in notches.

2. Various approaches to the assessment of material fatigue and service life of machine parts

Today, the method based on the elasticity theory and analytical calculations of the stress of mechanical parts and structures can be denoted as a classical approach. This nominal stress approach (NSA) is based on the classification of stress states (tensile stress, bending stress, local stress, etc.) and on the calculation of the stress amplitudes and mean stress values in the assessed critical cross section of a machine part. It assumes the knowledge of the fatigue stress curve ($S-N$ curves) at this point or at least its qualified estimate. If the values of the stress amplitude exceed the fatigue limit, σ_C, determined for this curve, a limited service life of the machine part can be expected. As operational conditions are frequently characterized by a stochastic time course, it is first necessary to obtain single-parametric or multiple-parametric histograms of the stress incidence frequency. At present, the rain flow method and its two-parametric output of the frequency of the incidence of cycles, n_i, into a rain flow matrix, is the method used exclusively in practice for the analysis of loading history. The magnitude of fatigue damage, D, for the loading spectrum processed by this method, is evaluated in most cases using the Palmgren and Miner rule and its modification. It holds that $D = \sum_i \frac{n_i}{N_i}$ for the basic form of this rule, where N_i is the limit number of cycles determined from the $S-N$ curve. In order to improve the accuracy of the calculations for a new generation of products, the results of the experimental tests of the service life of the preceding generation can be used and the rule can be corrected using the ratio of the actual and calculated fatigue damage (the so-called relative Palmgren and Miner hypothesis).

The main disadvantage of NSA is its complicated application in the FEM calculations, because it requires assessment of individual categories of nominal stress values in the assessed cross sections. For this reason, the so-called local approaches are applied. These approaches are based on a thesis that the time until the initiation of a fatigue crack at a critical local point (usually at the root of sharp geometrical notches) is the same as the fatigue life of a sample without notches that is loaded by stress parameters and deformations at a critical local area. These parameters can be determined by the FEM calculations. In the region of a low-cycle fatigue, i.e. approximately up to a service life of $N = 10^4$ up to 10^5 cycles, where the plastic component of the relative deformation should be taken into account, the local plastic stress and strain approaches (LPSA) are used. These methods are based on the use of a strain life curve and damage parameter, P, that is determined according to the local quantities in the notch. The P_{SWT} damage parameter according to Smith, Watson and Topper is used in most cases. These approaches were compared, for example, in Ref. [1]. The disadvantage of these methods is that it is necessary to solve the elastic and plastic problem using FEM or to apply the analytical formulae for the adaptation of the elastic local parameters to the elastic and plastic solutions (the Neuber hyperbola method, the method of equivalent stress energies, etc.).

* **Milan Růžička**
Czech Technical University in Prague, Faculty of Mechanical Engineering, Technická 4, 166 07 Prague 6, Czech Republic.
Telephone: +420 224 352 512, Fax: +420 233 322 482, E-mail: milan.ruzicka@fs.cvut.cz

In the region of a high-cycle fatigue, it is sufficient to use the local elastic stress approach (LESA). The advantage of this approach is that the direct FEM calculations can be used in the elastic region of deformations, which makes it possible to use the superposition of stress values during various loading states of the structure. Some of the most important aspects of this method will be discussed in the following paragraphs, where the method will be compared with the nominal approach.

3. Stress concentration and the stress gradient effect in the notches

It is known that the concentration of nominal, σ_n, stress to the local elastic (virtual), σ_{fic}, stress intensities which are at the root of geometrical notches can be described using a shape factor defined as $K_t = \frac{\sigma_{fic}}{\sigma_n}$. The magnitude of the so-called exposed material volume in which a significant part of the local damage occurs, can be described using the relative stress gradient at the notch root, G, where

$$G = \left[\frac{\Delta\sigma_y}{\Delta x}\right]_{x\to 0} \cdot \frac{1}{\sigma_{fic}} \quad [\mathrm{mm}^{-1}]. \tag{1}$$

If the stress peaks occur along the entire L region (as, for example, in Fig. 1, where L is the sample thickness), the L/G ratio represents the exposed region. For the etalon sample, the ratio of these quantities defines the similarity factor, $\theta = \frac{L/G}{L_0/G_0}$, of the exposed volume.

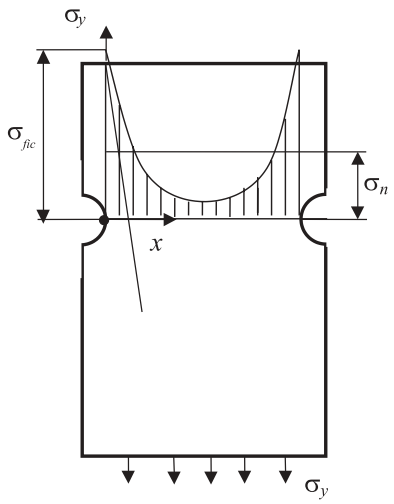

Fig. 1

All these quantities can be determined in the notch locality from the results of the FEM calculations, also during complex loading conditions, when the condition of the multicomponent strain is usually assessed using equivalent stress values according to strength hypotheses, for example, σ_{HMH} according to Huber, Mises and Hencky.

4. The effective notch effect on the fatigue strength

It is also known that the effect of the stress peaks on the notch fatigue strength is not as significant as it would correspond to the theoretical stress concentration. Experiments define the effective notch effect on the fatigue limit by a notch factor, $K_f = \frac{\sigma_C}{\sigma_C^*}$. In the past, several relations were proposed for the computational estimation of the notch factor, which are reviewed, for example, in Ref. [2]. Let us define the ratio of the shape and notch factor by the fatigue ratio, $n = \frac{K_t}{K_f}$. The methods for expressing the n quantity can be split into two major groups. The first group is formed by relations that are determined in dependence on the notch root radius, ρ. The second group involves expressions depending on the magnitude of the relative stress gradient, G. In Table 1, the values of the n_ρ and n_G ratio are indicated for some most frequently used relations.

For the FEM applications, the expression by means of the stress gradient, G, turns out to be more convenient. For the determination of the local fatigue limit in the notch root, $\sigma_{C,FEM}$, (i.e., of the limit values of the elastic stress peaks in the FEM calculations), the following relation can be used:

$$n = \frac{K_t}{K_f} = \frac{K_t \cdot \sigma_C^*}{\sigma_C} = \frac{\sigma_{C,FEM}}{\sigma_C}, \text{ so that } \sigma_{C,FEM} = n_G \cdot \sigma_C,$$

where σ_C is the material fatigue limit during a homogeneous uniaxial tensile stress.

Analogously to the K_f factor introduced in the region of the permanent fatigue strength, it is possible to define the notch factor, $K_{f,N} = \frac{\sigma_A}{\sigma_A^*}$, in the region of the limited life from the fatigue test results or, as the case may be, the fatigue ratio by the relation $n_{G,N} = \frac{K_t}{K_{f,N}}$. It is then possible to obtain the fatigue curve of virtual stress values at the notch root, $\sigma_{FEM} = \frac{K_t}{K_{f,N}} \cdot \sigma_C = n_{G,N} \cdot \sigma_C$, which must lie above the smooth sample curve (see Fig. 2). In practical calculations, we can also use an opposite procedure. During the damage calculation, we use the fatigue curve of a smooth sample and correct the local stress amplitudes by calculating the quantity

$$\sigma_{cor} = \sigma_{FEM} \cdot \frac{K_{f,N}}{K_t}. \tag{8}$$

This procedure is also illustrated in Fig. 2.

Table 1

Author	Fatigue ratio n	Note	Equation
Neuber	$n_\rho = 1 + \frac{A}{\rho} \cdot \left(1 - \frac{1}{K_f}\right)$	where $A = f(R_m)$ is the Neuber factor, see, e.g., [2]	(2)
Peterson	$n_\rho = 1 + \sqrt{\frac{a}{\rho}} \cdot \left(1 - \frac{1}{K_f}\right)$	where a is the critical surface layer depth, see, e.g., [2]	(3)
Heywood	$n_\rho = 1 + 2\sqrt{\frac{a'}{\rho}} \cdot \left(1 - \frac{1}{K_f}\right)$	empirical factor a' see, e.g.,. [2]	(3)
Siebel, Stiller	$n_G = 1 + \sqrt{c \cdot G}$	parameter c see, e.g., [2]	(4)
Bäumel Seeger [3]	$n_G = 1 + \sqrt{G} \cdot 10^{-\left(\frac{R_e}{810} + 0{,}35\right)}$	where R_e is the yield strength	(5)
Eichelseder [4]	$n_G = 1 + \left(\frac{\sigma_{C,b}}{\sigma_C} - 1\right) \cdot \left(\frac{G}{2/d}\right)^k$	where $\sigma_{C,b}$ and σ_C are the bending and tensile fatigue limits, d is the diameter of the bending sample	(6)
Volejnik, Kogaev [5]	$n_G = 1 + \left(\frac{1}{v_\infty} - 1\right) \cdot \left(\frac{L/G}{L_0/G_0}\right)^\mu$	here v_∞ is the magnitude factor for the homogeneous strength, μ is an exponent	(7)

5. Synthetic S-N curves

Fig. 2 indicates the analogy between the LESA approach and the NSA approach. While the fatigue curve is corrected in the downward direction in the nominal approach with respect to the notches, and the fatigue damage is determined from the nominal stress amplitude, the local approach uses the corrected stress peak at the notches and the

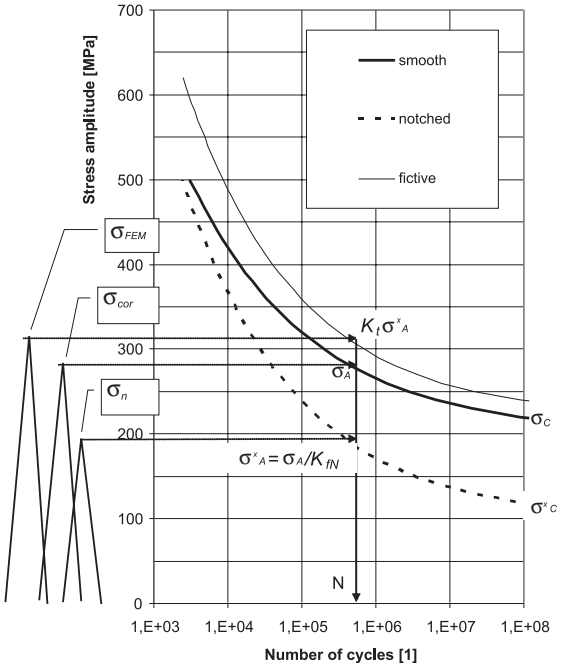

Fig. 2

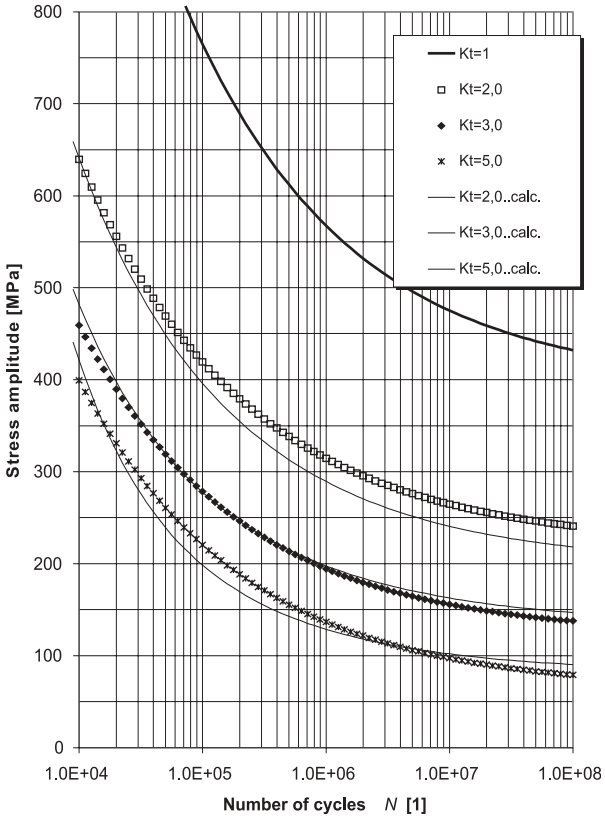

Fig. 3

initial fatigue curve of the sample without notches. Let us mention, however, that all the effects of the surface quality of the actual machine part should be projected into the curve and, as the case may be, its further technological modifications. The magnitude factor is taken into account in the above-indicated similarity criterion of the stress gradient effect and exposed volume.

The author of this paper proposed a modification of the Heywood expression (see [6]) for the description of the notch effect in the region of the limited life, i.e., for the expression of the $K_{f,N}$ coefficient, $K_{f,N} = 1 + (1 - K_t) \cdot \mu(N)$, (9)

in which the dependence on the relative stress gradient, G, was expressed in the following form: $n_G = \frac{K_t}{K_f} = 1 + \sqrt{G} \cdot 10^{-(K1)}$ and the time functions as $\mu(N) = \frac{(\log N)^E}{B + (\log N)^E}$ with the parameters $E = 4 \cdot G^{K2}$ and $B = \left[\frac{1}{(1+G)^{K3}} \cdot \frac{K4}{R_m}\right]^2$.

The curves of ASTM 300M steel according to MIL-HDBK catalogue [7] are taken for an example here. The mathematical description of fatigue curves and of their parameters for smooth and specific notched specimens with a variable shape factor K_t are presented in Tab. 2.

Fig. 3 depicts the comparison of commented catalogue curves and the derived ones. The goal is to obtain the smallest possible difference in the area of middle and higher notch factor and in the range of cycles between 10^4 and 10^7 cycles. It can be clearly seen that the coincidence is satisfactory – especially towards the original sources, where the significant scatter of experimental points is clear, and to the fact, that the punctuality of result approximation by a mean curve is affected with certain error. The parameters of a studied approximation are given in the last column of Tab. 2. To describe the effect of number of cycles (i.e. the $\mu(N)$ factor) on the size of different notch coefficient K_f, the $K_{f,N}$ dependencies were depicted (Fig. 4). It can be traced that the notch factor progressively decreases with higher concentrations on the specimen for lower numbers of cycles. A bunch of the so-called synthetic fatigue curves can be generated for any general stress gradient and shape factor; these curves can represent the required areas of the structure in the NSA approach. The example of these curves is indicated in Fig. 5.

The set of these equations can also be used for correcting the elastic stress peaks according to relation (8) in the LESA approach.

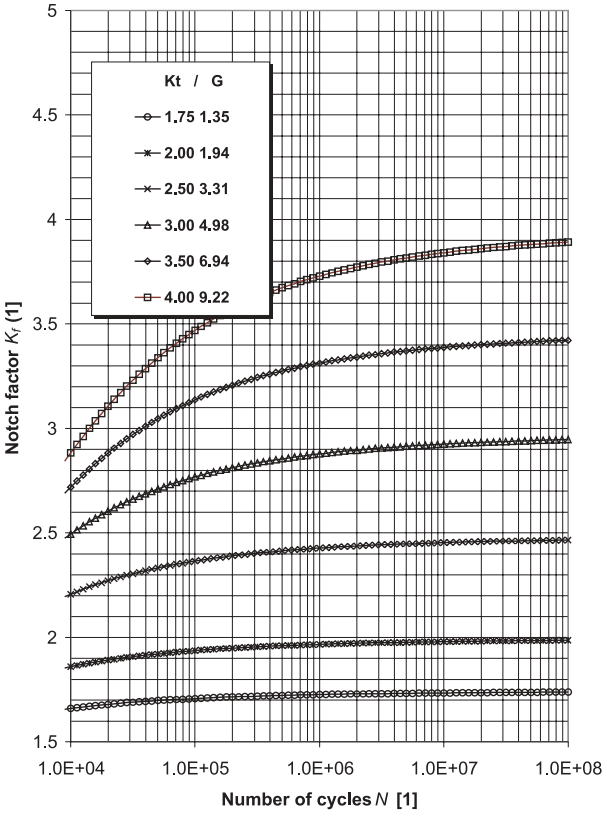

Fig. 4

Table 2

	Shape factor K_t	Fatigue curve description $N \cdot (\sigma_{\max,eg} - \sigma_C)^w = C$	Exponent p $\sigma_{\max,eg} = \sigma_{\max}(1-R)^p$	Synthetic curve parameters K_i
300M steel	1.0	$logN = 10{,}58 - 3{,}02 \cdot \log(\sigma_{eq} - 75{,}0)$	0,39	$K1 = 2.409$
	2.0	$logN = 12{,}87 - 5{,}08 \cdot \log(\sigma_{eq} - 55{,}0)$	0,36	$K2 = 0.1$
	3.0	$logN = 9{,}52 - 3{,}00 \cdot \log(\sigma_{eq} - 25{,}0)$	0,50	$K3 = -0.989$
	5.0	$logN = 9{,}61 - 3{,}04 \cdot \log(\sigma_{eq} - 15{,}0)$	0,52	$K4 = 6100$
	N ... lifetime in number of cycles $\sigma_{max,eq}$ *upper stress of equivalent cycle [ksi]* σ_{max} *... upper stress of loading cycle [ksi]* σ_c *... fatigue limit [ksi]*		*p ... exponent for equivalent stress* *C, w ... fatigue curve parameters* *R ... coefficient of cycle asymmetry* $\sigma_{min} / \sigma_{max}$ ***Remark:*** *1 ksi = 6.894 MPa*	

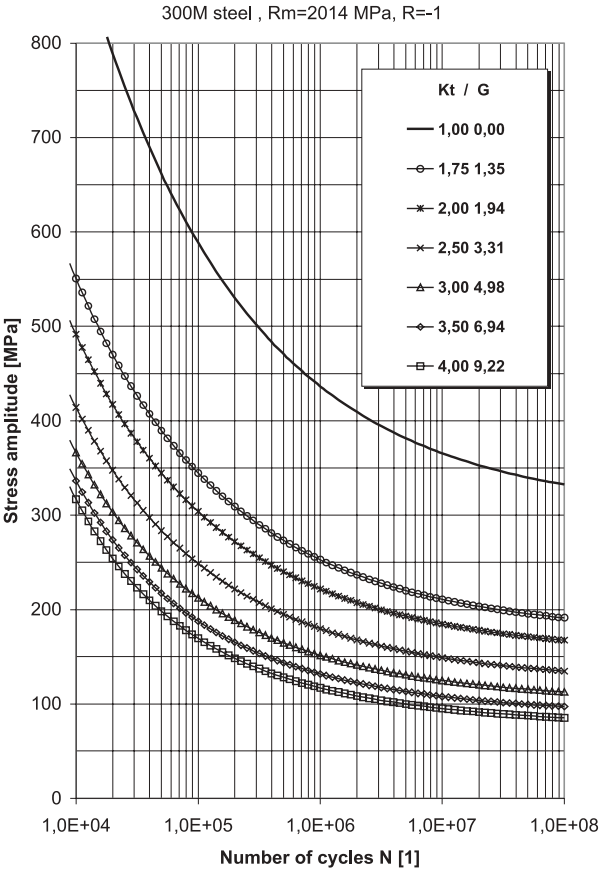

Fig. 5

6. Correction for the effect of the mean stress

For the purposes of the calculation of the fatigue damage, the biparametric description of the loading history stored in the rain flow matrix should be transformed to the equivalent stress cycle. This means that for a general stress cycle of amplitude σ_a and mean value σ_m, described also by the asymmetry factor $R = \dfrac{\sigma_{min}}{\sigma_{max}}$, we assign a cycle with the same damaging effect. Let us mention that the correction is carried out only for the region of tensile mean stress values. Usually, the equivalent symmetrically alternating cycle is assigned (i.e., for $\sigma_m = 0$ or $R = -1$) and denoted as $\sigma_{a,eq}$, or the repeated cyclic load (i.e., for $\sigma_m = \sigma_a$ or $R = 0$) is assigned and denoted as $\sigma_{max,eq}$. For the determination of the equivalent cycle, it is possible to use for example the relations for the approximation of the Haigh diagram. We obtain $\sigma_{a,eq} = \sigma_a \dfrac{1}{1 - \left(\dfrac{\sigma_m}{\sigma_f}\right)^s}$, where σ_f represents the static fracture strength and the s exponent describes both the linear form of the limit curve (for $s = 1$), and for example the parabolic form (for $s = 2$). The behaviour of the actual machine parts with stress raisers of the geometrical and technological type (for example, parts with welds) revealed that the initial significant reduction of the fatigue ultimate strength decreases with increasing prestressing and that the limit curve has a nonlinear form. In Ref. [7], the limit curve of the Haigh diagram is indicated in the form of $\sigma_a^p \cdot (\sigma_a + \sigma_m)^{1-p}$, from which the equivalent amplitude can be expressed as

$$\sigma_{a,eq} = \sigma_a^p \cdot (\sigma_a + \sigma_m)^{1-p} = \sigma_a \left(\frac{2}{1-R}\right)^{1-p} \qquad (10)$$

For metallic materials (carbon steels, aluminium alloys), the value of the p exponent is close to $p = 0.5$, so that relation (10) becomes

$$\sigma_{a,eq} = \sqrt{\sigma_a \cdot (\sigma_a + \sigma_m)} = \sqrt{2} \cdot \sigma_a - \frac{1}{\sqrt{1-R}} \qquad (11)$$

The value of the repeated cyclic load can be expressed from Eq.(10) analogically as

$$\sigma_{max,eq} = \sigma_{max}(1-R)^p , \qquad (12)$$

which for $p = 0.5$ takes the form

$$\sigma_{max,eq} = \sigma_{max}\sqrt{(1-R)} = \sqrt{2\sigma_a \cdot (\sigma_a + \sigma_m)} . \qquad (13)$$

Relation (13) is known for example in the aerospace engineering as the Oding correction. The correction according to Eq.(11) can also be considered as a certain analogy; this correction forms the basis for the calculation of the damage parameter, P_{SWT}, according to Smith, Watson and Topper, as already mentioned in the introductory part. It holds for this parameter that $P_{SWT} = \sqrt{\sigma_a \cdot (\sigma_a + \sigma_m)} = \sqrt{E \cdot \varepsilon \cdot (\sigma_a + \sigma_m)}$; in the low-cycle fatigue region, the local elastic and plastic stress and the deformation amplitudes are considered in this expression.

7. Scheme of the LESA application and conclusion

The above-discussed aspects of the fatigue damage can be summarized in the following proposal of the procedures for the prediction of the fatigue life of actual machine parts of structures subject to FEM calculations in the elastic stress region. The input quantities of the calculation are:

- The results of the stress state determined using FEM for the individual states of the effect of operational forces (usually for a “unit” load).
- The loading history corresponding to a given unit of the operational time obtained by a linear combination of individual loading states and processed by the rain flow method.
- The fatigue curve of the material used that is modified with respect to the surface layer quality.

According to the scheme indicated in Fig. 6, a relation can be shown to exist between the following steps of a further procedure:

- Correction of the elastic stress peaks according to Eq. (8)
- Correction for the mean stress of the loading cycle.
- Application of the rules for damage accumulation, including the correction of the results of the calculation on the basis of

the carried out fatigue tests during the simulation of the operational loading spectra.

The result is interpreted as the fatigue life until the initiation of a fatigue crack at a local point of the structure. During the computer processing of each point of the surface of a machine part, a map of fatigue damage can be displayed. This makes it possible to find quickly the critical points visually and the lengths of the predicted fatigue life by their mutual comparison, analogously as during the assessment of the stress state during a static analysis by means of FEM. Some examples of applications were already published; see e.g. Refs. [8] and [9].

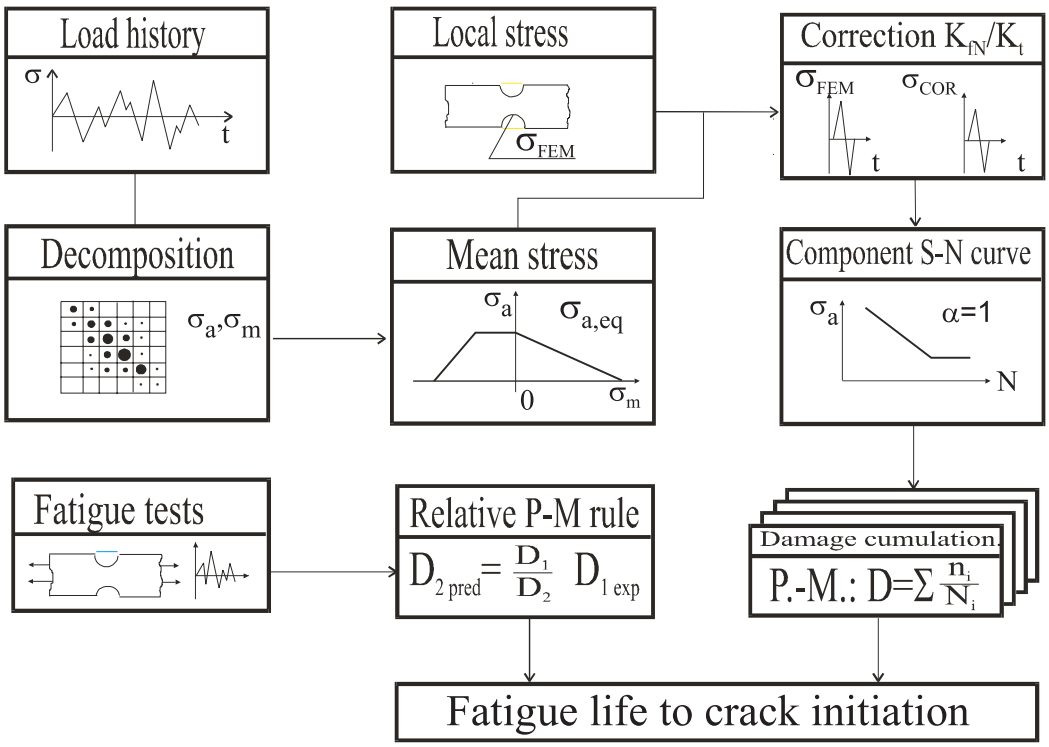

Fig. 6

References

[1] RŮŽIČKA, M.: *Life Prediction of Machine Parts Using the Local Approach.* (in Czech). In: Dynamic of Machines '94. Prague, Institute of Thermomechanics AS CR. 1994. pp. 77-80.
[2] RŮŽIČKA, M., HANKE, M., ROST, M.: *Dynamic Strength and Service Life.* (in Czech), lecture notes CTU Prague, 1992.
[3] BÄUMEL, A., SEEGER, T.: *Material Data for Cyclic Loading - Suppl. 1.* Materials Science Monographs 61, Elsevier Sc. Publisher, Amsterdam 1990.
[4] EICHELSEDER, W., LEITNER, H.: *Influence of Stress Gradient on S/N-Curve.* In: New trends in fatigue and fracture, Metz April, 2002.
[5] VOLEJNIK, N, V.: *Carrying Capacity of Machine Parts.* (in Russian). Scientific Idea Publ., Moscow 1985.
[6] HEYWOOD, R. B.: *Design Against Fatigue,* Pergamon Press, 1965.
[7] Military Standardization Handbook: *Metallic materials and elements for aerospace vehicle structure.* MIL-HDBK-5D, 1987.
[8] RŮŽIČKA, M.: *Service Life Prediction of the Airplane Engine Bed.* (in Czech). In: Dynamic of Machines 99, Institute of Thermomechanics CAS, Prague 1999, pp. 217-224. ISBN 80-85918-48-X.
[9] RŮŽIČKA, M., PAPUGA, J., KUBA, P.: *Integration of Methods of the Experimental Stress Analysis in Design Mountainbike Components.* In: 17th Danubia Adria Symphosium – Extended Summariers. Department of Mechanics, CTU Prague 2000, p. 293-296. ISBN 80-01-02234-X.

kamUNikácie
COMMUNICATIONS

Marián Činčala – Ludvík Kunz *

HIGH-CYCLE FATIGUE BEHAVIOUR OF 14 109 BEARING STEEL

Fatigue lifetime of 14 109 bearing steel in a high-cycle region in tension-compression has been studied experimentally. The aim was to determine the S−N curve including fatigue limit, to perform fractographic observation and to analyze crack initiation sites, to discuss the large scatter of lifetime data, which is inherent to high strength steels, and to check the empirical $\sqrt{area}$ method to predict fatigue limit for this type of steel.

1. Introduction

Bearings are important machine parts, which have to sustain an extremely high number of loading cycles during their lifetime. Severe material and technological requirements are posed on the manufacturing of particular bearing parts. Structural steel 14 109, which has frequently been used for bearing bodies, balls and cylindrical roller bearings, fulfills these requirements. This steel is an equivalent of the European 100Cr steel, US E52100 through-hardening steel or Japanese SUJ2 and SUJ4 steels. The characteristic feature is higher content of C and Cr, which is an important prerequisite for superior mechanical properties. In spite of the fact that this steel belongs to the group of common structural steels, it still attracts research attention from the point of view of the relation among microstructure, mechanical properties and machining technology [1].

Extremely high fatigue lifetime is a crucial requirement for all types of bearing steels. Fatigue properties of high strength steels generally strongly depend on the surface state and on structural defects [2-3]. High quality clean steels, free from nonmetallic inclusions or other stress raisers are the primary requirement to achieve extended fatigue life. This holds above all in the high-cycle and giga-cycle fatigue regions. Defects on the surface – small notches, scratches, impressions and roughness – play an important role in the pitting process. However, suitable technological and production processes can eliminate them successfully. High quality finished surfaces, application of suitable lubricants diminishing friction and heat generation at contact areas significantly suppress this problem. On the other hand, details of microstructure and micropurity remain important phenomena which determine the fatigue crack initiation and hence the fatigue lifetime. Irregularly distributed small carbides and non-metallic inclusions are the result of desoxidation process and of heat treatment. They often represent severe stress raisers. Fatigue cracks initiate predominantly in their vicinity. Whereas in the case of surface initiation the crack location and propagation can be monitored and described during the cyclic loading, in the case of internal initiation and crack propagation some open questions remain.

Fatigue lifetime data in high-cycle and giga-cycle region have been shown to exhibit a "two-stage" or "stepwise" $S-N$ curve, eg. [4-5]. Japanese researchers have performed the majority of these observations on bearing steels [6-10] using rotating bending fatigue machines. The main reason for the two-stage $S-N$ curve seems to be the transition from the surface to internal crack initiation in the very-high-cycle region. The discontinuity on $S-N$ curves and the change of the crack initiation from the surface to the interior has been usually reported in the interval between 10^6 to 10^7 cycles. Recently Marines et al. [11] have compared the S-N curves of bearing steel NF 1006C at frequencies of 35 and 30 kHz in tension-compression and in rotating bending. They indicate that the two-stage S-N curve is connected with the rotating bending; if the tension-compression loading is used, a continuously decreasing lifetime with decreasing stress amplitude is observed up to the giga-cycle region. Further, the fatigue limit of bearing steels defined between 10^6 to 10^7 cycles cannot guarantee a safe design.

The aim of this work was to experimentally determine the fatigue lifetime of bearing steel 14 109 in tension-compression and to analyze the crack initiation in the range of 10^6 to 10^7 cycles.

2. Material and experiments

Hypereutectic steel 14 109 with the chemical composition as given in Tab.1 has been used. The composition corresponds to that of E52100 and SUJ 2 steels.

Chemical composition of 14 109 steel (wt.%). Tab. 1.

C	Mn	Si	Cr	Ni	Cu	Ni+Cu	P	S
1.0	0.34	0.28	1.48	0.1	0.12	0.22	0.01	0.01

Button-end specimens for fatigue tests, Fig. 1, were prepared by cutting operation. The minimum gauge length diameter was machined with working allowance of 0.8 mm. Heat treatment consisted of austenitization at 1113 K for 20 min. followed by rapid

* **Marián Činčala[1], Ludvík Kunz[2]**
[1] Žilinská univerzita v Žiline, Veľký diel, 010 26 Žilina, Slovenská republika
[2] Ústav fyziky materiálů AV ČR, Žižkova 22, 616 62 Brno, Česká republika

quenching into oil (JS4). The resulting martensitic microstructure was annealed for stress relieving at 443 K with holding time of 90 min followed by air-cooling. The resulting microstructure consists of tempered martensite with regularly distributed carbides and residual austenite content of 6.35 ± 0.94 wt. % (determined by difractometric analysis). The microstructure of heat-treated steel is shown in Fig.2. The hardness measured on the specimen cross-section varies between 650 ÷ 713 HV and is well compared with the hardness reported in [11]. The gauge length with working allowance of 0.8 mm of heat-treated specimens was finely ground to the final diameter of 3 mm with the aim of removing the notch influence of the surface after cutting operation and of removing the decarburized layer. The final operation consisted of fine grinding by means of metallographic emery papers on a turn bench.

Fatigue tests were accomplished on resonant fatigue machine Amsler in controlled load. The cycling was characterized by sine load wave with frequency 190 Hz. The stress ratio *R* was equal to −1. Experiments were performed at room temperature in the ambient air atmosphere. In the stress amplitude interval used, no heating of specimens was observed.

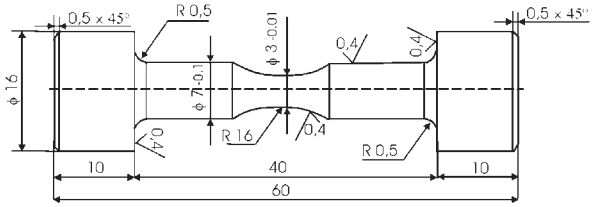

Fig. 1. Specimen for experimental determination of S–N curves.

3. Results

Experimentally determined lifetime of specimens loaded in tension-compression is shown in Fig. 3. The experimental data exhibit a considerable scatter. The highest stress amplitude at which the run-out specimen (on the basis of 10^7 cycles) was found is 840 MPa.

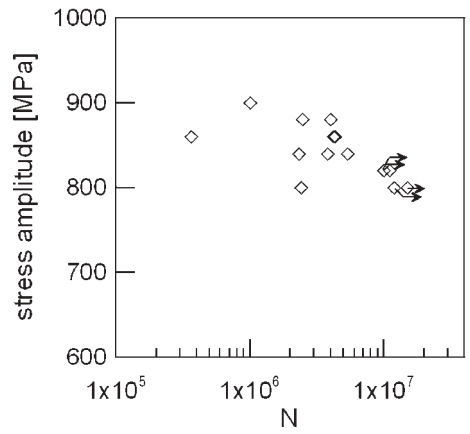

Fig. 3. S–N curve of 14 109 bearing steel.

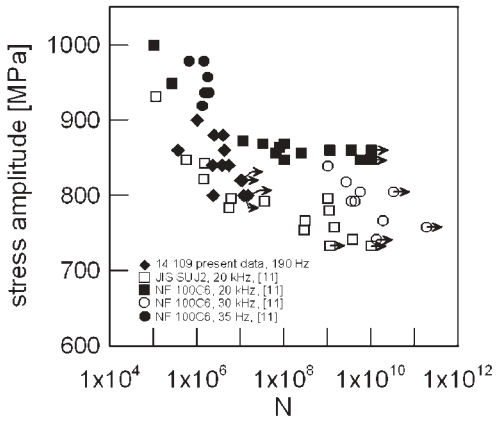

Fig. 6. Comparison of present results with literature data [11]

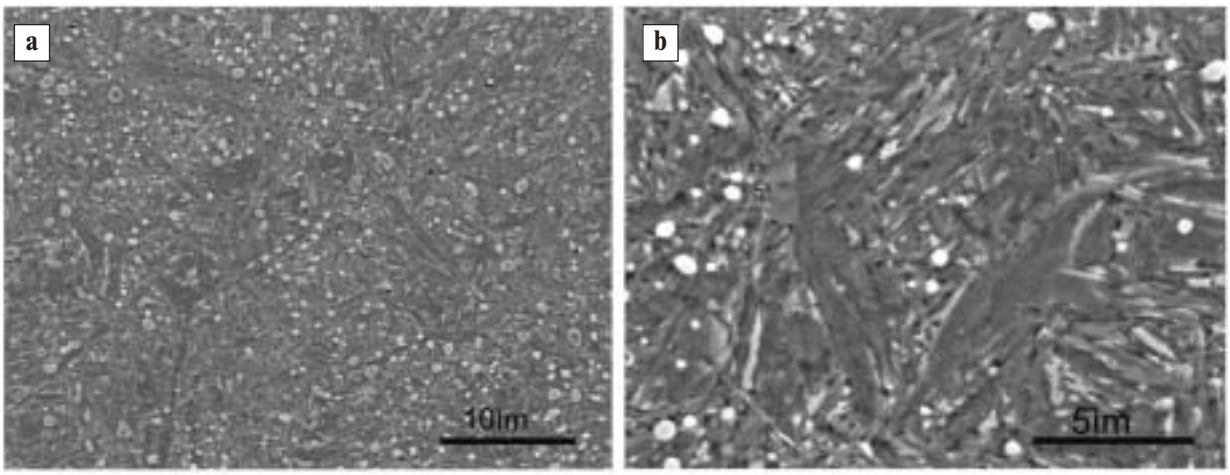

Fig. 2. Microstructure of 14 109 steel. Picric acid etching.

Fractographic analysis revealed that all specimens tested in a high-cycle region failed by fatigue fracture, originating on internal defects of various types. An example of a large aluminium oxide inclusion can bee seen in Fig. 4. The inclusion contains nearly 42 % of Al, 53 % O (determined by X-ray difractometric analysis, wt. %) and the rest is made of Fe, Cr and C. In Fig. 5 an example of a small TiN inclusion is shown. The corresponding composition is 66 % Ti, 19 % N, 9% Cr, and the rest is Fe, V and Zr. The fracture surfaces exhibit typical fish eye appearance with an inclusion at the centre.

4. Discussion

A large scatter of experimental lifetime data in a high-cycle region is a typical feature of high strength bearing steels. This holds not only for a particular batch but it is even more pronounced when experimental results on steels of a similar chemical composition and heat treatment but coming from different steel-makers are compared. The $S-N$ curves cannot be exactly defined. There is no good correlation between the stress amplitude and the number of cycles to fracture, Fig. 3. Results obtained in this work are shown along with high-cycle fatigue data of JIS SUJ2 and NF 106C steel, published in [11] in Fig. 6. It can be concluded that high-cycle lifetime of 14 109 steel fits well into the broad range of results obtained in bearing steels.

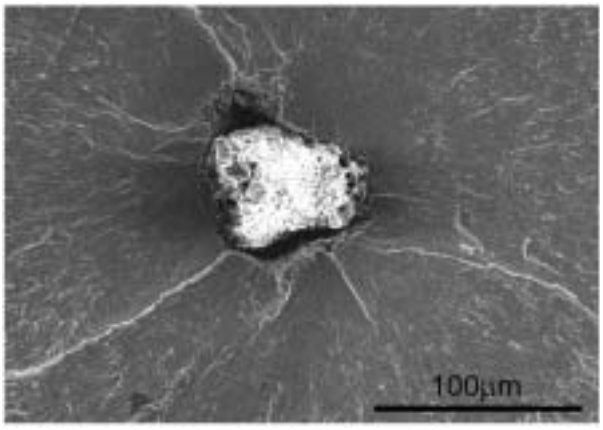

Fig. 4. Large aluminium oxide inclusion at the fatigue crack origin.

In some cases the $S-N$ curves have been interpreted as "two-stage" curves, having a horizontal step in the vicinity of a conventional fatigue limit at an interval of between 10^6 to 10^7 cycles. Experimental results shown in Fig. 3 do not exhibit any sign of a horizontal step. In the frame of the large scatter there seems to be rather a continuous decrease of lifetime following the decrease of stress amplitude. This finding supports suggestion proposed in [6], [11], namely that the $S-N$ curve determined on rotating bending specimens can be influenced by the small size of an extremely loaded volume of material related to large stress gradients in such a way that the $S-N$ curve manifests itself as a step curve.

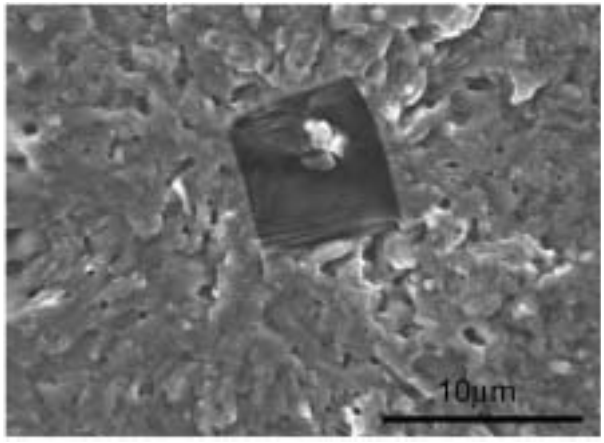

Fig. 5. TiN inclusion in the middle of a fish eye.

Fatigue fracture of bearing steels originate in high-cycle fatigue, mostly at non-metallic inclusions like Al_2O_3, CaO or SiO_2. This is in full agreement with fractographic observations, Fig. 4 and 5. All fatigue cracks were initiated at internal inclusions. The influence of small defects or inclusions on fatigue limit can be estimated by an empirical $\sqrt{area}$ method, proposed by Murakami [12]. The $\sqrt{area}$ parameter is defined as the square root of the projected area of a defect into the plane perpendicular to the loading direction. The fatigue limit for symmetrical loading σ_w of a specimen with an internal defect that can be characterized by the geometrical parameter $\sqrt{area}$ can be predicted according to the formula

$$\sigma_w = 1.56(HV + 120)(\sqrt{area})^{-1/6}. \qquad (1)$$

HV stands for Vicker's hardness, $\sqrt{area}$ is in μm, and fatigue limit is in MPa. Fractographic observation made it possible to detect and evaluate dimensions of inclusions located in the origin of fatigue fracture almost for all tested specimens. The inclusion dimensions represented $\sqrt{area}$ by parameter, the number of cycles to fracture N_f and the fatigue limit σ_w, as predicted according to formula (1) taking into account hardness value $HV = 650$, are given in Tab. 2.

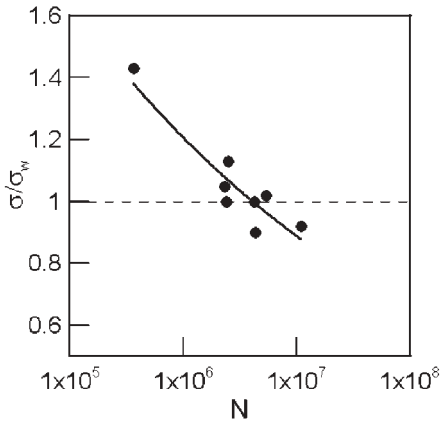

Fig. 7. Modified S–N curve.

Fatigue lifetime, inclusion size at initiation site, and fatigue limit as predicted by $\sqrt{area}$ of method. Tab. 2.

σ_a [MPa]	N_f [cycle]	$\sqrt{area}$ μm	σ_w [MPa]	σ_c/σ_w
900	1.00×10^6	—	—	—
880	2.48×10^6	13.5	778	1.13
880	4.00×10^6	—	—	—
860	3.64×10^5	63.6	601	1.43
860	4.34×10^6	4	953	0.90
860	4.23×10^6	7.4	860	1.00
840	5.39×10^6	9.7	823	1.02
840	2.33×10^6	11.5	800	1.05
820	1.11×10^7	6	892	0.92
800	2.41×10^6	11.4	801	1.00

The highest stress amplitude at which the run-out specimens (on the conventional basis of 10^7 cycles) were observed is, according to Fig.3, $\sigma_c = 840$ MPa. Fig. 7 shows the modified $S-N$ curve according to Murakami [4]. It can be seen, that the values of σ/σ_w ratio can decrease below 1. This supports the opinion that the conventional number of cycles of the order of 10^7 is insufficient for reliable determination of the fatigue limit of bearing steels [11], where the mechanism of fatigue initiation is related to the role of internal inclusions.

5. Conclusions

The $S-N$ curve of 14 109 bearing steel determined in tension-compression does not exhibit a two-stage form. All fatigue cracks in the high-cycle region were initiated at internal inclusions; a considerable scatter of experimental data is related to this fact. Determination of fatigue limit on the basis of 10^7 is insufficient for this steel; a higher number of cycles has to be used.

Acknowledgements

This work was supported by The Centre for Transportation Research (CETRA, Žilina), the project of bilateral Czech-Slovak co-operation Nr. 36 and the grant No. 1/1077/04 of the Scientific Grant Agency of Ministry of Education and Slovak Academy of Sciences, Slovak Republic.

References

[1] BENGA, G. C., ABRAO, A. M.: *Turning of hardened 100Cr6 bearing steel with ceramic and PCBN cutting tools.* Journal of Mat. Processing Technol., 143-144 (2003) 237-241.
[2] MOYER, C.: *Fatigue life prediction of bearings. In: Fatigue and Fracture,* ASM Handbook, Vol.19. ASM Int. Materials Park, OH, 1996, p.355-368.
[3] JECH, J.: *Bearing steels and its heat treatment (in Czech)*, SNTL Praha 1968.
[4] MURAKAMI, Y., NOMOTO, T., UEDA, T: *Factors influencing the mechanism of superlong fatigue failure in steels.* Fatigue Fract Engng Mater Struct 22 (1999) 581-590.
[5] MUGHRABI, H.: *On the life-controlling microstructural fatigue mechanisms in ductile metals and alloys in the gigacycle region.* Fatigue Fract Engng Mater Struct. 22 (1999) 633-641.
[6] MURAKAMI, Y., YOKOYAMA, N. N., NAGATA, J.: *Mechanism of fatigue failure in ultralong life regime.* Fatigue Fract Engng Mater Struct 25 (2002) 735-746.
[7] SAKAI, T., SATO, Y., OGUMA, N.: *Characteristic S-N properties of high-carbon-chromium-bearing steel under axial loading in long-life fatigue.* Fatigue Fract Engng Mater Struct 25 (2002) 765-773.
[8] TANAKA, K., AKINIVA, Y.: *Fatigue crack propagation behaviour from S-N data in very high cycle region.* Fatigue Fract Engng Mater Struct 25 (2002) 813-822.
[9] SHIOZAWA, K., LU, L.: *Very-high cycle fatigue behaviour of shot-peened high-chromium bearing steel.* Fatiuge Fract Engng Mater Struct 25 (2002) 775-784.
[10] WANG, Q. Y., BATHIAS, C., KAWAGOISHI, N., CHEN, Q.: *Effect of inclusion on subsurface crack initiation and gigacycle fatigue strength.* Int. J. Fatigue 24 (2002) 1269-1274.
[11] MARINES, I., DOMINGUEZ, G., BAUDRY, G., VITTORI, J.-F., RATHERY, S., DOUCET, J.-P., BATHAIS, C.: *Ultrasonic fatigue tests on bearing steel AISI-SAE 52100 at frequency of 20 and 30 kHz.* Int. J. Fatigue 25 (2003) 1037-1046.
[12] MURAKAMI, Y., ENDO, M.: *Effects of defects, inclusions and inhomogeneities on fatigue strength.* Int. J. Fatigue 16 (1994) 163 - 182.

kamUNikácie
COMMUNICATIONS

Pavel Lukáč – Zuzanka Trojanová *

MECHANICAL PROPERTIES OF AZ91 MAGNESIUM ALLOYS

Commercial magnesium alloys AZ91 were reinforced with Al_2O_3 short fibres. The composites were prepared by different fabrication routs (powder metallurgy technique, squeeze casting and casting followed by extrusion). Some specimens of the AZ91 alloy were prepared using equal channel angular pressing. The values of the yield stress and the maximum stress of specimens deformed at temperatures between 20 and 300 °C were determined. The test temperature strongly influences the mechanical properties of the AZ91 alloy and its composites.

1. Introduction

Engineering importance of magnesium alloys has grown recently. The automotive industry shows a growing interest in magnesium alloys because of their low density and high damping. Magnesium alloys as a structural material in cars may reduce fuel consumption and exhaust emissions. The applications fields for magnesium alloys are also aviation and communication industries. Magnesium alloys are considered as promising light structural materials, even if they have poor ductility. If deformed at room temperature, they exhibit a tensile elongation of only a few percent. Among the most commercial magnesium alloys used, AZ91 alloy (Mg-9Al-1Zn) dominates. The mechanical properties of the commercial magnesium alloy AZ91 depend strongly on temperature. The specific strength of AZ91 at room temperature is high but it remains rather low at temperature above about 120 °C. It is well known that it is a close relationship between microstructure and the mechanical properties. In order to improve the mechanical properties it is important to understand the deformation mechanisms of yielding and work hardening. Solid solution hardening, precipitation and/or dispersion strengthening influence the yield stress. The yield stress increases also with decreasing grain size. The grain size dependence of the yield stress and tensile strength can be expressed by the Hall – Petch relation. Magnesium alloys reinforced with short ceramic fibres or particles exhibit significantly higher mechanical properties than conventional alloys. The microstructure of alloys and metal matrix composites is influenced by the fabrication routs. The mechanical properties and the deformation behaviour of Mg alloys as well as composites are strongly influenced by temperature and strain rate. The aim of this paper is to provide information on the mechanical properties of AZ91 alloys and AZ91+Saffil composites deformed at various temperatures. The results will be discussed.

2. Experiments

The investigated materials were AZ91 (9Al, 0.7Zn, 0.2Mn in wt.%) alloy and AZ91 reinforced with δ-Al_2O_3 short fibres (Saffil®) with a mean diameter of 3 μm and a mean length about of 87 μm. Alloys were prepared by different fabrication routs. Composites were prepared by squeeze casting. The preforms, consisting of Al_2O_3 short fibres with a planar isotropic fibre distribution, were infiltrated using two-stage application of the pressure. Tensile specimens of the cylinder form with a gauge length of 25 mm (with a diameter of 4 mm) and compression specimens with dimensions $5 \times 5 \times 10$ mm^3 were annealed according to T6 treatment (413 °C/18h, then 168 °C/8h). Tensile and compression tests were carried out using an Instron machine at temperatures between 22 and 300 °C at a strain rate of 8.3×10^{-5} s^{-1}. Some tensile specimens with dimensions of $1 \times 2 \times 10$ mm^3 were machined from the rods produced by equal channel angular pressing (ECAP).

3. Experimental results and discussion

The value of the yield stress (YS = 0.2 % proof stress), tensile strength (UTS) and the % elongation to fracture (A) of AZ91 alloys and composites produced by various fabrication routs are given in Table 1 (for specimens deformed at room temperature and 200 °C). Above 100 °C the yield stress and tensile strength of AZ91 alloy decrease very rapidly with increasing temperature. The elongation to fracture increases with increasing temperature. Aune and Westengen [1] have reported that the elongation to fracture is 7 % at room temperature and it reaches 13 % and 23 % at 100 °C and at 150 °C, respectively. Table 1 shows that the values of the yield stress of AZ91 alloys and AZ91/Al_2O_3 composites [2, 3] are influenced by the fabrication methods. Composites (AZ91 + 15 vol. % Saffil) and also matrix alloys prepared by powder metallurgy (PM) exhibit a higher tensile strength and a higher yield stress than those materials prepared by squeeze casting (Sc) and casting followed by extrusion (Sce). The reason for the increase in the mechanical properties is an increase in the dislocation density induced by the powder metallurgy technique or extrusion process. The increased dislocation density causes a decrease in the dislocation mobility. The free path of dislocation is lower. This may induce an enhanced ductility of AZ91 materials prepared by squeeze casting. However, it should be noted that squeeze casting is more suitable for preparation of short fibre reinforced composites because of less damage of the fibres in com-

* **Pavel Lukáč, Zuzanka Trojanová**
Department of Metal Physics, Charles University, Ke Karlovu, 121 16 Praha 2, Czech Republic,
E-mail: lukac@met.mff.cuni.cz; ztrojan@met.mff.cuni.cz

parison to the PM technique. It is important to note that while the yield stress and tensile strength of composites prepared by squeeze casting decrease gradually with increasing temperature, the same tensile properties of composites prepared by PM decrease strongly with increasing temperature. The addition of the fibres to the matrix increases both the yield stress and tensile strength.

Tensile properties of unreinforced and reinforced AZ91 alloy at room temperature — Tab. 1

	YS/MPa	UTS/MPa	UTS/MPa at 200 °C	A/%
AZ91 (PM)	270	330	120	4.0
AZ91 + 15 (PM)	395	420	123	0.7
AZ91 (Sc)	120	230	120	8.5
AZ91 (Sce)	240	325	132	4.0
AZ91 + 20 (Sc)	245	320	227	1.8
AZ91 + 20 (Sce)	282	290	147	0.7

The deformation behaviour (see the differences in the values between tensile strength and yield stress) is influenced by the thermal stresses. Cooling of a composite from a higher temperature of processing to room temperature may generate thermal residual stresses due to the difference in the coefficients of thermal expansion (CTE) of the matrix and reinforcement. If the applied stress is zero, then the thermal stress near the interface between reinforcement and matrix is given by

$$\sigma_{TS} = E_f E_m f \Delta\alpha \Delta T / [E_f f + (E_m(1 - f)] \quad (1)$$

where f is the volume fraction of fibres, $\Delta\alpha$ is the CTEs difference, ΔT is the temperature range, E_f and E_m are the elastic modulus of the fibres and the matrix, respectively. If thermal stresses become larger than a critical stress, stress relaxation occurs and new dislocations are generated at the interface (in the matrix near the fibres). The density of newly created dislocations produced by the thermal stresses in the composite reinforced with fibres can be calculated as [4, 5]

$$\Delta\rho = Bf\Delta\alpha\Delta T/(1 - f)br \quad (2)$$

where B is a constant that depends on the geometry of the fibres, r is their radius and b is the magnitude of the Burgers vector. The increase in the flow stress corresponding to the increase in the dislocation density is given by

$$\Delta\sigma = \mathrm{AGb}(\Delta\rho)^{1/2} \quad (3)$$

where A is a constant and G is the shear modulus of the matrix. The increase in the flow stress of the matrix in the composite over unreinforced metal is proportional to square root of $\Delta\alpha\Delta T$, if the newly generated dislocations due to CTE mismatch are dominant. In any cases, a dislocation increment due to CTE mismatch and cooling is one of strengthening mechanisms in the composites. The dislocation density near the interface is significantly higher than elsewhere in the matrix. Plastic zones containing tangled dislocations may be formed around the fibres. The dislocation movement is determined by the required stress that depends on temperature, the internal stress in the matrix, the distribution and kind of obstacles, and the crystallographic orientation of the grains to the fibres.

The influence of the test temperature on the stress strain curves of AZ91 alloy for a compression test is shown in Fig. 1. It can be seen that the flow stress and the strain hardening decrease significantly with increasing temperature. At temperatures above about 250 °C strain softening is observed from the very beginning of deformation. The temperature dependence of the yield stress

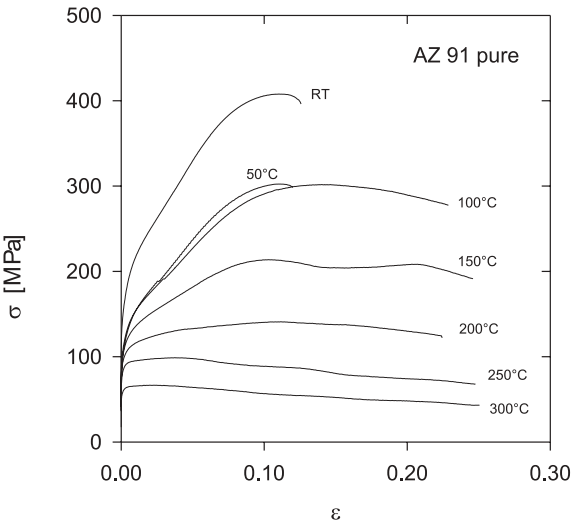

Fig. 1 The true stress-true strain curves obtained in compression

σ_{02} (defined as the flow at 0.2 proof strain) of AZ91 alloy deformed in compression is shown in Fig. 2. Similar variation of the maximum stress with temperature was obtained (Fig. 3).

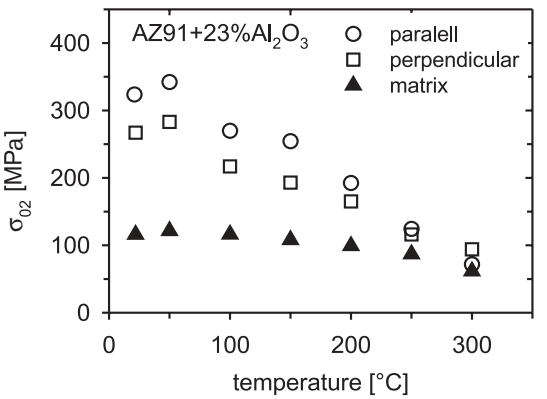

Fig. 2 Temperature dependence of unreinforced AZ91 magnesium alloys and the alloys reinforced with 23-vol. % of Al_2O_3

Between 100 and 200 °C, the decrease in the yield stress is slow. It is interesting to note that the strain (elongation) at which the

maximum tensile stress is reached decreases with temperatures above 100 °C. Dynamic recovery is observed for AZ91 specimens deformed at temperatures above 100 °C (see Fig. 1). The stress strain curves of AZ91+23 vol.% Saffil estimated in the same temperature range have similar forms as those for unreinforced alloy. The yield stress values of the composites deformed in compression are higher than those for specimens deformed in tension. The temperature dependence of the yield stress of the composite deformed in compression is also shown in Fig. 2. Planes with planar randomly distributed fibres were parallel with or perpendicular to the specimen axis (applied stress). The yield stress decreases strongly with increasing temperature. The reduction in the yield stress of the composite with temperature is higher than that of the alloy. It can be seen that short fibres and the distribution of planes with fibres influence the strength of composites. Figure 3 shows the temperature dependence of the maximum stress of unreinforced and reinforced AZ91 alloys. The strengthening effect is influenced by temperature; it decreases with increasing temperature.

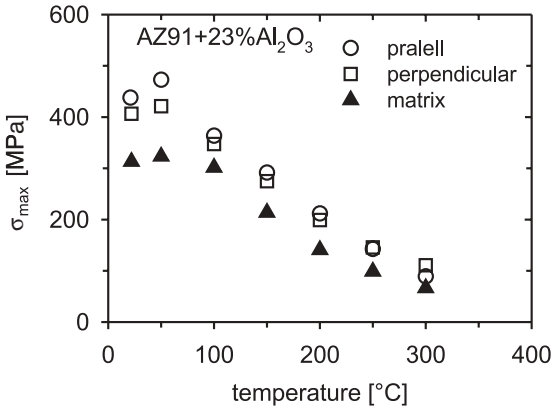

Fig. 3 Temperature dependence of the maximum stress of unreinforced AZ91 alloy and the alloy reinforced with 23-vol. % of Al_2O_3

As mentioned above, a reduction of the mean grain size is expected to increase the yield stress of a material at room temperature (the Hall – Petch relationship). In ECAP process, the material is subjected to severe plastic deformation that may be approximated to simple shear. Very high strains may be achieved, which leads to a substantial grain refinement and to an increase in the dislocation density. In the previous paper [6], the effect of the ECAP procedure on the deformation behaviour of AZ91 magnesium alloy was investigated at various temperatures at an initial strain rate of 5×10^{-4} s^{-1}. The yield stress and the maximum stress are strongly depending on the test temperature as shown in Figs. 4 and 5. It is obvious that both the yield stress and the maximum stress are higher for the ECAP processed specimens (after eight passes) up to 100 °C. Above this temperature a strong decrease of both stresses is observed. Above 100 °C the values of both the yield stress and the maximum stress are higher for the as-cast material (without ECAP processing). On the other hand, the elongation to fracture of the pressed AZ91 alloy specimens is increasing with increasing temperature above 100 °C. The elongation to fracture of AZ91 specimens after ECAP procedure is much higher than that of unpressed alloy. The elongation to fracture of specimens after eight passes in ECAP procedure deformed at 300 °C is about 80 %. The refinement of grains and a high testing

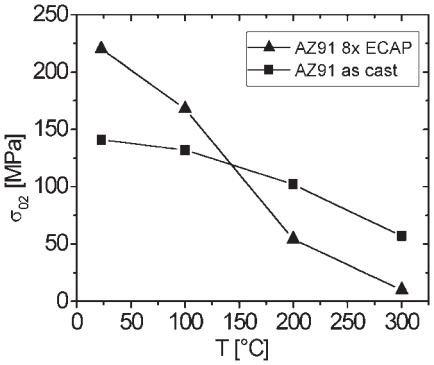

Fig. 4 Temperature dependence of the yield stress of AZ91 alloy and the alloy after ECAP procedure (eight passes)

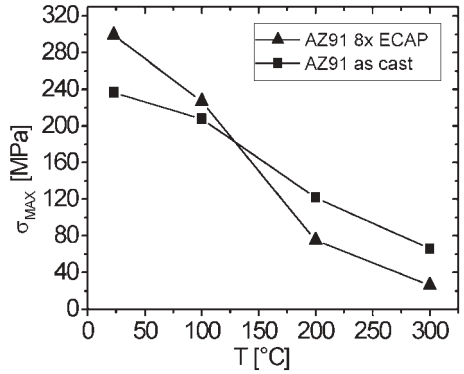

Fig. 5 Temperature dependence of the maximum stress of AZ91 alloy and the alloy after ECAP procedure (eight passes)

temperature may explain this behaviour. A reduction of the mean grain size of AZ91 alloy after the ECAP procedure increases the yield stress and the maximum stress at room temperature according to Hall-Petch relationship. The temperature of 100 °C (373 K) corresponds to 0.4 T_m, T_m being the absolute melting temperature. At this temperature, an increase in the diffusion activity may be expected. Grain boundary sliding in the ECAP processed specimens (the mean grain size was between 0.5 and 1 μm) should be considered. Kubota et al. [7] have reported that the AZ91 alloy with the grain size about 5 μm exhibits a large elongation to fracture of 340 % if deformed at 300 °C and at strain rate of 2×10^{-4} s^{-1}. Mabuchi et al. [8, 9] have reported that AZ91 alloy after the ECAP procedure (the mean grain size of about 1 μm) exhibits a large elongation to fracture of 661 % if deformed at 200 °C and at strain rate of 6×10^{-5} s^{-1}. These high values of the elongation to fracture indicate the superplastic behaviour, in which grain boundary sliding plays a significant role. At higher temperatures, larger than 200 °C, the activity of non basal slip system increases. (The activity of five independent slip systems is required for

plastic deformation of polycrystals.) In Mg and Mg alloys, where the main slip system is the basal one, the second order pyramidal slip systems may be active at temperatures above 150 – 200 °C. Not only an interaction between a and ***c*** + ***a*** dislocations but also among the pyramidal ***c*** + ***a*** dislocations can take place [10]. Different dislocation reactions can take place. Some dislocation reactions may produce obstacles for the moving dislocations. Other dislocation reactions may result in annihilation of dislocations, and therefore, cause strain softening. The macroscopic work hardening rate is a sum of hardening due to storage of dislocations at obstacles and softening due to annihilation of dislocations. During deformation, the moving dislocations can cross slip. Screw dislocations can move to the parallel slip planes by double cross slip and then may annihilate. The probability of cross slip increases with increasing temperature. Edge dislocations can climb at high temperatures. The higher temperature the more dislocations can climb. The dislocation annihilation may take place and hence, softening occurs. The changes in the shape of the stress strain curves with increasing temperature may be accounted for by considering of softening mechanisms above mentioned.

4. Conclusions

Commercial AZ91 magnesium alloys and composites with the matrix of AZ91 lose their strength at temperatures above 150 – 200 °C. They are unusable for structural application. The experimental results clearly demonstrate the significant role of temperature on the deformation behaviour of unreinforced and reinforced AZ91 alloys. The shape of the stress strain curves indicates that hardening at higher temperatures is influenced by recovery processes. Cross slip and local climb of dislocations can be regarded as possible softening mechanisms. The fibres added to the matrix increase both the yield stress and the tensile strength. The AZ91 alloys prepared by ECAP procedure exhibit higher strength at room temperature in comparison with those alloys prepared by squeeze casting. Above 200 °C, the lower strength and larger elongation of AZ91 alloys prepared by ECAP in comparison with those alloys after squeeze casting is believed to be mainly due to the occurrence of softening mechanisms. Grain boundary sliding cannot be excluded at higher temperatures, at which the superplastic deformation may be expected.

Acknowledgements – The authors are grateful for the support offered by the Czech and German authorities under the Exchange Programme CZE 01/029. P.L. greatly acknowledge the support of his stay at the University of Žilina by the CETRA (Centre for Transportation Research, Centre of Excellence).

References

[1] AUNE, T.Kr., WESTENGEN, H.: *SAE Technical Paper 950424*, Detroit 1995.
[2] PURAZRANG, K., ABACHI, P., KAINER, K. U.: *Composites Eng., 3*, 1993, p. 489.
[3] PURAZRANG, K., ABACHI, P., KAINER, K. U.: *Composites, 25*, 1994, p. 296.
[4] ARSENAULT, R. J., SHI, N.: *Mater. Sci. Eng.*, A81, 1986, p. 175.
[5] DUNAND, D.C., MORTENSEN, A.: *Acta Metall.* Mater., 39, 1991, p. 127.
[6] MÁTHIS, K., MUSSI, A., TROJANOVÁ, Z., LUKÁČ, P., RAUCH, E.: *Metal Mater. (in Czech)*, 41, 2003, p. 293.
[7] KUBOTA, K., MABUCHI, M., HIGASHI, K.: J. *Mater. Sci.*, 34, 1999, p. 2255.
[8] MABUCHI, M., IWASAKI, H., HIGASHI, K.: *Scripta Mater.*, 36, 1997, p. 681.
[9] MABUCHI, M., AMEYAMA, K., IWASAKI, H., HIGASSHI, K.: *Acta Mater.*, 47, 1999, p. 2047.
[10] LUKÁČ, P., MÁTHIS, K.: *Kovové mater.*, 40, 2002, p. 281.

Pavol Šebo – Pavol Štefánik *

THERMOPHYSICAL PROPERTIES OF COPPER – CARBON FIBRE COMPOSITE

In this paper two main properties of copper matrix - carbon fibre composite from the point of view of using it in electronics as a material able to dissipate the heat are presented. Thermal expansion and thermal conductivity of the composite can be changed in dependence on volume amount of fibres in composite, their geometrical arrangement and on the properties of carbon fibres. Propagation of heat across the composite was measured. Results are in good agreement with those obtained by finite elements method calculation.

1. Introduction

Development of new, better and more responsible products and facilities involves demand of new materials with improved properties. Among the materials fulfilling such demands belong also composite materials.

The principle of composite materials consists in fact that by the combination of two or more dissimilar materials into one unit we can obtain material with a property, or properties, which no one of the components possesses. Combination of copper which is characterised by high thermal and electrical conductivity, high density and carbon fibres which are characterised by high strength, high modulus of elasticity, low density and low, even negative coefficient of thermal expansion (CTE) can give a material with relatively high thermal conductivity, low thermal expansion and low density which can be utilised in electronic industry as heat sink, packaging for high voltage chips, cooling plate for microwave application and carrier plate which serve for heat dissipation. The coefficient of thermal expansion as well as thermal conductivity of copper-carbon fibre (Cu-C_f) composites can be tailored according to the requirement by volume fraction of carbon fibres, by using carbon fibre with appropriate thermal conductivity and Young modulus and by changing the orientation of carbon fibre in copper matrix.

The aim of this paper is to characterise thermal expansion and thermal conductivity of copper-carbon fibre composites in dependence on the volume amount of fibre in composites and their geometrical arrangement. A method, calculation and measurement of heat transport across the composite to increase the transverse thermal conductivity of Cu-C_f composite are also discussed.

2. Experiment

Cu-C_f composites are made from Torayca T300 carbon fibre with 3000 monofilaments in tow. The fibres were coated by copper to the thickness of around 1 μm. Thickness of Cu coating gives volume of copper amount in composite. Composite can be made by diffusion bonding of unidirectionally oriented fibres producing thus monolayers of the thickness $\sim$ 0.2 mm or by weaving copper coated carbon fibres. Another type of composite can be spiral or tube arrangement of copper coated carbon fibres [1].

Properties of unidirectional composites are anisotropic because of anisotropic properties of carbon fibres. To lower this anisotropy cross-ply arrangement of monolayers was used. Another type of composite with lower stress between the cross-ply monolayers due to anisotropy in thermal expansion was prepared using copper foils in-between perpendicularly oriented monolayers. Schematic view of various arrangements of fibres in Cu-C_f composites can be seen in Fig. 1. Some properties of selected carbon fibre as well as some metal (for comparison) are presented in Table 1.

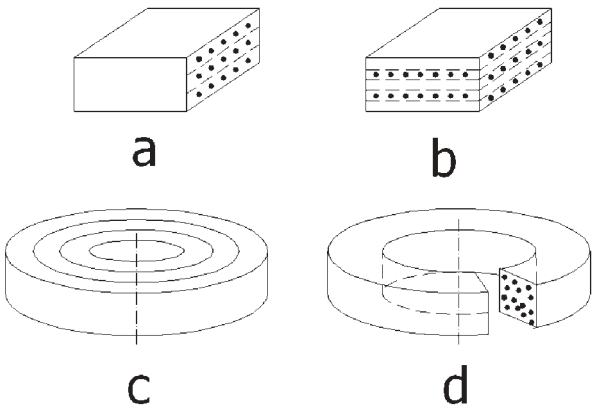

Fig. 1. Scheme of various arrangement of fibres in Cu-C_f composites: (a) unidirectional, (b) cross-ply, (c) spiral and (d) tubular.

* **Pavol Šebo, Pavol Štefánik**
Institute of Materials and Machine Mechanics, Slovak Academy of Sciences, Račianska 75, 831 02 Bratislava, Slovakia, E-mail: ummssebo@savba.sk

Some properties of selected carbon fibres and several metals. Table 1

Material	Density [kgm^{-3}]	Strength [GPa]	Young modulus [GPa]	Thermal conductivity [Wm^{-1}K^{-1}]	CTE [10^{-6} K^{-1}]
Al	2700	0.08	69.5	237	24
Cu	8960	0.2	125	400	17.5
Steel	8260	3.8	210	48	11.7
C_f T300	1760	3.6	231	5	-0.5
C_f P120S	2180	2.2	827	640	-1.44
C_f K3D2U	2200	3.7	935	800	
C_f K1100X	2200	3.1	956	1060	-1.4
VGCF				1500	

3. Results and discussion

3.1. Thermal expansion

A large number of models for prediction of thermal expansion was developed. For longitudinal (L) coefficient of thermal expansion (CTE) of two phases composite Shapery [2] derived an equation

$$\alpha_{CL} = \frac{\alpha_{FL} V_F E_{FL} + \alpha_M (1 - V_F) E_M}{V_F E_{FL} + E_M (1 - V_F)} \quad (1)$$

for transverse (T) CTE we used equation

$$\alpha_{CT} = (1 - V_F)(1 + \nu_M) \cdot \cdot (M + V_F (1 + \nu_{FL}) \alpha_{FT} - \nu_C \nu_{CL} \quad (2)$$

where α, V, E, ν are CTE, volume fraction, Young modulus and Poisson number, indices C, M, F, L and T are for composite, matrix, fibre, longitudinal and transverse direction, respectively.

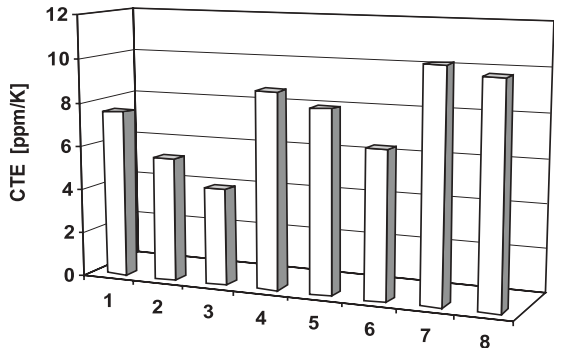

Fig. 2. Coefficient of thermal expansion of Cu-C_f composite for various fibre arrangement. (1), (2), (3) unidirectional (in fibre direction) with 40, 50 and 60 vol.% carbon fibre, respectively, (4), (5), (6) cross-ply with 47, 50 and 57 vol.% C_f, respectively and (7), (8) woven composite with 47 vol.% C_f in x and y directions, respectively.

The measurement of CTE was performed in push-rod dilatometer [3]. Unidirectional specimens were measured in direction parallel and perpendicular to the fibre orientation and cross-ply and woven samples were measured in the direction along the fibres and in transverse direction (perpendicularly to the fibre plane).

The results obtained by measurement of CTE for various fibre amount and various geometrical arrangement of fibre are summarised in Fig. 2. As can be seen from Fig. 2 these values of CTE can be tailored by selection of proper fibre amount, and their arrangement. The mean CTE of Cu-C_f composite should be in the range of $(4 - 9) \times 10^{-6}$K^{-1} to match the one of the electronic materials e.g. Si ($\alpha = 4.1 \times 10^{-6}$K^{-1}), Al_2O_3 ($\alpha = 6.5 \times 10^{-6}$K^{-1}). As it can be seen in Fig. 2 the cross-ply and woven composites of appropriate fibre content are candidate materials for the heat sinks and packaging plate application.

3.2. Thermal conductivity

Copper-carbon fibre composite as an anisotropic two components material possesses two thermal conductivities – longitudinal and transverse. Longitudinal thermal conductivity can be expressed by rule of mixtures.

$$\lambda_{CL} = \lambda_{FL} V_F + \lambda_M (1 - V_F) \quad (3)$$

transverse thermal conductivity λ_{CT} of unidirectional composite was derived by Hatta and Taya [5]

$$\lambda_{CT} = \lambda_M \frac{\lambda_M (\lambda_{FT} - \lambda_M) V_F}{\lambda_M + (1 - V_F)((F_T - \lambda_M)/2} \quad (4)$$

where λ and V are thermal conductivity and volume amount, respectively and indices C, L, T, F, M are for composite, longitudinal, transverse, fibre and matrix, respectively.

Thermal conductivity was measured by laser flash method. The method measures the thermal diffusivity of a material and thermal conductivity is calculated according to

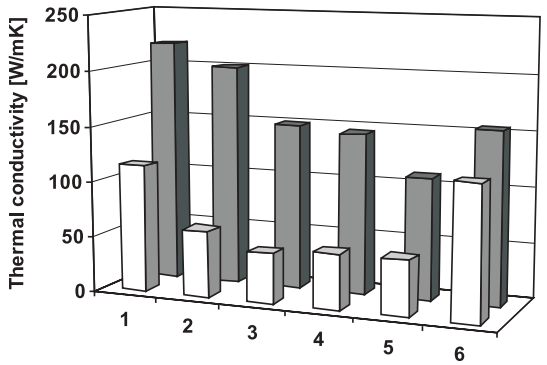

Fig. 3. Thermal conductivity of Cu-C_f composite in longitudinal (rear line) and transverse (front line) for various fibre arrangement: (1), (2), (3) unidirectional with 40, 50 and 60 vol.% C_f, respectively, (4), (5) cross-ply with 50 and 60 vol.% C_f and (6) woven with 40 vol.%.

$$\lambda = a\, c_p\, \rho \qquad (5)$$

where c_p and ρ are specific heat and density of a material.

Thermal conductivity of Cu-C_f composite in longitudinal (rear) and transverse (front line) direction for various fibre arrangements is in Fig. 3.

The required thermal conductivity of a heat sink material given by an end user, is at least 150 $Wm^{-1}K^{-1}$. As can be seen from the presented results the transverse thermal conductivity is very low. This direction of thermal conductivity is for heat dissipation in electronic packaging the most important. From the CTE point of view the most suitable composite for heat sink application are woven or cross ply composites with 45 vol.% of fibres.

In real construction the heat is scattered not only in z (transverse) direction but also in x, y plane and heat sink insure the cooling practically from whole of its opposite surface.

To understand the propagation of heat in composite material we measured the temperatures in several surface points of composite. Halogen lamp gives a heat through glass bar, which produces, round light area of a diameter 10 mm in the centre of specimen of dimension 50 × 50 × 1 mm [7]. Propagation of heat was measured by thermocouples in various distance from the centre of specimen with perpendicular and parallel direction to fibres. Accuracy of the apparatus was tested on homogeneous copper plate. Obtained results were compared with the calculation of the temperature distribution by finite elements method using the software ANSYS [8].

Typical curves showing dependence of temperature on time for Cu-C_f composites containing 40 vol.% fibres are in Figs. 4a, b. Thin lines are experimental results, thick lines are for calculated dependencies for the same specimen. The digits in the brackets (co-ordinates) give distance (in mm) of thermocouples location from the centre of the sample. Co-ordinate $z = 0$ means the front of the sample, $z = 1$ means back side of the specimen.

Comparison of experimental and calculated results gives the density of heat flux around 16000 Wm^{-2}. Temperature increasing in composite with unidirectionally arranged fibres in the amount of 40 vol.% in the same distance from the centre of the specimen is approximately equal to that one in homogeneous material. For higher amount of fibres in composite (63 vol.%) the temperature increasing in fibre direction is more expressive where low thermal conductivity of fibres in transverse direction has already been manifested.

Increasing the in-plane and transverse thermal conductivity of the composite can be generally achieved by adding as much as possible the highest thermal conductive material, in our case of copper, taking into account technological problems as well as the influence of copper on other properties of composite, e.g. CTE. Ting, Lake and Duffy [6] developed vapour grown carbon fibre (VGCF) as reinforcement in carbon and aluminium matrices for

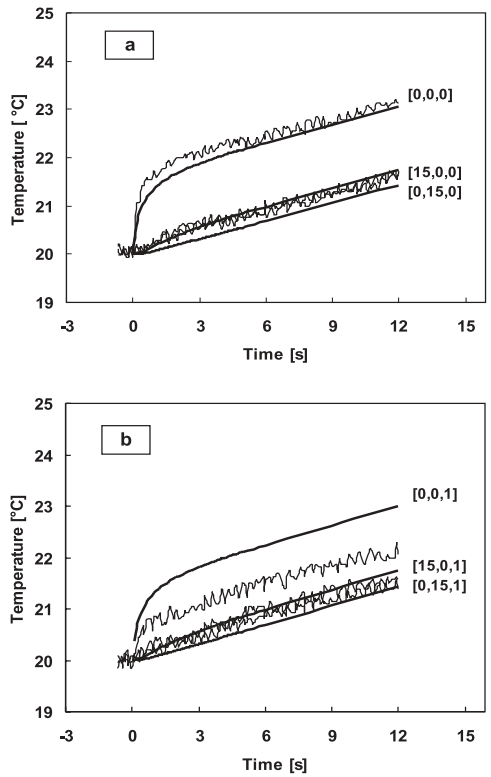

Fig.4. Experimental (thin) and calculated (thick line) temperature dependence on time of heating of Cu-C_f composite with 40 vol.% fibres. (a) front, (b) back side of the specimen.

thermal management. Thermal conductivity of Al matrix composite with 36.5 vol.% VGCF was 642 $Wm^{-1}K^{-1}$ and that one with carbon matrix was 910 $Wm^{-1}K^{-1}$.

The increase of thermal conductivity of Cu-C_f composite can be done in several ways [7]

- using carbon fibre with high axial thermal conductivity

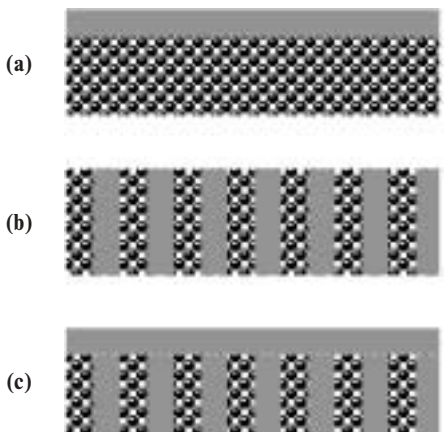

Fig. 5. Scheme of Cu elements in composite: (a) foils, (b) bridges, (c) foil and bridges.

- coating skeleton of carbon fibres with high conductive carbon by chemical vapour deposition followed by pressure infiltration of copper
- adding the Cu foils on the surface of Cu-C_f composite to increase in-plane thermal conductivity (Fig. 5a)
- constructing copper bridges in transverse direction (Fig. 5b)
- combining last two points to increase both longitudinal and transverse thermal conductivity (Fig. 5c)

First experiments concerning the increase of transverse thermal conductivity by construction of copper bridges (Fig. 5b) were done and preliminary results were obtained [10].

4. Conclusion

The obtained results demonstrate the possibility of preparing copper matrix – carbon fibre composite material with the properties suitable for using it as heat dissipation material. The coefficient of thermal expansion can be controlled in the interval of $(4 - 9) \times 10^{-6}K^{-1}$. Thermal conductivity in longitudinal direction in the interval of (100 – 220) $Wm^{-1}K^{-1}$ and in transverse direction of (50 - 100) $Wm^{-1}\,K^{-1}$ in dependence on the amount of fibres and their arrangement in composite. To increase the transverse thermal conductivity, propagation of heat across the composite was measured in dependence on volume amount of fibres. For low volume amount (40 %) of fibres the heat dissipation is close to that of homogeneous material, for higher amount (63 %) of fibres the temperature increase is higher in all measured points. The results are very close to the results obtained by finite elements method calculation.

References

[1] ŠEBO, P., ŠTEFÁNIK, P.: *Inter. J. Mater. Product Technology* 18, 2003, pp. 141-159.
[2] SHAPERY, R. A.: *J. Comp. Mater.* 2, 1968, pp. 380-404.
[3] KORÁB, J.: *Ph.D.Thesis,* Technical University, Wien, 1999.
[4] KORÁB, J., ŠTEFÁNIK, P., ŠEBO, P., KAVECKÝ, Š.: *Proc. 6th Internat. Conf. Technológia '99*, Bratislava, Sept. 8-9, 1999, pp. 96-99.
[5] HATTA, H., TAYA, M.: *J. Appl. Phys.* 59, 1986, pp. 1851-1860.
[6] TING, J. M., LAKE, M. L., DUFFY, D. R.: *J. Mater. Res.* 10, 1995, pp. 1478-1484.
[7] HUDCOVIČ, P., ŠTEFÁNIK, P., VOZÁR, L.: *Proc. 9th Internat. Conf. CO-MA-TECH 2001*, Trnava, Oct.25-26, 2001, pp. 80-85.
[8] ŠTEFÁNIK, P., BEHÚLOVÁ, M., HUDCOVIČ, P.: *Proc. 4th Conf. Konštrukčné materiály 2003*, Bratislava, May 6, 2003, pp. 16-22.
[9] HUDCOVIČ, P., VOZÁR, L., ŠTEFÁNIK, P.: *Proc. Thermophysics 2001*, Račkova dolina, Oct.23, 2003, pp. 49-54.
[10] KAVECKÝ, Š., ŠTEFÁNIK, P., ŠEBO, P.: *Proc. 4th Conf. Konštrukčné materiály 2003*, Bratislava, May 6, 2003, pp. 10-15.

Ján Micheľ – Marián Buršák *

INFLUENCE OF THE STRAIN RATE ON THE NOTCH TOUGHNESS OF COLD-FORMING STEELS

The paper analyses the influence of the strain rate with loading rates of $1.7.10^{-5} - 4.8\ m.s^{-1}$ on the notch toughness of hot-rolled microalloyed steels S 315 MC and S 460 MC and cold-rolled deep-drawing steels DC 06, H 220 B and H 220 P. It discusses a possibility of utilising a modified notched-bar impact test to predict the formability of these steels at high strain rates of thin steel sheets.

Key words: *notch toughness, strain rate, microalloyed steel, drawing steel*

1. Introduction

The influence of the strain rate in the forming process can be formulated in such a way that the resistance of metal against dislocation movement increases with an increasing strain rate, which has an impact on an increase in the yield point, the tensile strength, a change in the deformation characteristics, etc. A localization of plastic deformation can occur and at higher strain rates the whole process assumes an adiabatic character [1]. The influence of the strain rate on the strength and deformation characteristics is significantly influenced by the structure of metallic material.

The notched-bar impact test is one of the simplest tests making it possible to assess the behaviour of materials under the dynamic loading conditions and expressing the active fracture resistance in a narrow zone of the tested cross-section [1, 2]. Its disadvantage consists in the fact that it does not make it possible to obtain absolute values of material toughness that would characterize the fracture resistance. The notch toughness is influenced by the size and shape of the notch of the test bar, while their influence on the notch toughness depends on the internal structure of material. Nowadays, the test is usually made using standard tests bars with the dimensions of $10 \times 10 \times 55$ mm and with the V notch with the depth of 2 mm, the diameter $r = 0.25$ mm and the angle of 45°. Even though there are more exact tests to determine material fracture resistance [1, 2], the notched-bar impact test is the most used one in practice for its simplicity. Its application to testing the notch toughness of semi-products and products from which standard test bars cannot be made necessitated studying the influence of the test bar thickness, the notch shape, the specimen dimensions, as well as the loading rate, etc. on the characteristics that can be obtained using the notched-bar impact test [3, 4, 5, 6, 7].

The goal of this paper is to analyse the influence of the loading rate on the notch toughness of cold-forming steels with higher tensile strength values and, based on this analysis, to assess a possibility of utilizing the notched-bar impact test to predict their formability at increased strain rates, which is necessitated by the practice at present.

2. Experiments and their analysis

The experiments were made on hot-rolled micro-alloyed steels S 315 MC and S 460 MC with the thickness of 8 mm and on cold-rolled deep-drawing steels DC 06, H 220 B and H 220 P with the thickness of 0.8 and 1 mm.

Basic mechanical properties and characteristic of tested steels — Table 1

Steel	Thickness [mm]	R_e ($R_{p0.2}$) [MPa]	R_m [MPa]	A_5 [%]	Z [%]	Characteristic of steel
S 315 MC	8.0	390	477	38	80	Micro-alloyed steel C = 0.05 %, Nb = 0.042 %, thermomechanically rolled, suitable for cold rolling
S 460 MC	8.0	537	625	30	76	Micro-alloyed steel C = 0.07 %, Nb = 0.052 %, V = 0.082 % thermomechanically rolled, suitable for cold rolling
DC 06	0.8	145	283	45	–	C < 0.015 % recrystallization annealed, extra deep-drawing
H 220 B	1.0	224	347	36	–	C < 0.06 % drawing steel, hardened during paint baking
H 220 P	1.0	250	369	31	–	C < 0.06 %, P < 0.08 %, drawing steel with increased dent resistance

* **Ján Micheľ, Marián Buršák**
Department of Material Science, TU Košice, Park Komenského 11, 04 200 Košice, Tel.: 055/602 27 61, Fax: 055/602 22 43,
e-mail: Marian.Bursak@tuke.sk

The basic mechanical properties and characteristic of the tested steels are given in Table 1.

From the strips of the tested steels, materials were taken in the rolling direction and the following test bars were made: from steels S 315 MC and S 460 MC – with the dimensions of 10 × 8 × × 55 mm and the V notch with the depth of 2 mm, and from steels DC 06, H 220 B and H 220 P – with the dimensions 8 × (sheet thickness) × 28 mm and the V notch with the depth of 4 mm. The shape and dimensions of these test bars were based on obtained practical knowledge.

The notched-bar impact test was made at two or three loading rates on different testing machines given in Table 2.

Loading rates and used notched-bar testing machines Table 2

Loading rate v [m.s^{-1}]	Strain rate $\dot{\varepsilon}$ [s^{-1}]	Used machines
$v_1 = 1.7.10^{-5}$	$1.1.10^{-3}$	Tensile testing machine ZD 100/I + fixture
$v_2 = 5.10^{-2}$	3.3	Fatigue testing machine INSTRON 8511 + fixture
$v_3 = 4.8$	$3.2.10^{2}$	Pendulum impact testing machine PSWO 1000

The required test bar failure energy at the loading rates (v_1 and v_2) was evaluated by planimetring the area of the force F – deflection diagram.

Fig. 1 shows the influence of the loading rate (v) during the notched-bar test on the *KCV* values at 20 °C. It results from Fig. 1 that the *KCV* values of steels S ... MC are significantly higher than that of the other tested steels, during both the static loading (v_1) and the impact loading (v_3). This is, besides different mechanical values, due to different dimensions of the test bars, which has a significant influence on the *KCV* value.

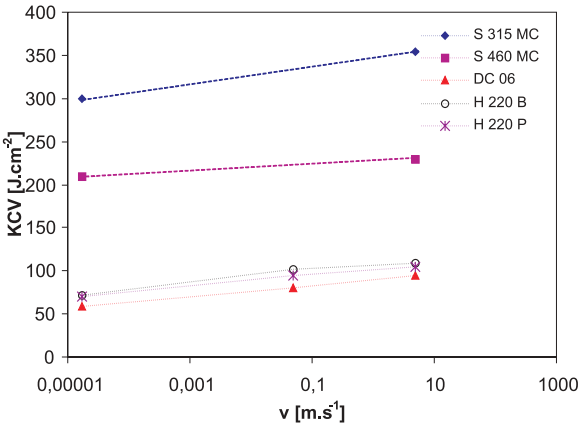

Fig. 1. Relationship between KCV and loading rate of tested steels

The evaluation of the influence of the property (structure) of the tested steels on the loading rate can be made e.g. using the following relationship

$$KCV_{v3} = k \,.\, KCV_{v1} \qquad (1)$$

where KCV_{v3} is the notch toughness at the loading rate v_3 = = 4.8 m.s^{-1}, KCV_{v1} is the notch toughness at the loading rate $v_1 = 1.7.10^{-5}$ m.s^{-1} and k is a material constant expressing the sensitivity of steel to the change of the loading rate.

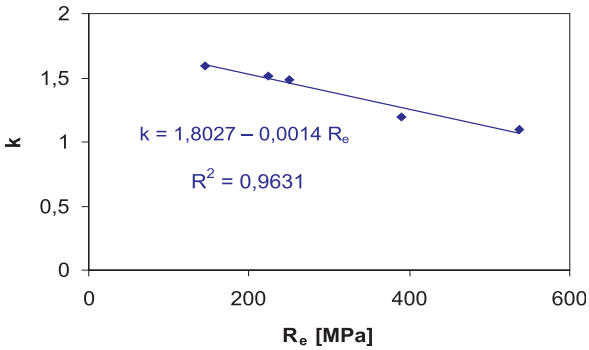

Fig. 2. Relationship between the constant of material sensitivity to the loading rate change from $1.7.10^{-5}$ to 4.8 m.s^{-1} and the yieald point R_e of tested steels

Fig. 2 shows the relationship between the k constant and the yield point of the tested steels, demonstrating that the higher yield point of steel the less sensitivity of steel to the strain rate. The yield point can be considered as a macroscopic structural characteristic. The matrix of all the tested steels is ferritic. The increase in the yield point of H 220 B and H 220 P steels is due to the BH effect and the phosphorus content, and that of S 315 MC and S 460 MC steels is due to fine grains and precipitation hardening. This means that the more dislocation movement obstructions in the steel structure the less sensitivity of steel to the strain rate [1, 8, 9, 10, 11]. For the tested steels, the material constant k can be analytically expressed using the following parametric equation

$$k = A - B \,.\, R_e \qquad (2)$$

For the tested steels, the constant A = 1.8027 and the constant B = 0.0014.

For S 315 MC and S 460 MC steels, a temperature dependence of the notch toughness was constructed for the static loading ($v_1 = 1.7.10^{-5}$ m.s^{-1}) and the impact loading ($v_3 = 4.8$ m.s^{-1}). The results are shown in Fig. 3 and Fig. 4. It results from the figures that at the static loading the *KCV* values in the super-transitional area are lower than at the impact loading, and the transitional temperature at the static loading is also lower. If we take the temperature at which KCVmax decreases by its half (T50) as the transitional temperature, this temperature at the static loading is 41 °C lower than at the impact loading for S 315 MC steel and as few as 19 °C lower for S 460 MC steel (see Fig. 3 and Fig. 4). The results are in accordance with literature knowledge [1] that with

an increasing strain rate the susceptibility of metals to brittle failure increases and that the sensitivity to the strain rate under the same external conditions is a function of the structure.

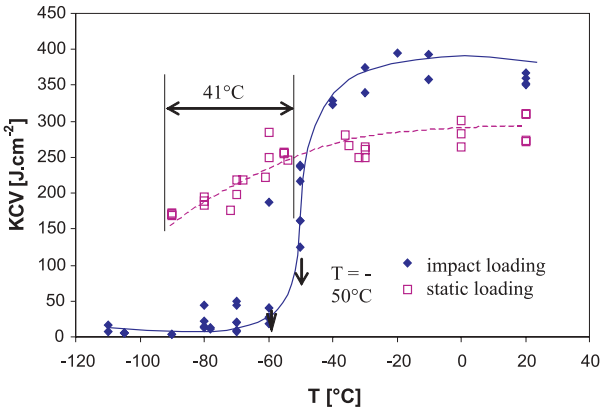

Fig. 3. Temperature dependence of KCV S 315 MC steel

It resulted from the experiments and their analysis that the notched-bar impact test can also be made, while meeting certain conditions, on thin steel sheets applied in the automotive industry. The notch toughness values in the super-transitional area are higher at a higher rate and this increase is a function of the structure, whose macroscopic characteristic is the yield point. With an increasing strain rate, the susceptibility of the tested steels to brittle failure (unstable crack propagation) increases.

The above-mentioned conclusions enable us to assume that a modified notched-bar test can serve to predict the formability of drawing steels at increased strain rates. With an increasing strain rate, the strain work increases, in dependence on the strength characteristics of steel ($k = A - B \,.\, R_e$). If the notch toughness at the required strain rate v_x (KCV_x) is higher that at the static strain rate v_s (KCV_s), at this strain rate the formability of steel sheet can be assessed according to traditional formability criteria. In case that KCV_x is less than KCV_s, at the strain rate v_x there is a risk of plastic instability and, as a result, a local failure. Such a condition may occur for example in S 315 MC steel at the temperature of −50 °C (see Fig. 3), but also when the critical strain rate is exceeded, where the relationship $KCV_x = k \,.\, KCV_s$ does not apply and where there is a risk of sudden fracture.

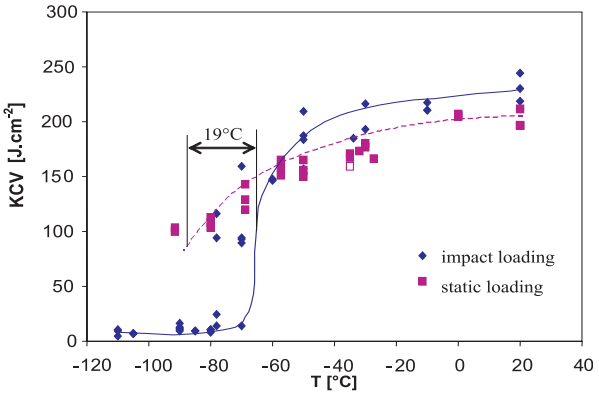

Fig. 4. Temperature dependence of KCV S 460 MC steel

3. Conclusion

The paper analyses, based on the experiments, the influence of the loading rate on the notch toughness of hot rolled microalloyed steels suitable for cold working (S 315 MC and S 460 MC) and cold rolled drawing steels (DC 06, H 220 B and H 220 P). Possibilities of utilizing the notched-bar impact test results to assess the formability of steels at higher strain rates are also discussed. It results from the analysis that:

- the notched-bar impact test can also be applied to thin sheets (~ 1 mm), but the test bar shape must meet certain conditions, in particular the bar height to the notch depth ratio,
- in the super-transitional area, the notch toughness increases with an increased loading rate in the interval from $1.7.10^{-5}$ to 4.8 $m.s^{-1}$, while this increase rate is a function of the structure of the tested steel,
- with an increasing loading rate, a risk of unstable crack propagation increases (the transitional temperature increases),
- a modified notched-bar impact test can serve to predict the formability of steel sheets at increased strain rates, mainly as regards the prediction of the strain resistance, the loss of plastic stability and a possibility of using traditional formability criteria at increased strain rates; standardized tests of deep-drawing properties of steel sheets are practically static ($\dot{\varepsilon} \approx 10^{-3} s^{-1}$), however, in the technical practice steel sheets are processed at rates of as many as 1 – 10 s^{-1}.

References

[1] VELES, P.: *Mechanické vlastnosti a skúšanie kovov,* ALFA Bratislava, 1989
[2] KÁLNA, K.: *Zváranie - Svařování,* 49, 2000, 11-12, 239
[3] HIDVÉGHY, J., MICHEĽ, J., BURŠÁK, M.: *Zváranie - Svařování*, 49, 2000, 11-12, 243
[4] MANAHAN, M. P.: *Advances in notched bar impact testing,* ASTM Standardization News, 1996, No 10, 23
[5] MICHEĽ, J., BURŠÁK, M.: *Oceľové plechy*, 1994, 1, 26
[6] DLOUHY, I., HOLZMANN, M., KOZÁK, V.: *Zváranie - Svařování*, 49, 2000, 11-12, 247
[7] MICHEĽ, J., BURŠÁK, M.: *Oceľové plechy*, 19, 1994, 1, 26
[8] MICHEĽ, J.: *Materiálové inžinierstvo*, 3, 1996, 2, 22
[9] ČIŽMÁROVÁ, E. – ET AL.: *Metallurgija*, 41, 2002, 4, 282
[10] ŠLESÁR, M., GERŐ, R., MICHEĽ, J.: *Kovové mater.* VII, 1969, 1, 87
[11] SCHNIDLER, I., BOŘUTA, J.: *Utilization Potentialities of the Torsion Plastometer*, OLDPPRINT, Žory, 1998

Dušan Kniewald – Janette Brezinová – Anna Guzanová *

THE STUDY OF MATERIAL CHANGES IN SHOT BLASTING PROCESS

The contribution deals with the blasting process from the point of view of degradation phenomena. The interaction of blasting material with the blasted surface causes changes in both blasting material and substrate. In this paper we investigate the wear of various blasting materials and the degradation of the substrate surface. On the basis of the evaluation of studied phenomena in blasting process the classification of upgrading and degrading effects was carried out.

***Keywords**: upgrading and degrading phenomena, degradation of blasting media, degradation of blasted material*

1. Introduction

Blasting technology belongs to the mechanical surface machining group. Machining tool, i.e. blasting material, produces upon impact qualitative changes in the surface layers of substrate, forming a typical surface morphology.

Blasted surface cannot be classified, on the basis of its technological origin, within the basis group of mechanically treated surfaces, i.e. as a "new" surface, created by cutting operations, or as a deformed surface created by mechanical working [1, 2, 3].

Final blasted surface is produced both by the surface layer deformation and by removing a part of substrate material. Blasted surface is multiple-loaded by blasting material; therefore it accumulates plastic deformation. Under the influence of multiple surface loading the surface layers change their dimensions, geometrical characteristics, structural properties, stress state etc. Thermal effects of the blasting process can induce structural changes of substrate surface and subsurface layers. These changes induced mainly by mechanical effects can affect macro-, micro-, or submicroscopic volumes of blasted surface layers.

Impact of blasting material on the blasted substrate produces qualitative changes in both involved subjects, i.e. in blasting material and in substrate.

2. Substrate degradation in the blasting process

The influence of the blasting process on the substrate can be separated into upgrading and degrading effects. However, since blasting process is a very complex one, no unanimous classification of various effects is possible. In many cases upgrading effects may be considered also as degrading effects [4]. Character of these effects depends upon the aim and purpose of the surface pre-treatment. Schematic classification of blasting effects on substrate is shown in Fig. 1.

Mechanical surface pretreatment creates suitable surface roughness for perfect anchoring of subsequently applied coatings. Final blasted surface is formed by the deformation of surface and peaks, and by their partial change, in dependence on the blasting angle, see Fig. 2, Fig. 3. Metallographic analysis shows, that during blasting process material is transferred and new configuration of extrusions is formed. When blasting angle is small a cutting (grooving) effect dominates and microchips are formed. For larger blasting angles a forging effect dominates, in dependence on the relation between the substrate and blasting material hardness. Due to intensive deformation processes in surface layers and due to the removal of an intermediate layer a surface with high activity is produced during blasting. This fact contributes significantly to the corrosive resistance of subsequently formed coatings. Real surface enlargement improves the adhesion of coatings on blasted substrates. But new surfaces formed by blasting are characterized by a fast decrease of their activity due to their reaction with the atmosphere. This decrease of surface activity has negative impact to the adhesion of coating applied to these surfaces. Blasting process may be considered as a process for improving mechanical and technological properties of metallic materials. Blasting involves plastic deformation of substrate surface layers, leading to the strengthening of these layers and to the appearance of mainly compressive stresses. This enhances the material resistance to cyclic fatigue. Surface purity is determined by the degree of removing scale, rust products, old coatings and other impurities. In the process of blasting the above-mentioned impurities are removed from the surface (upgrading effect), but, on the other hand, the surface is secondary contaminated by embedded grains, by parts of blasting material adhering to the surface and by free dust particles (degrading effect).

Blasting process is thus accompanied with some degrading effects related to the substrate and to the blasting material. It is

* **Dušan Kniewald, Janette Brezinová, Anna Guzanová**
Deparment of technology and materials, Faculty of Mechanical Engineering, Technical university, Masiarska 74, SK-040 01 Košice,
E-mail: Dusan.Kniewald@tuke.sk, Janette.Brezinova@tuke.sk, anna.guzanova@tuke.sk, Phone: +421-55-6222742

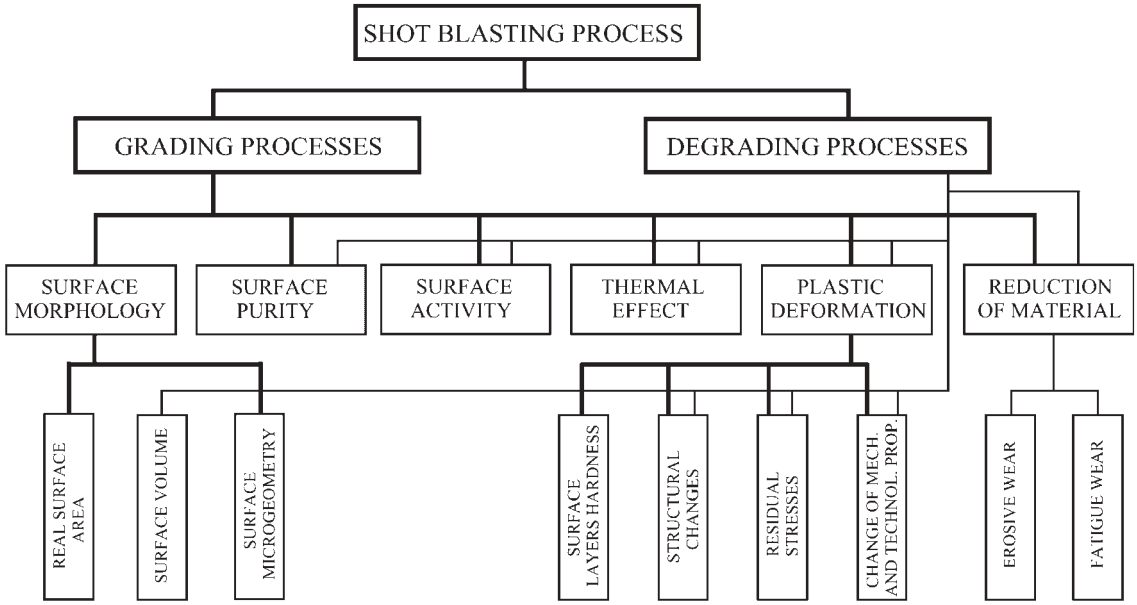

Fig. 1 Schematic classification of blasting effects on substrate [4]

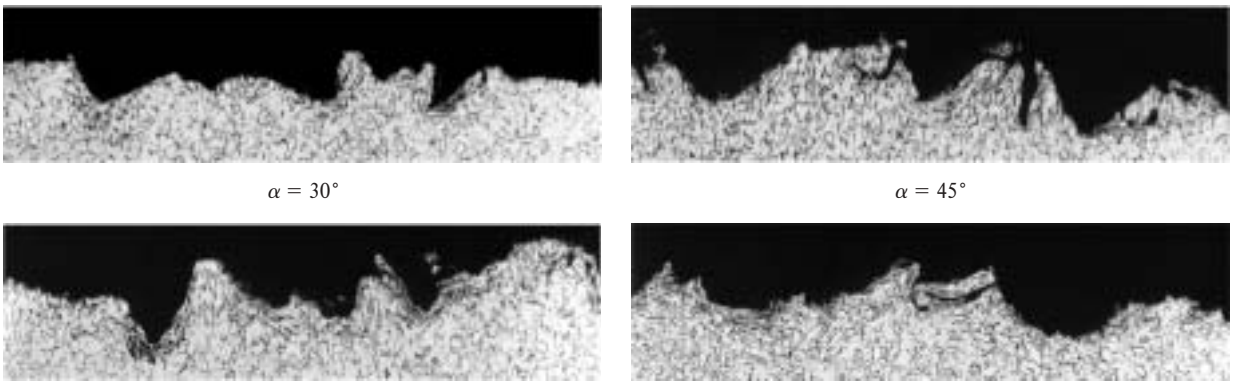

$\alpha = 30°$ $\alpha = 45°$

$\alpha = 75°$ $\alpha = 90°$

Fig. 2 Cross sections of shot blasted substrate in shot blasting medium direction, when $d_{zD} = 0.9$ mm [4]

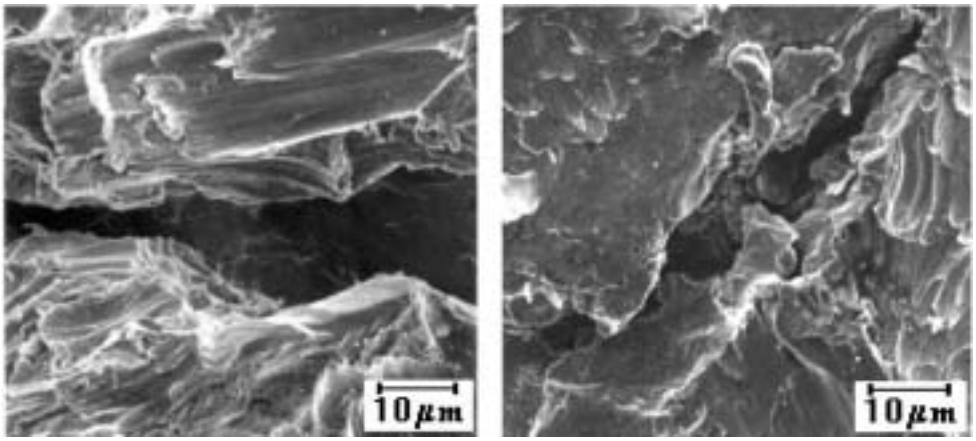

a) b)

Fig. 3 SEM photos of shot blasted surface when the blasting angle was: a) α = 30°, b) α = 90° [4]

necessary to pay proper attention to these effects, according to their significance. During blasting process substrate material is removed in the form of microchips. Removal of rust products and other impurities from the surface may be considered as upgrading effect. However, due to the increasing degree of coverage after multiple impact of blasting material grains the removal of the basis material begins to take place, followed by the surface delamination [4], Fig. 4. Surface layers separation depends probably mainly on defects presence in material. From this point of view this effect may be considered as degrading. Delaminating effect is a result of an incorrect blasting regime, which may be termed as surface "overblasting". Blasting material grains are also cyclically loaded during the blasting process. Change of shape and reduction of grain size by breaking occurs due to repeated loading during blasting. At the same time both substrate and blasting material are subjected to thermal load.

The wearing process of *metallic blasting media* is characterized as follows [5]:

- *cut wire*
  - rounding and slow abrasion wear,
  - intensive blasting media flaking and grain breaking,
  - slow wear down to the formation of dust particle, Fig. 5a
- *steel shot*
  - breakdown of double, cavernous and oval grains created by granulation,
  - gradual wear down to their total disintegration, Fig. 5b,
- *cast iron grit* – grain wear by fracturing is very intensive from the beginning of their use, Fig.5c.

Wear of *non-metallic blasting materials* is characterized by a different wearing mechanism (mainly brittle fracture), resulting from their material characteristics. Tougher and softer blasting materials are visibly deformed, hard and brittle materials crumble and break upon their impact on substrate. Wear of non-metallic blasting materials is more intensive when compared with metallic blasting materials, which is evident also from the changes of the blasted substrate appearance. Fig. 6 shows appearance changes of a substrate blasted by mineral blasting material – natural garnet Bohemia with grain size $d_{zD} = 0.56$ mm – after the first, tenth and twentieth blasting cycle. 3D pictures of shot blasted surface were obtained by a modified stylus profilometry method [6].

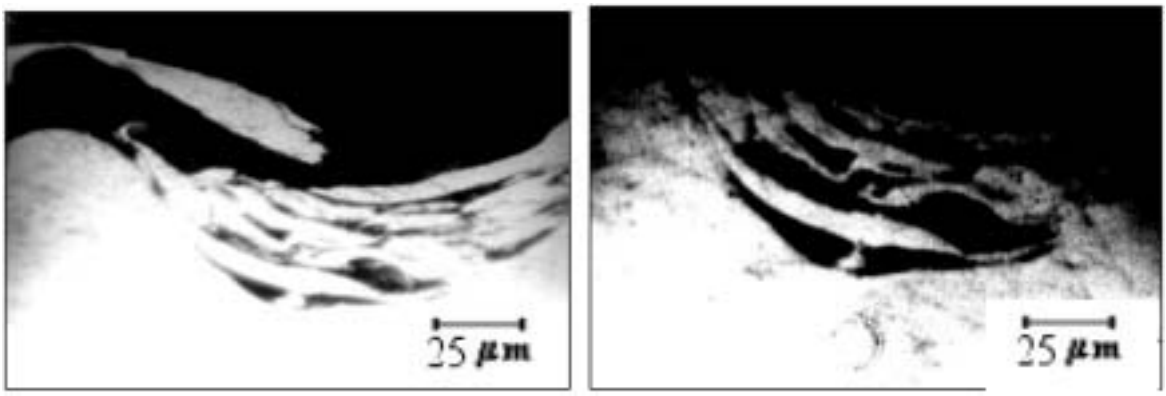

Fig. 4 Surface delamination [4]

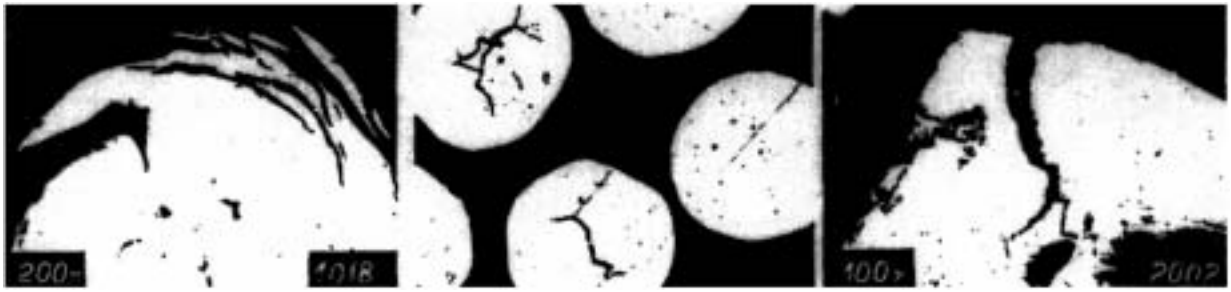

a) b) b)

Fig. 5 Blasting material grain wear (a – cut wire, b – steel shot, c – iron grit) [5]

3. Blasting material degradation during blasting process

Periodical use of blasting material in the blasting process induces its intensive wear. The character of this wear is determined by the type of blasting material, the shape and size of its grains, by blasting parameters (grain impact velocity, blasting angle) and by the quality of substrate material. Continuous gradual wear results in the change of blasting material grain size, producing new grain fractions. Wearing mechanism of metal and non-metal blasting materials is different.

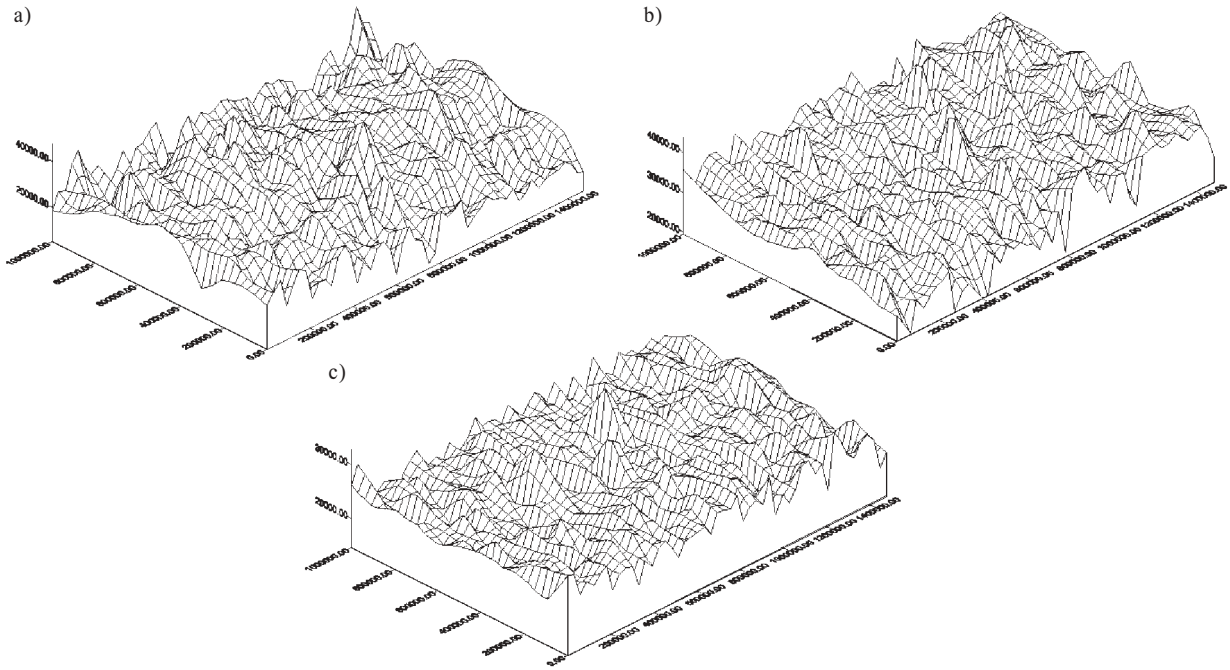

Fig. 6 3D view of surfaces blasted by: a) GBM 0.56 mm after the first blasting cycle, b) GBM 0.56 mm after 10th blasting cycle, c) GBM 0.56 mm after 20th blasting cycle [6]
GBM – Garnet Bohemia – $Fe_3Al_2(SiO_4)_3$; HK – Brown Corrundum

Intensive crumbling of non-metallic blasting material causes change and enlargement of the grain size range. Fig. 7 shows the change from monodisperse to polydisperse blasting material (Bohemia garnet and brown corundum with grain size 0.56 mm) after 20th blasting cycles.

Blasting material degradation is closely connected with its durability. Durability of blasting materials can be determined by several methods:

- *screening analysis method* – this method is based on the detection of the particle portion on nominal screen and it changes in dependence on a number of cycles. Durability of blasting material according to this method is expressed by a number of cycles after which the mass of the blasting medium on the nominal screen is reduced by 50 per cent – marked as K_{50}.
- *grain crumbling method* – is based on determining the increase of the number of blasting material grains during the blasting process. Durability of blasting material according to this method

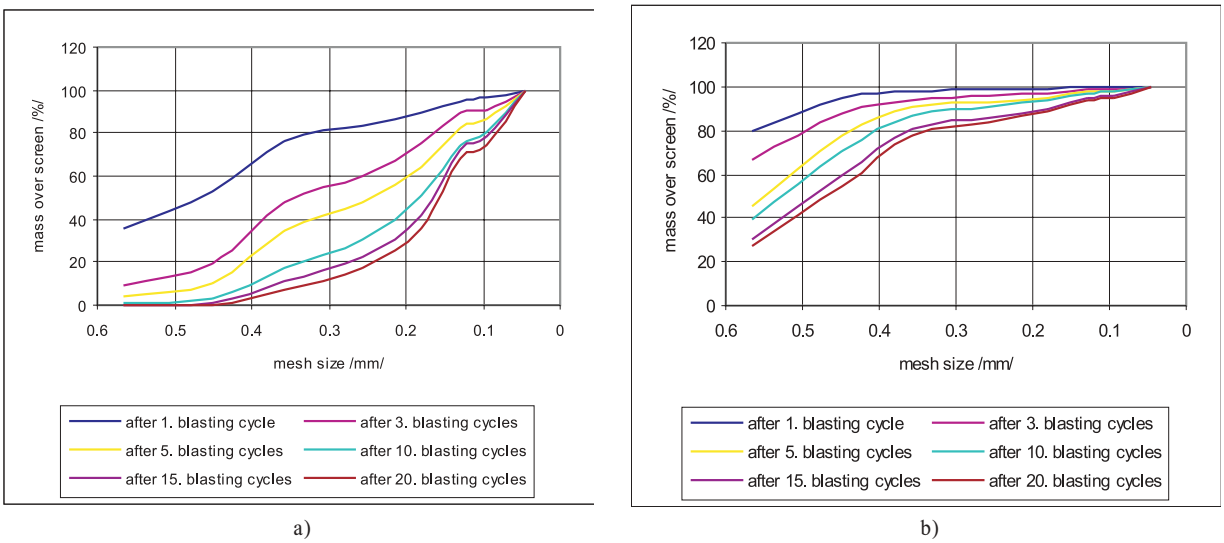

Fig. 7 Cumulative screening curves for a) GBM 0.56 mm and b) HK 0.56 mm [6]

is expressed by a number of blasting cycles after which the number of blasting material grains in a weight unit is doubled. This method is very laborious because the grains have to be manually counted and the loss of grains during the blasting process must be prevented.

- *surface roughness method* – is based on the fact that the roughness of blasted surface decreases with progressing blasting. Durability of a blasting material according to this method is expressed by a number of cycles after which the surface roughness parameter Ra of the blasted surface decreases by about 15 per cent.
- *total wear method* – it is a time consuming method, because blasting material is used until it is totally deteriorated. Total wear means that every blasting material grain has certain minimal size – e.g. 0.1 mm.
- *blasting material crumbling coefficient* k_{DTP} – is expressed as a ratio of the blasting material mass on nominal screen to the total initial blasting material mass after one blasting cycle.

An example of durability determination of metallic blasting materials by screen analysis method for cut wire and steel shot with grain sizes of 0.6 mm and 1.2 mm is shown in Fig. 8. Durability of a metallic blasting material is approximately few thousand cycles. Non-metallic blasting materials have substantially lower durability values. In Tab. 1 durability values, determined by four methods, of two types of non-metallic blasting materials with three various grain sizes, are given [6].

4. Conclusions

Blasting appears to be a suitable technology for the preparation of surface with desirable quality, including impurities removing, achievement of suitable microgeometry and physical – chemical surface properties.

To achieve a technically and economically advantageous use of blasting process, i.e. to achieve desirable surface quality at economically acceptable costs, the blasting process cannot be mechanically applied, but it is always necessary to find the most suitable technical parameters for this technology. This involves the use of new blasting parameters, the blasting parameters and blasting equipment. This is possible only if physical nature of the blasting process is fully understood.

The influence of the blasting process on the substrate can be separated into upgrading and degrading effects. However, since blasting process is a very complex one, no unanimous classification of various effects is possible. In many cases upgrading effects may be considered also as degrading effects. Character of these effects depends upon the aim and purpose of the surface pre-treatment.

Substrate degradation is characterized by surface and subsurface cracks formation, and is at least partially explained by delamination theory. During the blasting process the substrate surface morphology changes, a secondary surface pollution by embedded

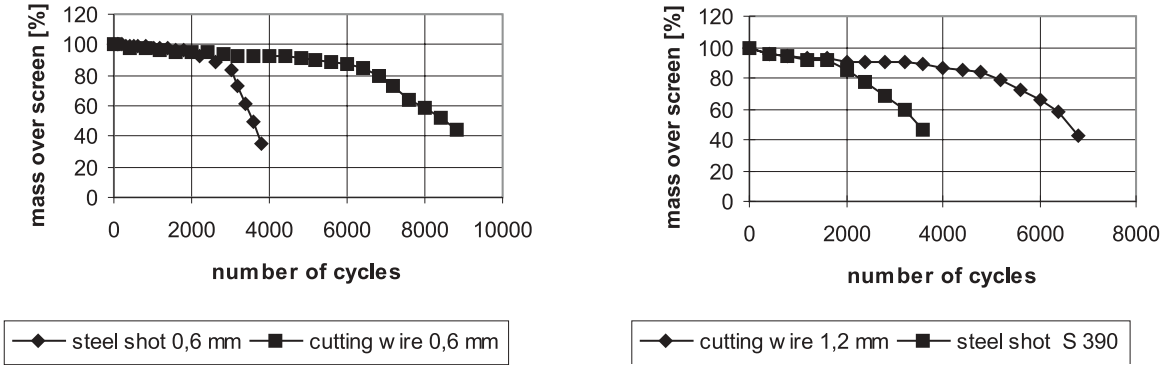

Fig. 8 Durability curves for steel shot and cut wire with grain size 0.6 mm a 1.2 mm [6]

Durability values of blasting materials determined by four methods of durability evaluation. Tab. 1

Blasting material	Method of durability evaluation.			
	k_{DTP} [–]	K_{50} [number of cycles]	Total wearing [number of cycles]	Ra – 15 % [number of cycles]
HK 0.56 mm	0.8	5.4	960.8	4.9
HK 0.35 mm	0.86	76.9	1591	0.5
HK 0.18 mm	0.93	5012.8	3315	0.72
GBM 0.56 mm	0.355	0.14	135.8	0.93
GBM 0.35 mm	0.69	2.29	135.8	1.1
GBM 0.18 mm	0.85	6.8	189.2	0.88

blasting material grains and free dust particles takes place, the surface activity rapidly decreases due to its reaction with the atmosphere together (which has negative impact on the adhesion of subsequently applied coatings), the materials are thermally loaded and undesirable substrate mass reduction also takes place.

Mutual interaction of blasting material with substrate involves complicated processes and mechanisms, leading to *blasting material degradation*. Wearing mechanisms of metal and non-metal blasting materials are different. Wear of *metallic blasting materials* is characterised by rounding, intensive flaking and grain breaking, slow wearing down to dust particle creation. Wear of *non-metallic blasting materials* is characterised mainly by crumbling, resulting from blasting material characteristics. Tougher and softer blasting materials are visibly deformed, hard and brittle materials crumbling and break upon their impact on the substrate.

Blasting material degradation is closely connected with its durability. Durability of blasting materials can be determined by several methods, based on evaluating the changes of various parameters of these materials. Selection of suitable method of durability evaluation depends on the specific application, for which the blasting process is optimised. Modified stylus profilometry makes it possible to obtain 3D views of surfaces blasted by blasting materials in different wearing state. These 3D view visually document the course of the substrate and blasting material wearing process.

This research was supported by grants VEGA No. 1/9388/02 and 1/9400/02.

References

[1] KNIEWALD, D. et al.: *Study of the blasting process as a substrate pretreatment with respect to subsequent coating process and formation of adhesive joints.* Grant research project VEGA No. 1/9388/2002.
[2] BAČOVÁ, V. et al.: *Investigation of the properties of plasma sprayed coatings with respect to thermal loads and tribogeneration changes.* Grant research project VEGA No. 1/9400/2002.
[3] KNIEWALD, D.: *Original knowledge in blasting process.* Habilitation thesis. Košice, TU SjF, 1994.
[4] BREZINOVÁ, J.: *The study of blasting process regularity from the aspect of degradation phenomena.* Academic dissertation. TU SjF Košice, 2003.
[5] TAKÁČ, K.: *Influence of blasting regime and structural changes on blasting media durability.* Academic dissertation. VŠT SjF Košice, 1969.
[6] GUZANOVÁ, A.: *New knowledge in blasting process with ecological blasting media application.* Academic dissertation. TU SjF Košice, 2003.

Gianni Nicoletto – Radomila Konečná *

CORRELATION OF FRACTURE SURFACE TOPOGRAPHY AND TRANSITION BEHAVIOR OF NODULAR CAST IRON

Dynamic testing methods, especially the Charpy V-notch testing at different temperatures, are commonly used to determine the impact response of metallic materials. However, in nodular cast iron this transition trend is characterized by scatter, which makes it difficult to precisely identify the influence of microstructural features on material response. In this paper the vertical surface roughness parameter R_V obtained from fracture profiles is considered on the hypothesis that the surface topography is a sensitive indicator of the energy absorbed by plastic deformation and of the microstructure. Nodular cast irons having a range of microstructures were impact tested and the surface roughness determined. Transition trends of impact toughness and of R_V are discussed.

1. Introduction

Nodular cast iron is preferred to grey cast iron in many engineering applications where high strength and high impact toughness are required, [1]. Previous studies, [2, 3], showed that ductile iron has a pronounced ductile-to-brittle transition i.e. the change in fracture response from ductile to brittle with an increase in test temperature. Most alloying elements or impurities affect toughness indirectly through their effect on graphite morphology and matrix microstructure. An increase in silicon and carbon content increases the number of crystallizing nuclei and, consequently, the number of graphite nodules with an increase in the transition temperature. The effect of graphite morphology is especially significant for upper-shelf toughness (ductile response) and very limited below the transition temperature, [4]. Addition of copper or tin favours the development of a pearlite matrix with an expected decrease in impact toughness.

Dynamic testing methods, especially the Charpy V-notch testing at different temperatures, are commonly used to identify the impact response of metallic materials. Test data associated to the transition behavior are normally presented in the form of *KCV* vs. *T* plot and are often characterized by a *S*-shaped trend. However, in nodular cast iron this transition trend is accompanied by scatter and the scatter increases with material heterogeneity as the notch selectively initiates failure at different microstructural locations. The data scatter makes it then difficult to precisely identify the influence of microstructural features, such as shape, size and number of graphite nodules or matrix structure (i.e. pearlite/ferrite ratio, for example) on material response.

The previous considerations suggest the importance of identifying and evaluating parameters, other than the absorbed impact energy, that could provide insight of the microstructural contribution to the material response. In this paper the vertical surface roughness parameter R_V of the fracture profile will be considered on the hypothesis that the surface topography is a sensitive indicator of both the energy absorbed by plastic deformation during an impact test and the material microstructure. Therefore notch and unnotched impact tests performed on different melts of nodular cast iron having a great range of microstructure are examined. Their transition behavior is also characterized by Charpy *V*-notch tests at different temperatures. The vertical surface roughness is then obtained from profiles of the failed specimens and assessed in its ability to discriminate the role of microstructural details on material response.

2. Experimental details

2.1 Materials and microstructure

Twelve melts of nodular cast irons were produced with the aim of obtaining a wide variety of microstructures, especially in terms of ferrite-to-pearlite ratio. Details of charge composition, type of modifier and inoculation of the ductile irons as well as the chemical composition of the melts are given elsewhere, [2]. The microstructures of the nodular cast iron were characterized according to the following parameters: percentage of perfectly round nodules, nodule count (number of nodules/mm^2) and percentage of effective ferrite phase in the matrix, see Tab. 1 (D identifies melts with FeSi addition and E with SiC addition). Basic mechanical properties, such as hardness, ultimate strength and elongation to rupture, are also given in Tab. 1.

2.2 Impact toughness testing

The Charpy *V*-notch dynamic test method is commonly used to identify the impact response of metallic materials. To deter-

* **Gianni Nicoletto[1], Radomila Konečná[2]**
[1]Dept. of Industrial Engineering, University of Parma, 43100 Parma, Italy, e-mail: nick@me.unipr.it,
[2]Dept. of Materials Engineering, Žilina University, 01026 Žilina, Slovakia, e-mail: radomila_konecna@kmi.utc.sk

Microstructure and mechanical properties of melts of nodular cast iron Table 1

Melt	Graphite form STN 42 0461	Matrix	Nodule count [mm^{-2}]	Effective ferrite [%]	HB	R_m [MPa]	A_5 [%]	KC0 [J/cm^2]	KCV [J/cm^2]
D 1756	80%VI5+20%V6	Fe 30	83	29.6	249	744	7	11	4.5
D 1579	70%VI5+30%V6	Fe 55	100	66.8	203	709	3	16	3.6
D 1248	90%VI6+10%V7	Fe 80	113	71.4	205	550	12	16	5.5
D 1674	70%VI6+30%V7	Fe 80	119	71.8	181	564	7	49	6.1
E 164	90%VI5+10%V6	Fe 30	92	21.2	201	774	8	14	3.7
E 158	70%VI5+30%V7	Fe 30	96	24.0	221	774	6	11	3.4
E 151	70%VI6+30%V6	Fe 55	117	49.8	216	564	12	6	5.6
E 148	80%VI6+20%V7	Fe 80	121	73.4	170	576	15	51	7.1
E 144	80%VI7+20%V7	Fe 80	131	75.6	174	537	16	69	6.3
E 152	90%VI7+10%V7	Fe 94	160	77.6	194	554	13	38	6.3
E 153	80%VI7+20%V7	Fe 94	174	80.2	178	530	13	90	5.2
E 171	90%VI7+10%V8	Fe 94	196	81.2	174	537	15	75	8.2

mine the transition behavior, Charpy V-notched specimens (prismatic bars 10 × 10 × 50 mm) are tested at different temperatures. In this study tests were performed at temperatures ranging from − 10 °C to 180 °C. The Charpy-notch impact toughness is defined as KCV (in J/cm^2). Following a norm suggesting the use of the same prismatic bar but without notch for the impact characterization of cast iron, extensive unnotched bar tests were also performed at room temperature. In this case the unnotch impact toughness is defined as KC0 (in J/cm^2). The experimental impact toughness data for the twelve melts of this study are presented in Tab. 1. Following impact testing, a thorough microfractographic investigation of the fracture surfaces was performed in the SEM to highlight the change in failure mechanisms due to the ductile-brittle transition behavior and was reported in [3].

2.3 Fracture surface roughness measurement

Nodular cast iron is relatively brittle, so limited energy is dissipated during crack propagation by impact. Following the hypothesis that fracture surface topography of impacted specimens is a sensitive indicator of both the energy absorbed by plastic deformation and of the material microstructure, the vertical surface roughness parameter R_V of the fracture profile was considered [5]. Fig. 1 shows typical micrographs of fracture profiles where dimples and extensive plastic deformation of ferrite when tested at high temperature and cleavage areas in ferrite when tested at low temperature are observed. Therefore, intuitively a high roughness is an indication of a significant contribution of ductile mechanisms.

The vertical surface roughness parameter R_V of the fracture surface was determined by analysis of the fracture profile, see Fig. 2. The R_V parameter (i.e. Behrens' roughness parameter) was quantitatively evaluated using the following relationship, [5],

$$R_V = \frac{y}{L'} \Sigma P_i$$

where P_i is the number of intersections of the magnified (250x) fracture profile with a superposed grid of horizontal lines, y is the spacing of these grid lines (i.e. y = 2 mm) and L' is the measurement base length (L' = 150 mm).

3. Results and discussion

3.1 Ductile-brittle transition behavior

In this section the role of ferrite in the matrix on the transition behavior of nodular cast iron is examined as obtained by Charpy *V*-notch impact tests at temperatures ranging from −10 °C to 180 °C. The response of essentially ferritic (Fe 94) nodular cast irons is shown in Fig. 3. The classical S-shaped trend signalling the transition behavior from ductile to brittle is observed with a change in KCV from 20 J/cm^2 down to 5 J/cm^2. The classical sigmoidal equation is best fitted to all the experimental results and a value of 70 °C is found for the transition temperature T0, defined as the temperature associated to the average of the two asymptotic *KCV* values. The scatter is relatively limited in this case.

Fig. 4 shows the transition curves for nodular cast iron having similar ferrite content (Fe 80) in the matrix but two different additions (i.e. SiC vs. FeSi) in the melt charge. In this case it is possible to discriminate two distinct transition curves although the scatter is larger than before. Furthermore, the SiC-added nodular cast iron presents a well-defined sigmoidal trend with two asymptotes and a transition temperature T0 of 85 °C. The FeSi-added nodular cast iron, on the other hand, shows a large scatter and an incomplete transition trend although a T0 of 108 °C can be esti-

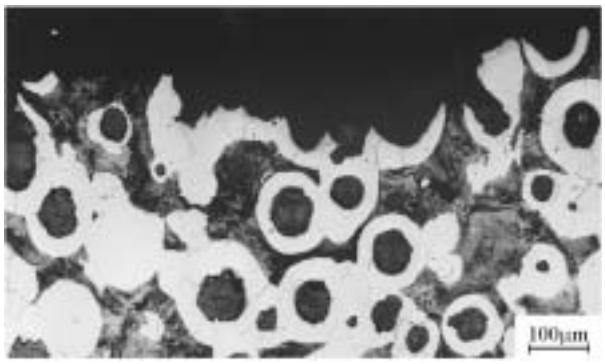

E 144, T = 140 °C, *KCV* = 15.4 J/cm^2

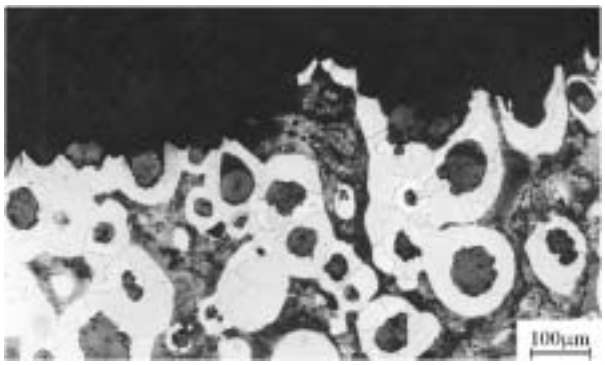

E 171, T = 100 °C, *KCV* = 14.6 J/cm^2

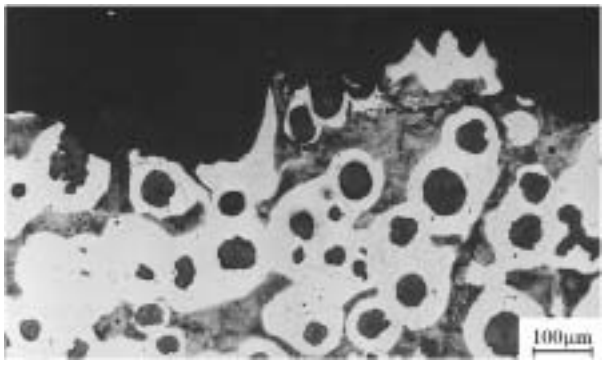

E 151, T = 60 °C, *KCV* = 8 J/cm^2

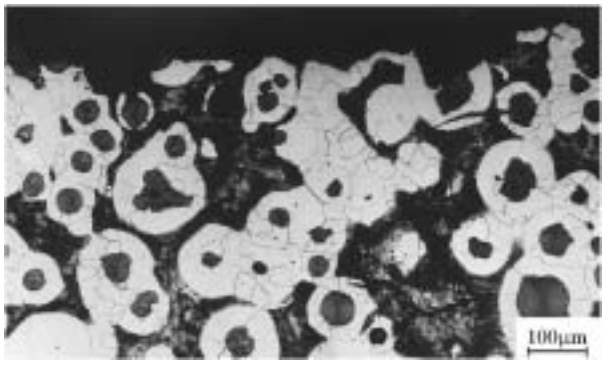

E 144, T = 20 °C, *KCV* =5 J/cm^2

Fig. 1. Typical sections of impacted test specimens (melt, test temperature and notch impact toughness are specified below each micrograph)

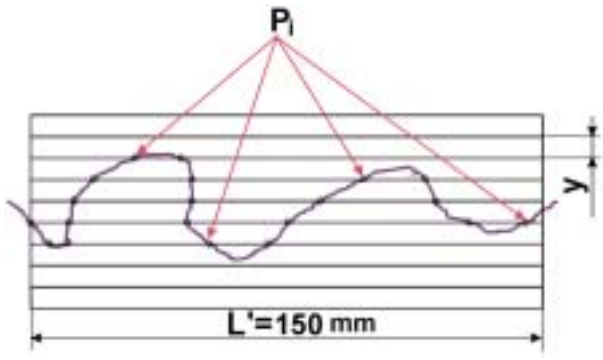

a)

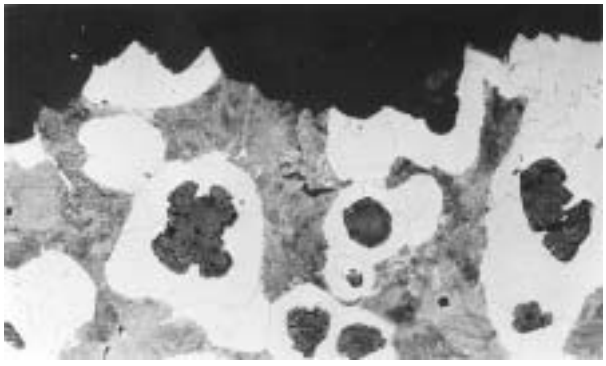

b)

Fig. 2. Method for the determination of R_V a) scheme and b) fracture profile

mated by best fit. To summarize this section, an increase in ferrite content in the matrix decreases the transition temperature. A SiC addition to the melt results in a higher upper-shelf toughness and a lower transition temperature when compared to nodular cast iron with a FeSi addition.

3.2 Notch vs. unnotched impact toughness

The role of the test methodology, (i.e. use of a V-notched or an unnotched prismatic bar) on the impact characterization of nodular cast iron is discussed in this section. A difference in the characterization capability of the two approaches (i.e. notched vs. unnotched) is expected since the notch concentrates high stresses only in a limited material volume at the crack tip and develops a triaxial stress state favoring a brittle material response. On the other hand, in the unnotched specimen a considerably larger material volume is subjected to high stresses while the stress triaxiality is low. The wide range of material microstructures characterizing the present melts of nodular cast iron provides experimental data that can be used in the assessment of the two impact test methods. Two microstructural characteristics, one related to the

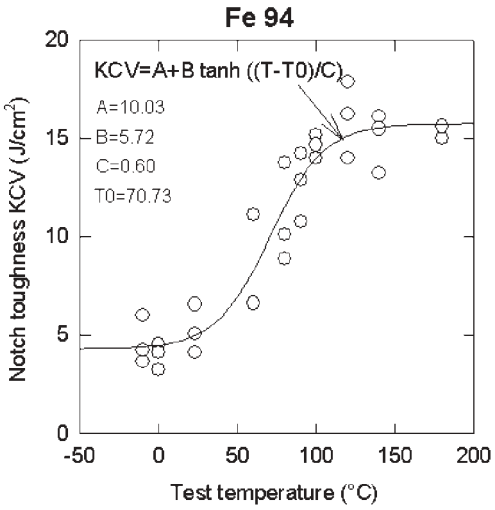

Fig. 3 Transition behavior of a nodular cast iron with Fe 94 matrix

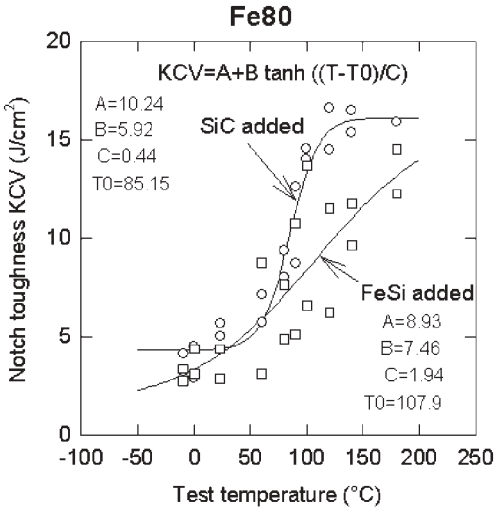

Fig. 4 Transition behavior of nodular cast irons with Fe 80 matrix

matrix and the other to the graphite nodules are separately considered in order to investigate their influence on the impact tests data. Therefore, notched and unnotched impact toughness at room temperature is plotted as a function of the ferrite content in the matrix in Fig. 5 and as a function of the graphite nodule count in Fig. 6.

The unnotched impact toughness test (i.e. KC0) shows the greatest sensitivity to the ferrite content. Fig. 5 shows also a steep gradient in the dependence on the ferrite content above 70 %. A 10 % increase in ferrite content is found to result in a dramatic increase, from 15 J/cm^2 to 80 J/cm^2, in KC0. The trend of the notched (i.e. *KCV*) data is less defined with a large scatter determined above 70 % of the ferrite content. As far as the dependence of KC0 and *KCV* on the graphite nodule count, see Fig. 6, both data sets show increasing impact toughness with nodule count but the scatter is quite significant in both cases. To summarize this

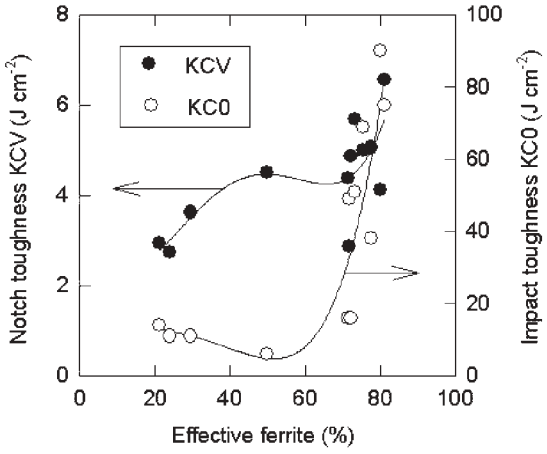

Fig. 5 Role of ferrite in the matrix on impact toughness at room temperature

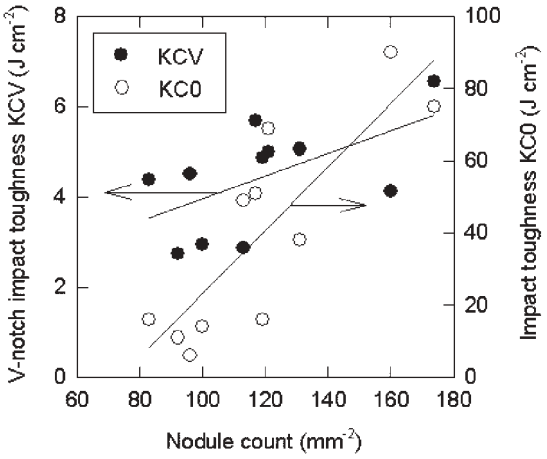

Fig. 6 Role of graphite nodule count on impact toughness at room temperature

section, it appears that the use of the unnotched specimen geometry for impact characterization of nodular cast iron provides a better resolution of material response than the Charpy notch test method.

3.3 Fracture surface roughness

In this section the capability of the surface topography in discriminating microstructure-dependent material behavior is investigated. Generally, the fracture roughness is directly influenced by the size and distribution of graphite. The presence of different fracture mechanisms, such as cavitations around nodules, dimple formation, cleavage of ferrite capsules and cleavage of pearlite regions, influence the degree of roughness of the surface.

In the previous section it was concluded that the use of unnotched specimen for impact characterization of nodular cast iron provides a better resolution of impact response of nodular

cast iron than the notched bar method. Initially, the KC0 data obtained by testing the present wide range of nodular cast iron at room temperature is plotted against the fracture surfaces roughness R_V. The remarkably linear correlation of Fig. 7 demonstrates a close dependence between the two parameters. To investigate this aspect, the fracture profiles obtained during the transition characterization testing of nodular cast iron were studied by optical microscopy and the fracture roughness determined.

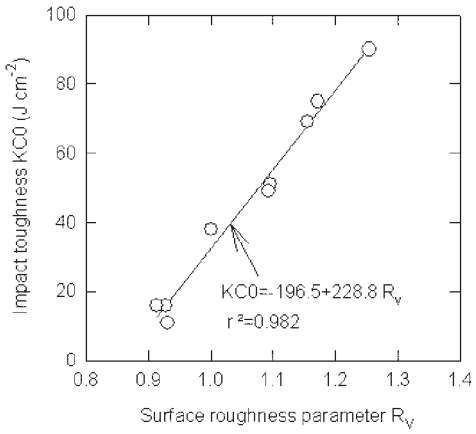

Fig. 7 Correlation of unnotched impact toughness and roughness of fracture profiles

The resulting trends in the vertical roughness parameter R_V characterization as a function of the test temperature are shown in Figs. 8 and 9. The nodular cast irons considered were characterized by a percentage of effective ferrite in the matrix of around 70 %, which should be associated to microstructural-induced scatter due to their heterogeneity. Vertical roughness R_V data are presented in separate plots on the basis of addition type. Inspection of Figs. 8 and 9 show that in all cases the vertical roughness R_V exhibits a "transition" trend although in a less pronounced way than the plots of the Charpy impact. This transition-type response is more pronounced in the SiC-added nodular cast iron, which also showed a well-defined transition behavior in the Charpy tests, Fig. 3 and 4. Fig. 8 confirms that, to completely determine the transition behavior of FeSi-added nodular cast iron, a wider range of test temperatures may be required.

Another interesting feature of the R_V vs. T plot is the distinct material response for the different microstructures. In the plots, each data set is associated to microstructural details such as nodule count and graphite form. Fig. 8 shows that in the presence of a similar nodule count of the FeSi-added melts, the quality of graphite nodules can significantly increase the surface topography and, indirectly, see Fig. 7, improve the impact performance. It is expected that this improvement would disappear within the scatter of the standard Charpy test method. Alternatively, Fig. 9 shows that in the presence of a similar quality of graphite nodules of the SiC-added melts, an increase in nodule count significantly reduces the surface topography especially at low temperatures. Again, the fracture surface topography could signal a reduced impact performance, possibly difficult to identify by the standard Charpy test method.

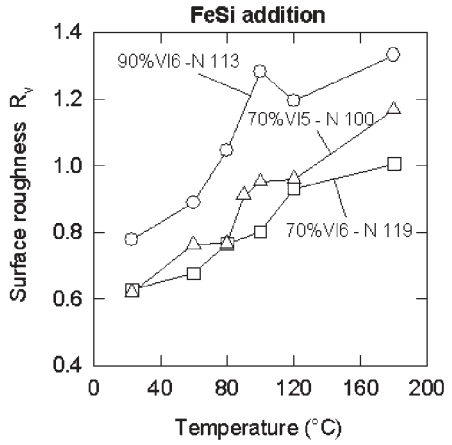

Fig. 8 Vertical surface roughness R_V dependence on impact test temperature for FeSi-added melts

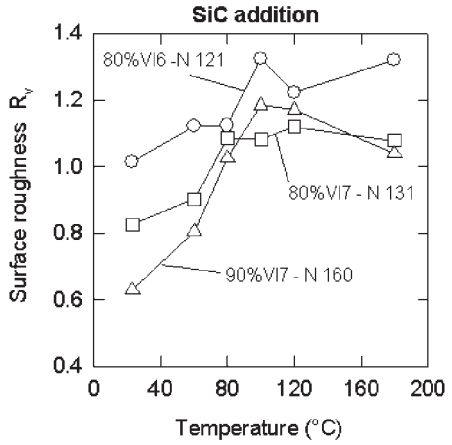

Fig. 9 Vertical surface roughness R_V dependence on impact test temperature for SiC-added melts

4. Conclusions

The aim of this study was to determine the transition response of nodular cast iron and to investigate the possibility of using fracture surface topography indicators to discriminate microstructure-related material response. Therefore, nodular cast irons with a wide range of microstructures were characterized and tested. The following conclusions are advanced:

- Nodular cast irons with a high percentage of ferrite showed the transition behaviour when Charpy *V*-notch tested at temperatures in the range from −10 °C to 180 °C.
- Nodule count and percentage of ferrite in the matrix significantly affect notch and unnotched impact toughness of nodular cast iron.

- The unnotched toughness KC0 test method is more sensitive and precise in describing the role of ferrite on the impact behavior of ductile iron when compared to the notch toughness *KCV* test method.
- The fracture surface roughness parameter R_V determined in impacted specimens defines trend similar to the ductile-to-brittle transition behavior.
- SiC addition to ductile iron results in a superior ductile-brittle transition behavior when compared to the FeSi addition.
- The role of microstructural parameters, such as quality of graphite nodule, nodule count and ferrite content in the matrix, on material performance can be discriminated using fracture surface roughness.

Acknowledgements

Financial support of the Scientific Grant Agency of Ministry of Education of Slovak Republic and Slovak Academy of Sciences (grant No.1/0027/03), of the SK/CZ Cooperation Project (No. 063/117) and of the CETRA program at University of Žilina, Slovakia.

References

[1] DAVIS, J. R. ED.: *ASM Specialty Handbook – Cast Irons*, ASM International, 1996.
[2] KONEČNÁ, R., HADZIMOVÁ, B., NICOLETTO, G., MATEJKA, M.: *Role of ferrite content on the impact strength of nodular cast irons.* Materials Engineering, 10, 2003, Žilina, ISSN 1335-0803.
[3] KONEČNÁ, R., NICOLETTO, G., HADZIMOVÁ, B., LEJČEK, P.: *Influence of temperature and micropurity of ferrite on failure behaviour of ductile iron.* In.: Fractography 2003, Stará Lesná, Slovakia, 2003, 224-232.
[4] KONEČNÁ, R., SKOČOVSKÝ, P.: *Relationship between microstructure and impact toughness of cast irons with transient forms of graphite.* Kovové materiály 3 – S, SAV, Bratislava, 1998, pp. 43 - 48.
[5] BENKO, P., SKOČOVSKÝ, P.: *Influence of modification on quantitative-microfractographic characteristics of silumin AlSi10MgMn (in Slovak).* Materials Engineering 2/1996, University of Žilina, 1996, pp. 64-72, ISSN 1335-0803.

Juraj Gerlici – Tomáš Lack – Marta Kadorová *

CALCULATION OF THE EQUIVALENT CONICITY FUNCTION OF THE RAILWAY WHEELSET TREAD PROFILE AT THE DELTA R FUNCTION WITH A NEGATIVE SLOPE

The rail-wheel interface is fundamental to explain the dynamic running behaviour of a railway vehicle. It must therefore be understood and among the parameters by which it is characterised, the one called "equivalent conicity" plays an essential role since it allows the satisfactory appreciation of the wheel-rail contact on tangent track and on large-radius curves.

By definition, the equivalent conicity is equal to the tangent of the cone angle tg γe of a wheelset with coned wheels whose lateral movement has the same kinematic wavelength as the given wheelset.

In order to be able to compare the results obtained by different railways, both as to the value of the equivalent conicity and as to the results where that parameter plays an important role, it is necessary for the equivalent conicity to be calculated according to the same principles.

Methods, which determine ways of the calculation, are mentioned in the UIC leaflet, but it does not define either limits of accepted values of the equivalent conicity or the shape profiles, thanks to which the conicity could be reached.

The equivalent conicity is calculated either by the application of the Klingel formula or with the help of the linear regression of the Δr function on the interval of the double amplitude of the wavelength of a periodical movement of the middle of a wheelset. The process of the calculation in the leaflet is determined for a standard case of the Δr function shape, which crosses the y-axis in one point in the graph of dependence of the Δr function on the lateral displacement. In practice there are cases when the Δr function crosses the y-axis in more than one point.

The paper deals with the possibility of the calculation of the equivalent conicity with the help of the Klingel formula in the case when Δr function crosses the y-axis in three points.

The leaflet describes such a case as a Δr function course with a negative slope. In this case not one, but three curves will be the results. Each of them will determine an equivalent conicity for another interval of validity (amplitude of oscillation of the middle of the wheelset). According to the initial conditions (amplitude of oscillation and position of the wheelset on the rail), the wheelset can have for some amplitudes two possible trajectories or none in the case of a negative conicity.

1. Introduction

Forces, thanks to which the wheelset comes back to a centred position, act on the railway wheelset after the deflection of its middle from the railway axis in the lateral direction. The wheelset performs at the same time a forward movement in the track direction. The result of the simultaneous movement, both in the progressive direction and in the lateral direction, is a theoretically regular wavy movement of the wheelset which is represented by its centre.

The conicity of tread profiles of railway wheels is the reason why the wheelset has a tendency to come back in the lateral direction from maximum deviations into the middle of a track. This happens when driving even after a lateral deviation from the centred position against the rail axis. It is important to determinate courses of geometrical characteristics of profile contacts of a railway wheel and a rail for the evaluation of the tendency rate.

2. Geometrical characteristics

Geometrical characteristics of a wheel and a rail contact are the following [2, 3]:

Contact points determine the position of contact points at the lateral displacement of the wheel profile on the rail profile.

Delta -r (Δr function) is a difference between of an instant diameter of running of one wheel of a wheelset and instant diameter of running of other wheel of a wheelset at the lateral movement of a wheelset on a track.

Tangent Gamma function is a difference between the value of the normal line tangent angle of the tangential contact area in the contact point and vertical axes of a track. It determines the rate of binding intensity, which comes back the wheelset after its lateral deviation into a centred equilibrium position on the track.

* **Juraj Gerlici1, Tomáš Lack1, Marta Kadorová2**
[1]Faculty of Mechanical Engineering, Department of Railway Vehicles, Engines and Lifting Equipment. University of Žilina, Veľký diel
[2]Faculty of Science, Department of English Language and Literature. University of Žilina, Hurbanova 15 SK-01026 Žilina.
E-mail: juraj_gerlici@kkvmz.utc.sk, tomas_lack@kkvmz.utc.sk, marta.kadorova@fpv.utc.sk

Effective conicity is a reference conicity only of a cone profile of a wheel of a wheelset which the wheelset should possess to perform the same rotational movement without slips on the track as the real (measured) wheelset.

Equivalent conicity is a reference conicity which equals the curving profile of a wheel when taking into consideration the wavelength and amplitude of a coned wheel movement.

The angle of attack and the angle of tilt of the wheelset, which originated by a different instant diameter of rolling, influences the size and shape of geometrical characteristics.

In the following text, let us suppose that the wheelset moves on the track under the angle of attack which equals zero grade and we will not take into consideration the influence of the angle of tilt on the shape of geometrical characteristics. Each of the above mentioned geometrical characteristics shows a measure of other condition of the geometrical contact, the position of contact points and the Δr function shape are the basis for the determination of other characteristics. The article concentrates on the determination of the equivalent conicity function. The methods of the calculation of the equivalent conicity function are determined by the UIC leaflet [1]. The basic procedure of the calculation of the equivalent conicity presupposes a standard shape of the Δr function course which crosses the horizontal axis in one point.

When there are wheel profiles with modified geometry, for example by wearing of the wheel tread, it can happen that the Δr function crosses the horizontal axis in three points. The leaflet describes this case as a characteristic with a negative slope and from the point of view of the solution procedure it enables a certain variability.

3. Equivalent conicity

By definition, the equivalent conicity is equal to the tangent of the cone angle tg γ_e of a wheelset with coned wheels whose lateral movement has the same kinematic wavelength as the given wheelset (on tangent track and on large-curve radius curves) [1].

If a coned tread profile of a wheel is used, and we do not take into consideration the slip between a wheel and a rail, the shape of the wave will have periodical oscillating course.

If we know the wheel diameters and the track gauge (distance of contact points), it is possible to state at the periodical oscillating movement the following [4]:

The wavelength does not depend on the amplitude and it is set only by the conicity of the tread profile of a wheel. The maximum amplitude is defined only by initial conditions.

Supposing that there is no slip between a wheel and a track, maximum amplitudes of waves following each other do not change.

In reality forces act on the wheelset moving on a track. The forces will lead to certain slips between the wheel and the rail they are determined by the relation friction – adhesion coefficient.

As a result of this influence, the amplitudes of waves following each other change in this way:

- the amplitudes of the waves decrease → the wheelset moves "in a stable way"
- the amplitudes of the waves increase → the wheelset moves "in an instable way",
- the amplitudes of the waves do not change → the wheelset moves in limits – cycles.

Determining the equivalent conicity course

The equivalent conicity is found by a *two-step computation* as follows [1]:

1. Integration of the differential equation

$$\frac{d^2y}{dx^2} + \frac{\Delta r}{2 \cdot s \cdot r_0} = 0 \qquad (1)$$

using the previously set characteristic $\Delta r = f(y)$ together with the following conditions:

$$y = y_0 \text{ for } x = 0 \qquad (2)$$

$$\frac{dy}{\partial x} = 0 \text{ for } x = 0 \qquad (3)$$

where: x displacement of the wheelset of the longitudinal direction of the track
y displacement of the wheelset of the lateral direction of the track
s half taping line distance
r_0 radius of the wheels when the wheelset is centred on the track
Δr difference of the rolling radius between right hand and left hand wheels.

The integration, based on the initial amplitude y_0, leads to the periodical movement of the wheelset with an amplitude (between two peaks) with the size $2\hat{y}$ and wavelength λ.

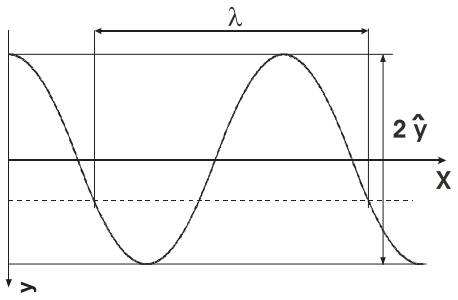

Fig. 1 y = F(x) function

2. Calculation of the conicity

From the actual movement of the wheelset the conicity is computed for the amplitude $\hat{y}$ either by applying the Klingel formula

$$tg\gamma_e = \left(\frac{\pi}{\lambda}\right)^2 \cdot 4 \cdot r_0 \cdot s \tag{4}$$

where $tg\gamma_e$ equivalent conicity
λ wavelength
$\hat{y}$ wave amplitude

or by applying a least squares type linear regression to the portion of the $\Delta r = f(y)$ characteristic within the $\hat{y}$ interval. The slope of this regression is equal to $2 \cdot tg\gamma_e$.

The procedure of the calculation of the equivalent conicity function course differs from the point of view of number of intersections of the Delta *r* function y-axis course. For practical usage that is for the equivalent conicity determination, the method of the Klingel formula application was used.

The wheelset's movement on the track can be formalised on the basis of the angle of attack Ψ.

$$\Psi = \frac{\dot{y}}{\dot{x}} = \frac{dy}{dx} \tag{5}$$

$d\Psi$ increment of the angle of attack
ds length of the track arc which equals the size of the angle $d\Psi$
R local radius of the wheel path

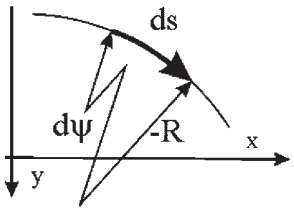

Fig. 2 Track increment

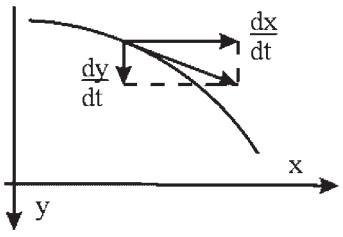

Fig. 3 Velocity vector and its components

$$ds = -R \,.\, d\Psi \tag{6}$$

for small angles Ψ, $ds \cong dx$

$$dx = -R\, d\Psi \tag{7}$$

and taking into account (1), this yields

$$\Psi = \frac{dy}{dx} = -\frac{dy}{Rd\Psi}\text{, hence } \Psi d\,\Psi = -\frac{dy}{R} \tag{8}$$

$$\frac{R}{2 \cdot s} = \frac{\frac{r_1 + r_2}{2}}{r_1 - r_2} \tag{9}$$

where r_1 right wheel diameter
r_2 left wheel diameter

$$r_0 = \frac{r_1 + r_2}{2} \tag{10}$$

where r_0 nominal radius of each wheel at centred position of wheelset in a track
$r_1 - r_2 = \Delta r$ Δr (Delta-r)
$2 \cdot s$ taping line distance

Thus:

$$R = \frac{r_0 \cdot 2 \cdot s}{\Delta r} \tag{11}$$

And by replacing R in (8), we get

$$\Psi d\Psi = \frac{-\Delta r \cdot dy}{r_0 \cdot 2 \cdot s} \tag{12}$$

giving, by integration,

$$\frac{\Psi^2}{2} = \frac{1}{2 \cdot s \cdot r_0}\left[\int \Delta r dy + C\right] \tag{13}$$

This integration serves to obtain the movement of the wheelset on the track and, in particular, the path corresponding to half of the wavelength starting from y_{emin} (for which $\Psi_{emin} = 0$) and going up to y_{emax} (for which $\Psi_{emax} = 0$).

The integral $\int \Delta r \cdot dy$ need only be calculated once for sufficiently large amplitudes to be able to cover the domain that will be needed for further assessment.

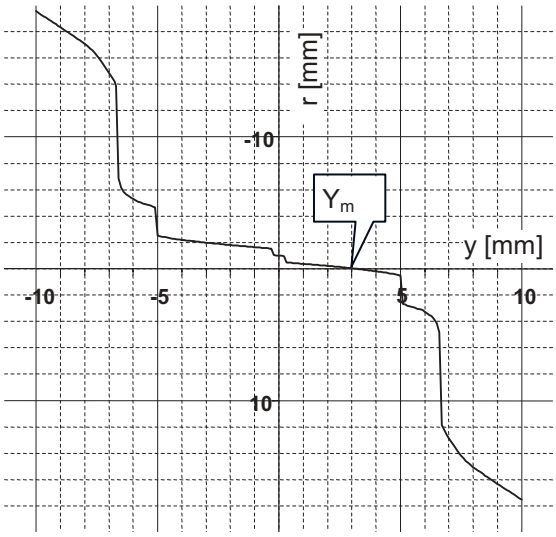

Fig. 4 Δr function with one intersection of y-axis

The wheelset's movement on the track is then obtained with the help of the following integration:

$$dx = \frac{1}{\Psi}\,dy \quad \text{or} \quad x = \int \frac{dy}{\Psi} \tag{14}$$

The procedure of the solution will be chosen on the base of *y*-axis intersections number.

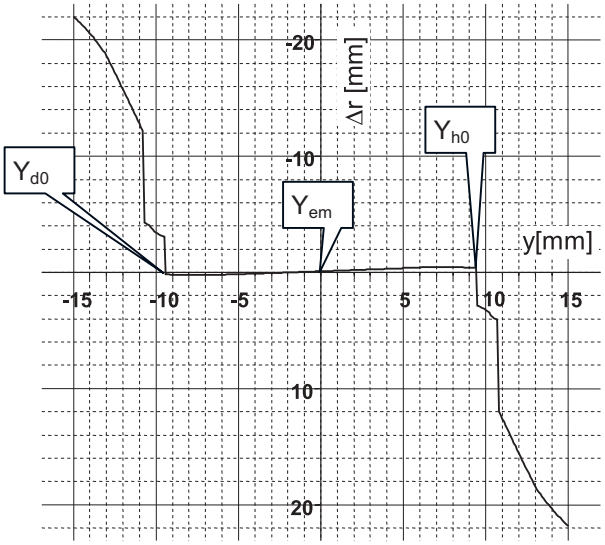

Fig. 5 Δr function with three intersections of y-axis

3. Δr function with one intersection of the y-axis

In practice the method of the Klingel formula application for one intersection of the y-axis is used in the following way.

1. Based on the function $\Delta r = r_1 - r_2 = f(y)$, find the value of Yem that corresponds to $\Delta r = 0$. (The example of Δr function with one intersection is in Fig. 4).

2. Calculate the function $S(y) = \int \Delta r \cdot dy$, starting from $y_{em} = Y_{em}$ in steps of $dy = +0.1$ mm to y and from $y_{em} = Y_{em}$ in steps of $dy = -0.1$ mm do $-y$.

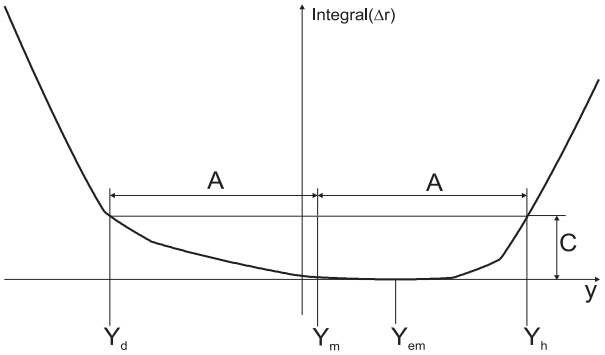

Fig. 6 Graph of the integral Δr function with one y- axis intersection

3. Determine the corresponding amplitudes $y_{emin} = Y_d$ a $y_{emax} = Y_h$ and calculate the mean lateral movement $\hat{y} = Y_m$.
4. Find the functions $y_{emin} = f(\hat{y})$ a $y_{emax} = f(\hat{y})$ which allow to determine, for given lateral movement of the wheelset $2\hat{y} = 2A$, corresponding minimum and maximum amplitudes y_{emin} and y_{emax}.
5. Compute the equivalent conicity $tg\gamma_e$ for a given movement $\hat{y} = A$: find the constant C of equation (13), such Ψ_{emin} for the corresponding y_{emin}, calculate the angle of attack Ψ by integrating equation (12) to give

$$\Psi = \sqrt{\frac{-1}{r_0 \cdot s}\left[\int \Delta r \cdot dy + C\right]} \tag{15}$$

In steps of $dy = 0.1$ mm.

Calculate the abscissa of the wheelset movement $x = f(y) = \int \frac{dy}{\Psi}$ between y_{emin} and y_{emax}, which allows to find the wavelength λ of the wheelset's kinematic motion.

In most cases the integration cannot be done in only one step in the range from y_{emin} to y_{emax}.

Therefore the wavelength x must be calculated by adding up, $dy = \frac{dy}{\Psi}$ whereby the step of dy should be lower than 0.1 mm.

Calculate the equivalent conicity, applying the Klingel formula.

$$tg\gamma_e = \left(\frac{\pi}{\lambda}\right)^2 \cdot 4r_0 \cdot s \tag{16}$$

6. Determine the function $tg\gamma_e = f(\hat{y})$ by applying Step 5. For $\hat{y}$ amplitudes starting up to the maximum permitted by the $\Delta r = f(y)$ characteristic, with a maximum step $\hat{y} = 0.5$mm.

4. Δr function with three intersections of the y-axis (with a negative slope)

In practice there are cases when Δr function crosses the y-axis in more than one point. (Fig. 5). The presentation of profiles shape and the distribution of contact points is in Fig.7. In this case, the wheelset according to initial conditions oscillates around one of the positions. There are three curves which describe the situation in the graph in Fig. 11.

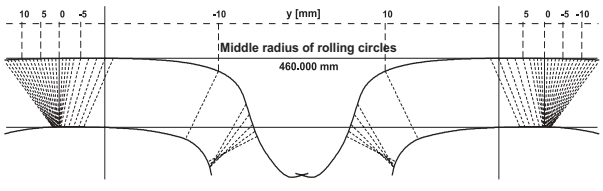

Fig. 7 Profiles shape and contact points distribution

When there are three intersections of the y axis, the graph of the Δr functions has a shape, which is shown in Fig. 8. Instead of a simple shape of the integral solution (around one intersection Y_m, Fig. 6), the geometrical shape of the integral solution consists of calculations around the first and third intersections of the Δr function through the y-axis.

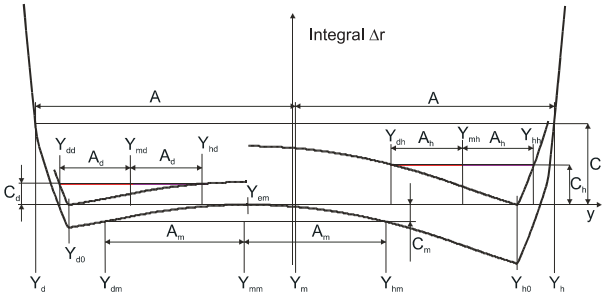

Fig. 8 Graph of the Δr integrals with three y- axis intersections

5. Calculation of Δr function integrals

When $\Delta r = f(y)$ characteristic has three intersections of the y-axis (defined as a characteristic having a negative slope), a slightly different procedure of equivalent conicity calculation is necessary.

Analysis of the Δr function shape,
- number of y-axis intersections,
- setting of the Y_{em} value,
- when there are three intersections setting of the Y_{d0} and Y_{h0} values as well,
- calculation of the curve of the Δr function integral,
- calculation of the integral on the left from Y_{em},
- calculation of the integral on the right from Y_{em},
- when there are three intersections of the y-axis,
  - calculation of the integral on the left from Y_{d0},
  - calculation of the integral on the right from Y_{d0},
  - calculation of the integral on the left from Y_{h0},
  - calculation of the integral on the right from Y_{h0}.

When the integrals for separate Y are calculated it is possible to gain other variables.

Calculation of the equivalent conicity course and mean value.

$$r = \frac{r_1 + r_2}{2} \tag{17}$$

where: r_1 right wheel radius
r_2 left wheel radius
r mean diameter of the wheels of the wheelset

6. For oscillation around Y_{em}

From $y_0 = y_{0\,min}$ to $y_{0\,max}$ with the step Δy_0

1. Determination of the C, Y_d, Y_h, Y_m constants for the y_0 amplitude under the condition $Abs(y_0 - A) < 1.10^{-4}$

   For the angle of wheelset yawing (angle of attack)

$$\psi = \sqrt{\frac{C - [\int \Delta r](y)}{s \cdot r}} \tag{18}$$

2. Determination of the function course.

$$\frac{1}{\psi} = f(y) \tag{19}$$

3. Determination of the mean value of the function $\frac{1}{\psi}$

$$\overline{\left(\frac{1}{\psi}\right)} = \frac{\int_{y_d}^{y_h} \frac{1}{\psi}}{2 \cdot y_0} \tag{20}$$

   Or for a negative conicity

$$\overline{\left(\frac{1}{\psi}\right)} = \frac{\int_{y_{dm}}^{y_{hm}} \frac{1}{\psi}}{2 \cdot y_0} \tag{21}$$

4. Determination of the wavelehgth of the wheelset movement

$$\lambda_0 = 4 \cdot \overline{\left(\frac{1}{\psi}\right)} \cdot y_0 \tag{22}$$

5. λ = calculation of the wheelset movement (s, r_1, r_2, Δr, y_0, y_m, λ_0)

   If $\lambda > 0$, $Y_m[y_0] = y_m$

$$K[y_0] = \left(\frac{2 \cdot \pi}{\lambda}\right)^2 \cdot s \cdot r \tag{23}$$

When there are three intersections of the Δr function with y-axis

λ = Calculation of the wheelset movement ($-s$, r_1, r_2, Δr, y_0, y_m, $-\lambda_0$)

If $\lambda > 0$, $Y_m[y_0] = y_m$

$$K[y_0] = \left(\frac{2 \cdot \pi}{\lambda}\right)^2 \cdot s \cdot r \tag{24}$$

- *When there are three intersections of the y-axis, for the oscillation around Y_{d0} and Y_{h0} the calculation is done in the same way as for the oscillation around Y_{em} except for the negative conicity.*

7. Presentation of the calculation results

K vector of the equivalent conicity
Y_m vector of the mean value
K_d vector of the equivalent conicity for the oscillation around Y_{d0}
Y_{md} vector of mean value for the oscillation around Y_{d0}
K_h vector of the equivalent conicity for the oscillation around Y_{h0}
Y_{mh} vector of mean value for the oscillation around Y_{h0}

One curve of the dependence on the amplitude of the lateral movement represents the graph of the equivalent conicity. The position of the axis around which the middle of the wheelset oscil-

lates (Y_m) is unambiguously changed according to size of the amplitude. (Fig. 9)

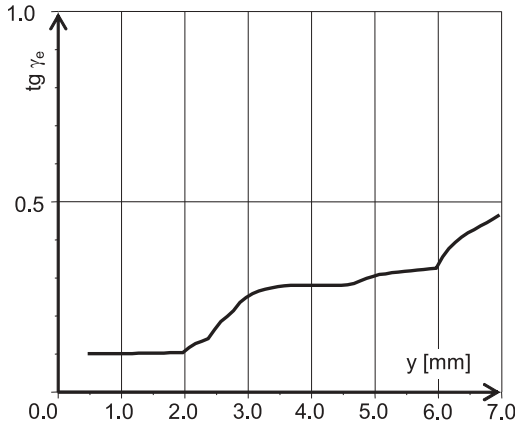

Fig. 8 Graph of equivalent conicity of the Δr function with one y- axis intersection

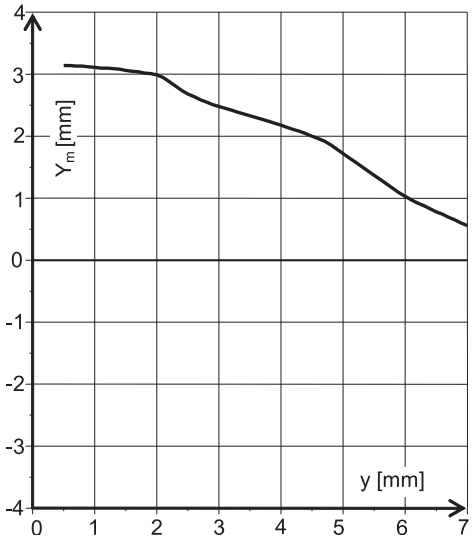

Fig. 9 Graph of mean Ym for Δr function with one y- axis intersection

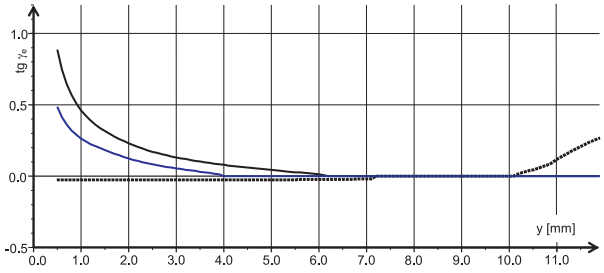

Fig. 10 Graph of the equivalent conicity function for Δr function with three y- axis intersections

It is possible to determine the equivalent conicity (Fig. 10) from several curves as a result of the Δr function integral shape. Two curves above the zero axis equal two possible periodical movements. The curve below the axis represents a theoretically non-stable area which equals the equivalent conicity non-leading to periodical movement.

The oscillation of the wheelset in the frame of amplitudes of approx. 6–10 mm is excluded in this specific case. When the amplitudes are smaller, it oscillates according to some of two local oscillation axes (Fig. 12) or when the amplitude is about 10.3 mm it oscillates only in one possible way (the third "middle" intersection $\Delta r \sim Y_{em}$) (Fig. 14.)

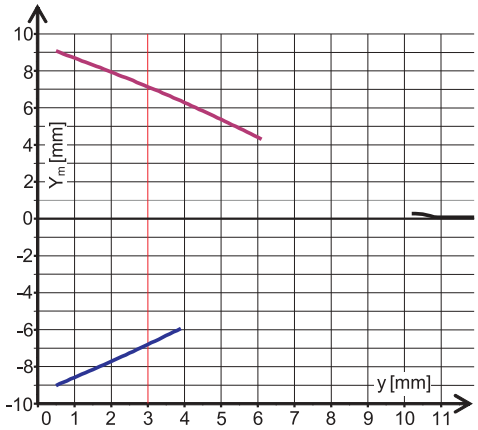

Fig. 11 Graph of mean Y_m (Y_{md}, Y_{mh}) for Δr function with three y- axis intersections

The shape of the trajectory of the wheelset centre arises from the size of the amplitude and from the position around which the wheelset centre oscillates. Both possibilities of the path of the wheelset centre for the amplitude of 3 mm are in Fig. 12.

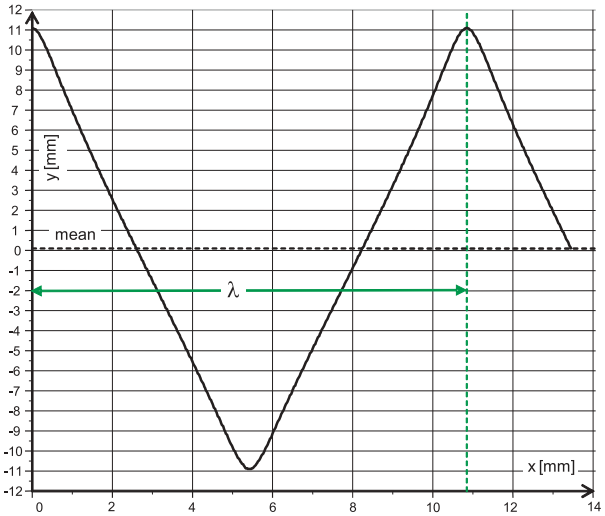

Fig. 14 Movement of a wheelset for the Δr function with three y- axis int. and y_0 = 11 mm

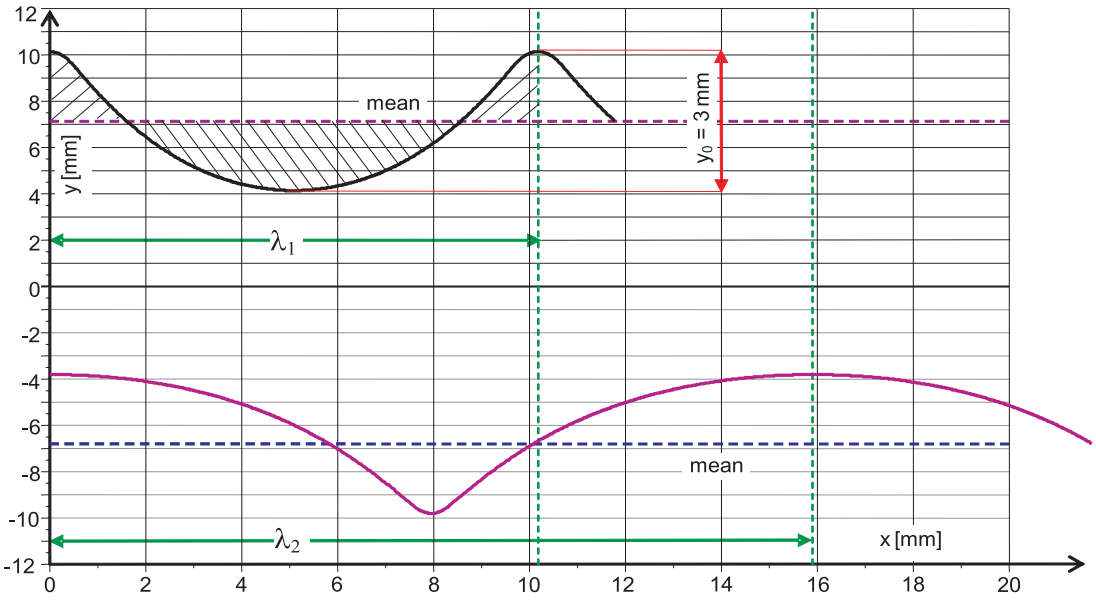

Fig. 12 Movement of a wheelset for the Δr function with three y- axis int. and y_0 = 3 mm

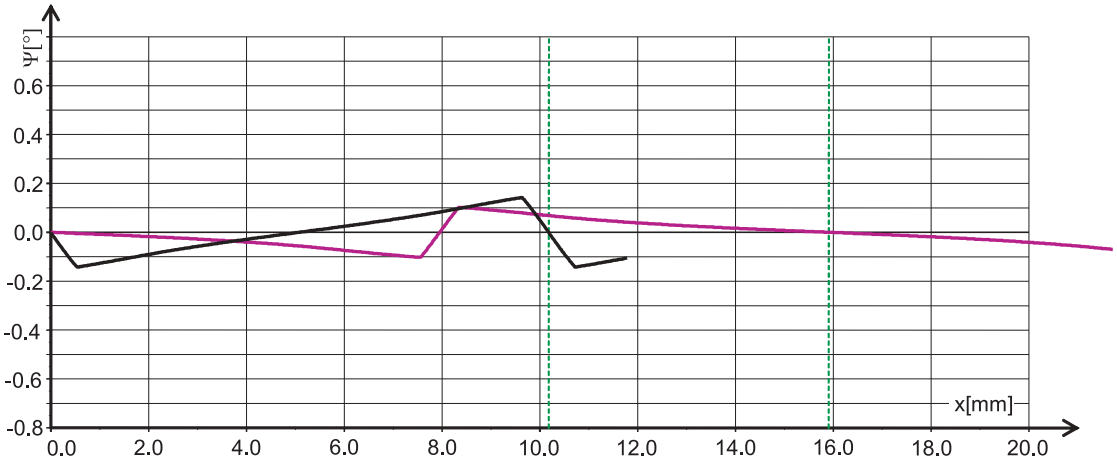

Fig. 13 Turning of a wheelset for the Δr function with three y- axis intersects and y_0 = 3 mm

The turning of the wheelset (angle of attack) in degrees at the periodical movement of the wheelset centre with the amplitude of 3-mm is shown in Fig. 13. Two curves build the graph, each of the curves is valid for other position of the centre around which the wheelset oscillates.

There is only one trajectory of the potential movement of the wheelset centre for the amplitude of 11-mm in Fig. 15.

The course of the wheelset yawing (angle of attack) in degrees at the periodical movement of the wheelset centre with the amplitude of 11 mm (shown in Fig. 15) is only one curve. The curve course of the wheelset yawing is closely connected with the shape of the Δr functions integrals.

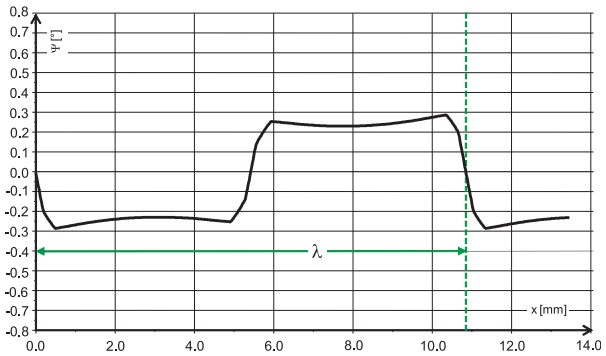

Fig. 15 Turning of a wheelset for the Δr function with three y- axis int. and y_0 = 11 mm

7. Conclusion

When evaluating the equivalent conicity and other geometric characteristics of the wheelset, it is necessary to take into account real shapes of the rails and wheel treads of both the wheels of the wheelset together with radii of the wheels.

In some cases the difference of the radii of the rolling of the wheels (Δr-function) obtains a negative slope. The fact will be realised in more than one intersection of the delta r function of the y -axis in the graph $\Delta r = f(y)$. The rolling radius of the wheel approaching the rail is decreasing this time while the radius of the drawing apart wheels from the rail is increasing.

The result of this geometric characteristic is that the wheelset can move in a wavy movement not around one but around more different positions. When the amplitudes are relatively small, it oscillates around one of two possible positions and it starts to oscillate only around one position only when it exceeds the limit value of the amplitude. The change is jumping, at a certain interval of amplitudes the wheelset cannot oscillate.

As the evaluation of the equivalent conicity is based on the analysis of the wavy movement of the wheelset on the track, we achieve three different courses of the equivalent conicity functions. The fact requests a special procedure of the evaluation of the equivalent conicity which is mentioned in the paper together with application examples.

References

[1] UIC Code 519: *Method for determining the equivalent conicity.* Draft of January 2003 Original version, 2003.
[2] GERLICI, J., LACK, T.: *Rail geometry analysis – from the point of view of wearing in the operation* (in Slovak). Komunikácie – ved. listy Žilinskej univerzity, EDIS ŽU Žilina, 2003.
[3] GERLICI, J., LACK, T.: *Railway wheel and rail geometry influence on ride properties of the vehicle* (In Slovak). In: 16. International Conference PRORAIL 2003, Žilinská univerzita, EDIS, Žilina 2003.
[4] IZER, J.: *The effective and equivalent conicity of railway wheelset tread profile* (in Czech). In: PRORAIL'95, Vysoká škola dopravy a spojov Žilina, EDIS, 1995.

Edward Hutnik – Andrzej Surowiecki *

DESIGNING OF RETAINING STRUCTURES OF REINFORCED SOIL WITH LIMIT CONDITIONS METHOD

The principles of limit conditions method in designing modern retaining structures of reinforced soil are presented. The principles are elaborated according to French Standard NF P 94-200 [1, 3]. Procedures of checking of particular kinds of stability are described. The most frequently adopted combinations of loads are given together with partial factors of safety of external, internal and general stability, method factors, friction factors of soil medium-reinforcement and values of partial safety factors of settlement.

1. Initial remarks

Dimensioning of retaining structures of reinforced soil elaborated by authors of this technology consists in the checking of internal and external stability [2, 5, 6], applying safety factors of pretty high values (1,5–3,15). The Standard [4] in which one of the chapters concerns dimensioning of retaining walls of reinforced soil, according to F. Schlosser [2, 5, 6] is binding in Poland. The Standard also gives principles of approximate adoption of the active zone, which is important for design economy. Modern structures of reinforced soil should be designed with limit conditions method according to the new French Standard NFP 94-200 [1, 3]. This Standard requires control of three types of stability of reinforced soil mass:

- external (because of slide along the base and bearing capacity of the ground),
- internal (because of value of the forces stretching reinforcement and anchoring bars in the soil),
- general, because of the possibility of slides along potential soil destruction surfaces due to cutting down.

The calculation scheme of reinforced soil structure is shown in Fig. 1 [1].

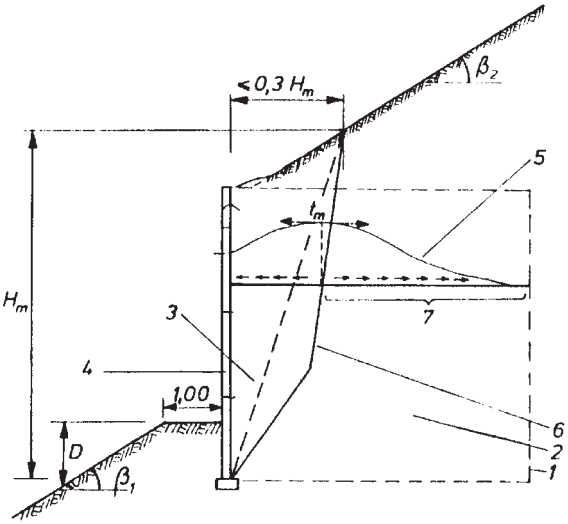

Fig.1. Calculation scheme of reinforced soil structure (according to [1, 3]): 1 – reinforced soil mass, 2 – bars anchoring zone, 3 – reinforced soil active zone, 4 – structure head lining, 5 – values of reinforcement element stretching, 6 – distribution of values of stretching along reinforcement, 7 – maximal stretching line, 8 – bar anchoring section

2. External stability

The structure is treated as uniform mass loaded with internal and external forces. Mass deadweight and water uplift pressure (when structure might be or is inundated with water) are internal loads. External loads include: thrust of backfill kept in balance by the reinforced mass as well as permanent and variable loads influencing the mass surcharge or its close proximity and passive earth pressure forces. The value of backfill thrust on the reinforced soil structure is calculated with conventional formulas (e.g. Coulomb's) assuming that the thrust influences theoretical surface located parallel to the structure lining, along the ends of longest reinforcement elements (Fig. 2). The tables of the NFP 94-200 [1, 3] standard include the most probable combinations of loads which are taken into account while checking external stability of the reinforced soil structure as well as partial safety factors γ_m.

Stability of the structure with regard to slide along the base will be ensured after fulfilling the following conditions:

$$R_h\ \gamma_{F3} \leq (R_v\ tg\varphi_{1k}/\gamma_{m\varphi} + L_{c1k}/\gamma_c) \tag{1}$$

and

$$R_h\ \gamma_{F3} \leq (R_v\ tg\varphi_{fk}/\gamma_{m\varphi} + L_{cfk}/\gamma_c) \tag{2}$$

* **Edward Hutnik[1], Andrzej Surowiecki[2]**
[1]Agricultural University in Wrocław, Institute of Building Engineering and Landscape Architecture, E-mail: hutnik@ozi.ar.wro.pl
[2]Wrocław Technical University, Institute of Civil Engineering; Agricultural Academy in Wrocław, Institute of Building Engineering and Landscape Architecture, E-mail: suran@poczta.pl

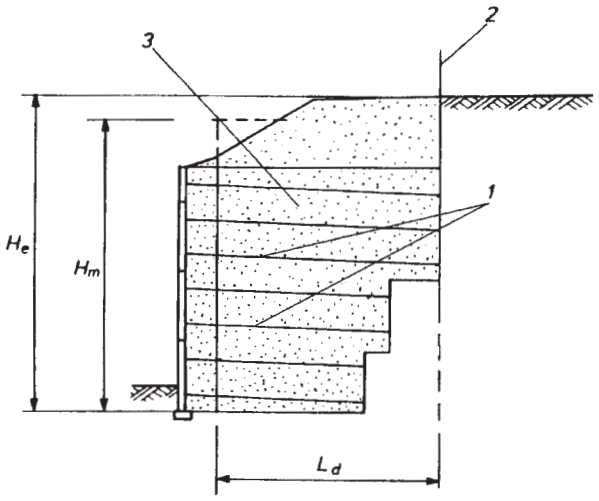

Fig. 2. Calculation scheme of soil backfill thrust [1, 3]: 1 – actual ends of reinforcement layers; 2 – line of reinforcement ends determining theoretical influence of the structure backfill thrust; 3 – zone of the internal active horizontal thrust

where:

R_h, R_v – horizontal and vertical components of the resultant load in the base of reinforced soil structure, neglecting method factor γ_{F3} [kN/m along the lining],

φ_{1k}, c_{1k} – characteristic values of the internal friction angle and soil cohesion in the reinforced mass [degrees; kPa],

φ_{fk}, c_{fk} – characteristic values of internal friction angle and subsoil soil cohesion [as above],

L – length of soil reinforcement layers (in structure with rectangular section), [m],

γ_{F3} – method factor,

$\gamma_{m\varphi}$ – partial safety factor applied to the tangent of internal friction angle; in case of standard load combination is 1.20; in case of exceptional combination is 1.10;

γ_{mc} – partial safety factor applied to the effective cohesion; in case of standard load combination is 1.65; in case of exceptional combination 1.50.

Soil resistance parameters corresponding to the effective parameters are determined from samples concentrated up to 95–100 % (according to Proctor's standard optimum). When there are no study results, A. Jarominiak [1] recommends adoption – for the reinforced mass, not inundated with water: $\varphi_{1k} = 360$, $c_{1k} = 0$, $\gamma_{1kmin} = 18$ kN/m^3, $\gamma_{1kmax} = 20$ kN/m^3; γ_{1kmin}, γ_{1kmax} – minimal and maximal characteristic density of the reinforced mass.

Checking with regard to subsoil bearing capacity means fulfilling the following inequality:

$$q_{ref} \leq q_{fu} / \gamma_{mq} \qquad (3)$$

where:

q_{fu} – subsoil limit bearing capacity [kPa],

γ_{mq} – partial safety factor of the reinforced mass subsoil bearing capacity, assumed as 1.50,

$q_{ref} = \gamma_{F3}\, R_v / (L - 2M_b/R_v)$ – subsoil load with reinforced soil mass [kPa].

In case of structure with vertical front wall $L \leq H_m$:

R_v, L – previously given designation,

M_b – resultant moment in the middle of the reinforced soil structure base, neglecting method factor γ_{F3}, [kNm/m].

3. Control of internal stability

The aim of this control is to determine whether tension stresses in the reinforcement are within permissible range and whether anchoring resistance of the bars is respectively greater than forces pulling the reinforcement from the soil. The formula adopted for control of internal stability is shown in Fig. 3. It was determined based on theoretical analyses, model research and tests of reinforced soil structures.

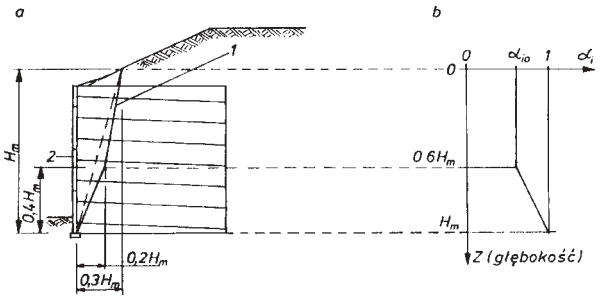

Fig. 3. Formula adopted for calculations of internal stability of the structure [1]: a – location of maximal stretching lines, b – change with depth of α_i factor, 1 – maximal stretching line, 2 – structure lining, z – depth

The line of maximal soil reinforcement stretching is determined first. Maximal stretching for 1 m. along the lining equals:

$$t_m = \sigma_h\, s_v \quad \text{[kN/m]} \qquad (4)$$

where: s_v – vertical spacing of reinforcement layers [m],

$\sigma_h = K\sigma_v + \sigma_{qh}$ – maximal horizontal stress in the analyzed reinforcement layer (along the maximal stress line) caused by the weight of its overlay , [kPa]

K factor depends on the depth (z) of reinforcement layer location in the soil mass:

– when $z \leq z_0$ *then* $K_z = K_a\, \Omega_1\, [1.6\,(1 - z/z_0) + z/z_0]$

– when $z \leq z_0$ *then* $K_{(z)} = K_a\, \Omega_1$

where:

$z_0 = 6$ m,

$K_a = tg^2\,(0.25\pi - 0.5\varphi_{1k})$ – active friction factor for the reinforced soil mass,

Ω_1 – form factor, assumed:

$\Omega_1 = 1.0$ in case of soil reinforcement with bands (flat bars),
$\Omega_1 = 1.5$ in case of soil reinforcement with shells (e.g. geogrids).

Vertical stress σ_v *at* (z) *level* is determined similarly as in case external stability control, which means calculating the resultant loads (above the analyzed layer) and distributing them according to Meyerhoff principle for width $(L_{(z)} - 2\,ex)$. In case of vertical lining the following relationship is binding:

$$\sigma_v(z) = R_v(z) / [L(z) - 2\,ex] + \sigma_{vq} \qquad (5)$$

in which:
$R_v(z)$ – resultant horizontal load (z) [kN/m],
$L(z)$ – horizontal length of reinforcement element (z) [m],
$ex = M(z) / R_v(z)$
$M(z)$ – horizontal overturning moment (z) in the middle of reinforcement layer; it is a resultant of all moments caused by loads applied above the level (z), considering their distribution [kNm/m],
σ_{vq} – vertical stress caused by loading the surcharge of the reinforced soil structure, considering distribution of this load [kPa].

When the reinforced soil structure is loaded with horizontal forces transverse to the lining (e.g. as a result of hydrostatic pressure or braking at the pavement), then soil reinforcement stretching caused by these forces should be taken into account.

Stretching stress at the lining of the structure is calculated according to the following formula:

$$t_p = (K \Sigma\, \alpha_i\, \sigma_{vi} + \sigma_{hq})\, h_a \qquad (6)$$

where:
K, h_a – previously given,
α_i – factor depending on flexibility of the lining and location of maximal stretching lines; its value changes corresponding to depth and in case of vertical linings it is (Fig. 3 b):
$\alpha_{i0} = 0.75$ – for very deformable linings (of metal and of geogrids, $i_f = 2$),
$\alpha_{i0} = 0.85$ – for moderately deformable linings (of prefabricated concrete units, $i_f = 1$),
$\alpha_{i0} = 1.00$ – for rigid linings (of concrete slabs with length identical with structure height, $i_f = 0$),
i_f – lining rigidity factor,
σ_{vi} – vertical stress corresponding to function α_i; for retaining structures equals $\alpha_i = 1.0$; for abutments $\alpha_i = 2.0$ [kPa].

Characteristic value of friction mobilized in each reinforcement layer is calculated according to the following formula:

$$r_f = 2\,N\,b\,L_a\,\mu^*\sigma_v \qquad (7)$$

in which:
N – number of reinforcing elements for 1 m along the lining (in case of shell lining $N = 1$); number 2 results from friction at the bottom and upper surface of the reinforcement $(2\,b\,L_a)$ [m^2],
b – width of reinforcement element (in case of shell lining $b = 1$) [m],
μ^* – real friction factor in the analyzed layer,
L_a – length of reinforcing element in the analyzed layer [m],
σ_v – mean vertical stress exerted on the analyzed reinforcement layer [kPa],
$\sigma_v = (1/L_a)\,(\sigma_v(x)\,dx$
$\sigma_v(x)$ – vertical stress at the (x) distance from lining in the analyzed reinforcement layer.

The most common load combinations which are taken into account while controlling internal stability of reinforced soil structure as well as partial safety factors (γ_m) are presented in the tables of NF P 94-200 [1, 3] standard.

Real friction factor μ^* is a relationship of cutting down stress to the mean vertical stress, which means that it depends on the depth of reinforcement location in the soil mass.

Safety control of each reinforcement layer with regard to break consists in determination whether two inequalities are fulfilled (considering the method factor as well as the partial safety factor with regard to reinforcement layer break):
- maximal stretching forces in the reinforcement layer are smaller than characteristic resistance of the reinforcement layer,
- maximal stretching stress at the structure lining is smaller than characteristic resistance of the reinforcement layer combined with the lining.

The partial safety factor with regard to the reinforcement layer break appears here and is assumed as 1.50 for standard structures and as 1.65 – for special ones (that means such, whose repairs will cause financial losses not acceptable for the user).

In each reinforcement layer and, when it is necessary also in the maximal stretching line, the stretching stress should be less than the value of characteristic friction mobilized in each reinforcement layer, while applying factor of method and partial safety factor for anchoring of reinforcement, assumed as 1.20 in case of standard structures and as 1.30 – for special structures.

It should also be controlled whether characteristic resistance of the lining is higher than maximal stretching stress at the lining (using the method factor and partial safety factor, assumed as 1.65 in case of concrete linings and as 1.50 – for metal linings).

4. Control of general stability

All potential soil destruction surfaces are taken into account as well as prevention of slides due to their cutting down resistance along these surfaces and increase of soil stability with the reinforcement layers cut by destruction surfaces. In case of uniform soil a potential destruction surface is usually cylindrical in form (Fig. 4).

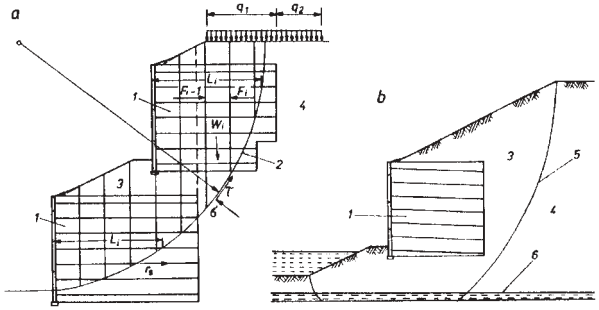

Fig. 4. Schemes of general stability control [1]: a – destruction along cylindrical surface, b – special case of destruction; 1 – reinforced soil mass, 2 – circular line of soil destruction, 3 – destruction zone, 4 – zone outside the destruction area, 5 – non-circular line of soil destruction, 6 – weak base layer

When a heavy structure is supported by reinforced soil mass, one of possible destruction forms is a wedge-shaped fragment including also this structure.

The maximal stretching value mobilized inside the reinforcement at the section with destruction surface is limited by:
- soil-reinforcement friction, which might be mobilized outside this surface,
- stretching resistance of the reinforcement bars,
- lining resistance at its joints with reinforcement, increased by friction value along the reinforcing elements, mobilized between the joints with the lining and the analyzed destruction surface.

Participation of soil reinforcement in the maintenance of general stability of the structure is expressed by F_R forces present in each reinforcement layer cut by destruction surface.

The designed soil resistance to cutting down τ_d along the destruction surface, at its each point, is calculated according to the following formula:

$$\tau_d = c_d + \sigma_n \, tg\varphi_d \quad \text{[kPa]} \tag{8}$$

in which:

c_d, φ_d – computational values of cutting down resistance parameters: cohesion, internal friction angle [kPa, degrees],

σ_n – normal stress in the soil in relation to destruction surface [kPa].

A number of destruction surfaces should be analyzed, usually with Bishop's method. In case of each method a general balance should be controlled using equations and moments and vertical forces. While applying the band method without analysis of balance of horizontal forces then reciprocal influence forces of bands in horizontal direction shall be adopted.

The stresses σ_n calculated according to the above formula have values different from the ones obtained in case of lack of reinforcement. This is caused by the influence of reinforcement bars anchored at both sides of destruction surface.

A general stability analysis should consider all potential load combinations: standard and random.

The binding partial safety parameters for control of general stability and load combinations are given in the standard tables [3].

5. Stability control with regard to subsoil load capacity

This control is realized basing on the evaluation of deformations' values, which will appear after the building of a structure of reinforced soil. Generally, such structures are characterized by increased flexibility, however, when great deformations are present they may negatively influence structures supported on the reinforced mass or located in its close proximity. Deformation causes might be of internal or external character (subsoil settlement or consolidation). Reinforcement bars are practically inextensible, and that is why designs take into account only external causes. Determination of settlements has a purpose of proving that deformations caused by them will fit the permissible range for buildings supported on the reinforced soil structures and remaining within the reach of subsoil deformation influence. Only combinations of constant and almost constant loads are considered in calculations. The values of partial safety factors (m used in these calculations are stated in the standard tables [3].

6. Conclusion

The principles of designing retaining structures of the reinforced soil with limit conditions method, elaborated in the French standard NF P 94-200 were discussed. The computation scheme of the structure was given in which the standard assumes a broken line of maximal stretching in the reinforcement as well as distribution of stretching forces' values according to the principles of the reinforced soil classics (H. Vidal, F. Schlosser [2, 5, 6]. A special emphasize should be put on the load combinations proposed for consideration by the standard [3] (deadweight, moving load, soil backfill pressure) as well as partial safety factors of the external, internal and general stability and: method factors, partial factors of settlement safety and values of soil medium-reinforcement friction for some cases of reinforcement bars. It seems worthwhile to confront resolutions of the French standard with Polish standard [4] with regard to its possible modification.

References

[1] JAROMINIAK, A.: *Light retaining structures (Lekkie konstrukcje oporowe)*, WkiŁ, Warsaw 1999.
[2] LONG, N.T., SCHLOSSER, F.: *Dimensioning of reinforced soil walls (Wymiarowanie murów z gruntów zbrojonych)*, Selected Problems of Geotechnics (Wybrane Zagadnienia Geotechniki), PAN-IBW, Wrocław, Ossolineum, 1978, s. 211-237.

[3] NFP 94-200: *Reinforcement des sols par inclusions.* Ouvrages en sols rapportes renforces par armatures ou nappes peu extensibles et souples. Dimensionnement.
[4] PN 83/B-03010: *Retaining walls (Ściany oporowe).* Static calculations and design (Obliczenia statyczne i projektowanie), PN 83/B-03010, 1983.
[5] SCHLOSSER, F.: *La terre armee', historique development, actuel et futur.* Proc. Symp. Soil Reinforcing and Stabilising Techq., NSWIT/NSW Univ., 1978, s. 5-28.
[6] SCHLOSSER, F.: *Reinforced Soil in Civil Engineering* (in Polish). Archiv. Hydrotechn., Vol. XXI, No. 2, pp. 299-336, 1974.

COMMUNICATIONS – Scientific Letters of the University of Žilina
Writer's Guidelines

1. Submissions for publication must be unpublished and not be a multiple submission.
2. Manuscripts written **in English language** must include abstract also written in English. The submission should not exceed 7 pages (format A4, Times Roman size 12). The **abstract** should not exceed 10 lines.
3. Submissions should be sent: **by e-mail** (as attachment in system Microsoft WORD) to one of the following addresses: *holesa@nic.utc.sk* or *vrablova@nic.utc.sk* or *polednak@fsi.utc.sk* **with a hard copy** (to be assessed by the editorial board) **or on a 3.5″ diskette** with a hard copy to the following address: Zilinska univerzita, OVaV, Moyzesova 20, SK-10 26 Zilina, Slovakia.
4. Abbreviations, which are not common, must be used in full when mentioned for the first time.
5. Figures, graphs and diagrams, if not processed by Microsoft WORD, must be sent in electronic form (as GIF, JPG, TIFF, BMP files) or drawn in contrast on white paper, one copy enclosed. Photographs for publication must be either contrastive or on a slide.
6. References are to be marked either in the text or as footnotes numbered respectively. Numbers must be in square brackets. The list of references should follow the paper (according to **ISO 690**).
7. The author's exact **mailing address of the organisation where the author works, full names, e-mail address or fax event. telephone number,** must be enclosed.
8. The editorial board will assess the submission in its following session. In the case that the article is accepted for future volumes, the board submits the manuscript to the editors for review and language correction. After reviewing and incorporating the editor's remarks, the final draft (before printing) will be sent to authors for final review and adjustment.
9. The deadlines for submissions are as follows: September 30, December 31, March 31 and Juny 30.

POKYNY PRE AUTOROV PRÍSPEVKOV DO ČASOPISU
KOMUNIKÁCIE – vedecké listy Žilinskej univerzity

1. Redakcia prijíma iba príspevky doteraz nepublikované alebo inde nezaslané na uverejnenie.
2. Rukopis musí byť **v jazyku anglickom**. Príspevok by nemal prekročiť 7 strán (formát A4, písmo Times Roman 12 bodové). K článku dodá autor **resumé** v rozsahu maximálne 10 riadkov (v anglickom jazyku).
3. Príspevok prosíme poslať: **e-mailom**, ako prílohu spracovanú v aplikácii Microsoft WORD, na adresu: *holesa@nic.utc.sk* alebo *polednak@fsi.utc.sk* príp. *vrablova@nic.utc.sk* (alebo doručiť na diskete 3,5″) **a jeden výtlačok** článku na adresu Žilinská univerzita, OVaV, Moyzesova 20, 010 26 Žilina.
4. Skratky, ktoré nie sú bežné, je nutné pri ich prvom použití rozpísať v plnom znení.
5. Obrázky, grafy a schémy, pokiaľ nie sú spracované v Microsoft WORD, je potrebné doručiť buď v digitálnej forme (ako GIF, JPG, TIFF, BMP súbory), prípadne nakresliť kontrastne na bielom papieri a predložiť v jednom exemplári. Pri požiadavke na uverejnenie fotografie priložiť ako podklad kontrastnú fotografiu alebo diapozitív.
6. Odvolania na literatúru sa označujú v texte alebo v poznámkach pod čiarou príslušným poradovým číslom v hranatej zátvorke. **Zoznam použitej literatúry** je uvedený za príspevkom. Citovanie literatúry musí byť **podľa STN 01 0197 (ISO 690)** „Bibliografické odkazy".
7. K rukopisu treba pripojiť **plné meno a priezvisko autora a adresu inštitúcie v ktorej pracuje, e-mail adresu** alebo číslo telefónu event. faxu.
8. Príspevok posúdi redakčná rada na svojom najbližšom zasadnutí a v prípade jeho zaradenia do niektorého z budúcich čísiel podrobí rukopis recenziám a jazykovej korektúre. Pred tlačou bude poslaný autorovi na definitívnu kontrolu.
9. Termíny na dodanie príspevkov do čísiel v roku sú: 30. september, 31. december, 31. marec a 30. jún.

kamUNikácie
COMMUNICATIONS

VEDECKÉ LISTY ŽILINSKEJ UNIVERZITY
SCIENTIFIC LETTERS OF THE UNIVERSITY OF ŽILINA
5. ROČNÍK – VOLUME 5

Adresa redakcie:
Address of the editorial office:
Žilinská univerzita
Oddelenie pre vedu a výskum
Office for Science and Research
Moyzesova 20, Slovakia
SK 010 26 Žilina
Tel.: +421/41/5620 392
Fax: +421/41/7247 702
E-mail: polednak@fsi.utc.sk, holesa@nic.utc.sk

Každý článok bol oponovaný dvoma oponentmi.
Each paper was reviewed by two reviewers.

Časopis je excerpovaný v Compendexe
Journal is excerpted in Compendex

Vydáva Žilinská univerzita
v EDIS – vydavateľstve ŽU
J. M. Hurbana 15, 010 26 Žilina
pod registračným číslom 1989/98
ISSN 1335-4205

It is published by the University of Žilina in
EDIS - Publishing Institution of Žilina University
Registered No: 1989/98
ISSN 1335-4205

Objednávky na predplatné prijíma redakcia
Vychádza štvrťročne
Ročné predplatné na rok 2004 je 500,– Sk

Order forms should be returned to the editorial office
Published quarterly
The subscription rate for year 2004 is 500 SKK

Jednotlivé čísla časopisu sú uverejnené tiež na:
http://www.utc.sk/komunikacie
Single issues of the journal can be found on:
http://www.utc.sk/komunikacie